# Numerical Simulations of High Speed Turbulent Jets in Crossflow

A DISSERTATION
SUBMITTED TO THE FACULTY OF THE GRADUATE SCHOOL
OF THE UNIVERSITY OF MINNESOTA
BY

**Xiaochuan Chai**

IN PARTIAL FULFILLMENT OF THE REQUIREMENTS
FOR THE DEGREE OF
Doctor of Philosophy

**Krishnan Mahesh, Advisor**

**August, 2012**

# Acknowledgements

First and foremost, I would like to thank my adviser Professor Krishnan Mahesh, for his constant advice, encouragement and support. His experience, intelligence, and patience were instrumental. He has provided not only great guidance to my PhD study but also a lot of help and suggestions to my life and future career, for which that I am very grateful.

I would also like to thank my colleagues: Dr. Suman Muppidi, Dr. Noma Park, Dr. Shankar Ghosh, Mr. Aman Verma and Mr. Prahladh Iyer for their great help and usefully discussions on this project. During the starting stage of my research, Dr. Yucheng Hou and Dr. Jeff Doom helped me a lot to quickly get familiar with the group. Great thanks to Mr. Michael Moselle and Mrs. Tessa Wagnild for their help on my English shortly after I started my study in the States. Special thanks to Dr. Rajes Sau and Dr. Hyunchul Jang. We have been working in the same office since always, and I have gained a lot from them on every aspect of PhD study and life abroad.

I am mostly indebted to my wife, Jing, for her unconditional support, which has allowed me to devote myself to my PhD work. Her understanding, encouragements and advises are essential to my current and future success. I would also thank my parents whose endless love is always with me wherever I am.

This work is supported by the National Science Foundation under grants CTS–0828162 and CTS–0933377. Computer time for the simulations was provided by Minnesota Supercomputing Institute (MSI), National Institute for Computational Sciences (NICS) and Texas Advanced Computing Center (TACC).

# Dedication

To my wife and my parents

# Abstract

This dissertation studies high speed jets in crossflow using numerical simulations. The complexity of this flow makes detailed measurements difficult, and only limited information is provided by past experimental studies. Traditional engineering simulation tools also have difficulties in simulating such flows. Therefore, the current study: 1) develops Large-Eddy Simulation (LES) capability and novel subgrid-scale (SGS) models for high speed flows in complex geometries; 2) realizes multiple methods to generate realistic turbulent boundary layer inflow condition for unstructured compressible flow solver; 3) explores the detailed physics of high speed jets in crossflow; 4) investigates the jet trajectory, entrainment and coherent vortical motions.

Large-eddy simulation capability is developed for the base numerical scheme developed by Park & Mahesh [1] for solving the compressible Navier-Stokes equations on unstructured grids. Large-eddy simulations are performed to study an under-expanded sonic jet injected into a supersonic crossflow and an over-expanded supersonic jet injected into a subsonic crossflow, where the flow conditions are based on Santiago *et al.*'s [2] and Beresh *et al.*'s [3] experiments, respectively. The simulations successfully reproduce experimentally observed shock systems and vortical structures. The time averaged flow fields are compared to the experimental results, and reasonable agreement is observed. The behavior of the flow is discussed, and the similarities and differences between the two regimes are studied. The trajectory and entrainment of the transverse jet is investigated. A modification to Schetz & Billig's theory [4] theory is proposed, which yields good prediction of the jet trajectories in the current simulations in the near field. Along the jet center streamline, the jet entrainment grow faster compared to turbulent free jets. In the very far field, the growth rates of jet entrainment decrease to values that are close to those for turbulent free jets. The Strouhal numbers of relevant flow structures are computed from power spectral densities. Many flow motions are observed to be correlated in sonic jet in supersonic crossflow. The frequencies in supersonic injection are observed to be higher than those in sonic injection.

A novel eddy-viscosity model, "dynamic $k$-equation model", is proposed for the LES of compressible flows with complex flow geometries, where the transport equation for sub-grid scale (SGS) kinetic energy is introduced to predict SGS kinetic energy, instead of using Yoshizawa's model as in standard Dynamic Smagorinsky Model (DSM). The exact SGS kinetic energy transport equation for compressible flows is derived formally. Each of the unclosed terms in the SGS kinetic energy equation is modeled separately and dynamically closed, instead of being grouped into production and dissipation terms, as in the Reynolds Averaged Navier- Stokes (RANS) equations. *A priori* test using Direct Numerical Simulation (DNS) of decaying isotropic turbulence shows that for Smagorinsky type eddy viscosity model, the correlation between SGS stress and the model is comparable to that from the original model. Also, the suggested model for pressure dilatation term in the SGS kinetic energy equation is found to have high correlation with its actual value. In *a posteriori* tests, the proposed dynamic $k$-equation model is applied to decaying isotropic turbulence and normal shock/isotropic turbulence interaction, and yields good agreement with available experimental and DNS data. Compared with the results of Dynamic Smagorinsky Model (DSM), the $k$-equation model predicts better energy spectra at high wave numbers, similar kinetic energy decay and fluctuations of thermodynamic quantities for decaying isotropic turbulence. For shock/turbulent interaction, $k$-equation model and DSM predict similar evolution of turbulent intensities across shocks, due to the dominant effect of linear interaction. The proposed $k$-equation model is more robust in that local averaging over neighboring control volumes (CV) is sufficient to regularize the dynamic procedure. The behavior of pressure dilation and dilatational dissipation is discussed through the budgets of SGS kinetic energy equation, and the importance of dilatational dissipation term is addressed.

The proposed dynamic $k$-equation model is then applied to Mach 2.9 supersonic turbulent boundary layer, where a recycling-rescaling method for turbulent boundary layer generation on fully unstructured meshes is developed and applied. Good agreement is observed between the LES results and available DNS and experimental results.

# Contents

# List of Tables

# List of Figures

# Chapter 1

# Introduction

## 1.1 Motivation and background

The term, jet in cross-flow (JIC), refers to a jet of fluid that exits an orifice to interact with the surrounding fluid that is flowing across the orifice (figure 1.1 *a*). High speed jets in crossflow implies that either the jet or the crossflow is supersonic. High speed jets in crossflow are central to a variety of applications. For example, in scramjet engine combustors (figure 1.1 *c*), sonic jets of fuel are injected into a supersonic crossflow of air. Due to their high speeds, the fuel and the air will reside in the combustor only for milliseconds. Successful operation of the combustor requires the fuel and the air to efficiently mix and burn thoroughly before they exit the combustor. Accurate estimation and detailed physical understanding of the turbulent mixing mechanisms are therefore essential to the design of scramjet combustors. Another important application of the high speed jets in crossflows is the steering of atmospheric flight vehicles, which includes thrust vector and attitude/roll control. The thrust vectoring technique utilizes the forces developed on the wall of the divergent portion of the flight exhaust nozzle by injecting lateral jet into the supersonic propellent gases. In addition to the usual jet reaction, it is observed that the transverse jets can cause significantly change in wall pressure distribution due to the induced shock waves from jet/crossflow interaction. Under certain conditions, the resulting transverse force could be as large as the primary thrust. Therefore, better interpretation of the relation between the resultant side forces and jet/crossflow conditions is crucial to the success of thrust vector control.

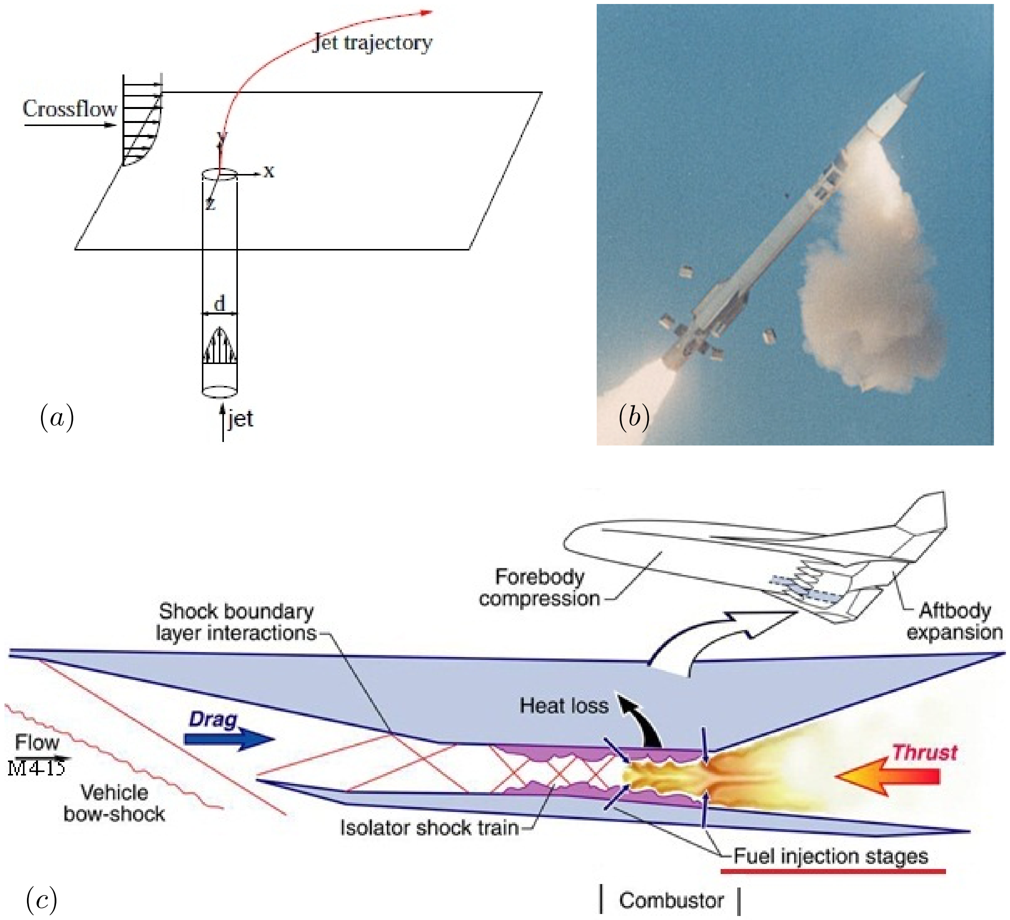

Figure 1.1: (*a*) Schematic of jet into crossflow; (*b*) Attitude control using supersonic jets (http://bemil.chosun.com/nbrd/files/BEMIL085/upload/2006/10/%20Patriot%20Advanced%20Capability%20(PAC-3)_01.jpg); (*c*) Schematic of scramjet engine (http://en.wikipedia.org/wiki/File:ScramjetEngine.jpg).

In attitude/roll control (figure 1.1 *b*), supersonic jet plumes exit the nozzle, reorient upon encountering the crossflowing freestream and travel downstream; where the jet and the induced flows can interact with aerodynamic control surfaces. In this case, understanding the turbulent characteristics in the far field of the jet is important.

High speed jets in crossflow are very complex flows. The complexity of this flow makes detailed measurements difficult, and only limited information is provided by past experimental studies. Traditional engineering simulation tools also have difficulties in simulating such flows. Thus, basic understanding of high speed jets in crossflow is still lacking, and several important questions are still unanswered. Large-eddy simulation is currently the most feasible way to simulate such flows. It resolves the large scale fluid motions and models the small scale (subgrid scale, SGS) motions. Therefore, accurate SGS models are important to the accuracy of LES. However, most of the existing SGS models are either developed for incompressible flows or flows with simple geometries. The compressible version of Dynamic Smagorinsky Model (DSM) is still the most popular model over 20 years, in spite of some know issues in accuracy and regularization.

In the light of the practical relevance of high speed jets in crossflow, the primary objectives of the current study are to:

1. develop the LES capability and novel SGS models for complex high speed flows;
2. provide a high-fidelity simulation database for high speed jets in crossflow;
3. explore the detailed physics of high speed jets in crossflow;
4. answer specific questions concerning the jet trajectory, entrainment, wall pressure distribution and dynamics of coherent vortical structures.

## 1.2 Past works on high speed jets in crossflow

Past work on high speed jets in crossflow are well summarized in the review paper by Mahesh [5]. Several early studies of thrust vector control using high speed transverse jets have been performed, where the induced pressure fields on the surfaces were measured to determine the change in the total thrust (e.g. [6], [7], [8], [9], [10]). Most recent studies are motivated by the application of high speed jets in crossflow to supersonic combustion (e.g. [11], [2], [12], [13], [14]). A variety of methods have been used to study high speed jets in crossflow, such as Schlieren photography (e.g. [6], [2]), planar Mie-scattering (e.g. [15], [11]), laser Doppler velocimetry (e.g. [2]), laser-induced fluorescence (e.g. [16], [17], [13]) and particle image velocimetry (PIV) (e.g. [18], [3], [19], [20]). Because of the complexity of this type of flows, detailed flow measurements are very difficult. Flow visualization has therefore been used to study the jet penetration, mixing and overall flow structure in high speed jets in crossflow, and some shock and vortical structures have been identified. A three-dimensional bow shock and a separation region form in front of the jet due to the blockage to the supersonic crossflow by the transverse jet. The separation region lifts the crossflow boundary layer and creates a "ramp", which further induces a separation shock (e.g. [15], [2]) ahead of the bow shock. An inclined barrel shock and Mach disk form at the periphery of the high speed jet plume as the jet exits the nozzle, expands and interacts with the crossflow. The typical vortical structures in high speed jets in crossflow are identified similarly to low speed jets in crossflow, which include: the near-field jet shear layer vortices, the downstream wake vortices, the horseshoe vortices wrapping around the jet column and the counter-rotating vortex pair (CVP) in the far field. As noted by Fric & Roshko [21] for low speed transverse jets, the former two types of vortices are unsteady and can be observed from the instantaneous flow field; while the latter two are usually observed and defined in the mean, though they also have unsteady components.

Jet penetration in high speed crossflow has been studied by numerous researchers [4, 16, 22, 23, 11, 13]. The jet-to-crossflow momentum ratio,

$$J = \frac{\rho_j V_j^2}{\rho_\infty U_\infty} = \frac{\gamma_j P_j M_j^2}{\gamma_\infty P_\infty M_\infty^2} \tag{1.1}$$

is recognized as the parameter that has the dominant effect on the jet penetration. Here, the subscript $j$ denotes the jet exit condition, while the subscript $\infty$ denotes the quantities of the crossflow. Compared to the widely used $rD$ scaling in incompressible jets in crossflow, $JD$ scaling appears to scale high speed jet trajectories best (e.g. [3]). Here $r$ is the jet-to-crossflow velocity ratio. In most of the experimental studies, power or logarithm functions with adjustable coefficients are used to fit the experimental data. However, it is shown (section 3.6) that these coefficients differ a lot between different studies, and the trajectory data from different studies show a large level of scatter even with $JD$ scaling. Papamoschou & Hubbard [23] studied the effect of crossflow Mach number and jet exit Mach number on the jet penetration. They pointed out that due to equation (1.1), the effect of Mach number cannot be evaluated unambiguously while keeping other quantities such as jet-to-crossflow momentum ratio and pressure ratio constant. Their study showed that the jet penetration increases slightly with the crossflow Mach number while keeping $J$ constant. Also Ben-Yakar *et al.* [13] found in their experiments that molecular weight also play a role in the jet penetration. Obviously, there are factors other than $J$ that affect the jet penetration, which must be considered to yield better scaling laws for the jet trajectories.

Among the previous experimental studies, the works of Santiago & Dutton [2] and Beresh *et al.* [3, 19, 20] provide relatively more quantitative data. Santiago & Dutton [2] measured the detailed velocity field induced by a sonic jet injected into a Mach 1.6 supersonic crossflow on the symmetric plane and crossplanes. Beresh *et al.* carried out a series of experiments [3, 19, 20] on over-expanded supersonic jets injected into subsonic crossflow. Based on 7 different flow configurations, Beresh *et al.* studied the influence of free stream Mach number and that of jet-to-crossflow momentum ratio on the penetration of the jet, the turbulent characteristics in the far field downstream of the jet and the scaling of counter-rotating vortex pairs (CVP) at cross planes. A number of numerical simulations were performed to compare to Santiago & Dutton's work [2] (e.g. [24], [25], [26] and [27]). These numerical studies discussed the presence of large-scale stuctures, the influence of crossflow boundary layer type and crossflow Mach number, the dynamics of barrel shock and jet shear layer vorticies, and mixing properties. These studies are mostly qualitative and emphasize the evaluation of specific algorithm or subgrid-scale models. In contrast, few numerical studies of supersonic jets injected into a subsonic crossflow have been reported in literature. Therefore, the quantitative and detailed study of high speed jet in crossflow is still lacking.

## 1.3 Past works on large-eddy simulations

Large-eddy simulations (LES) have gained great success in simulating practical flows where the Reynolds numbers are usually very high. By calculating the large-scale fluid motions directly from the filtered Navier-Stokes equations while modeling the unresolved motions, large-eddy simulations alleviate the Reynolds number restrictions in DNS, but preserve the ability to present the instantaneous flow characteristics and turbulent flow structures. Numerous modeling works have been performed on LES. However, Most of these models are either developed for incompressible flows or restricted to flows with simple geometries. Relatively fewer models have been developed for compressible flows. The compressible DSM model developed by Moin *et al.* [28] is still the most popular model used in simulations of compressible flows. As opposed to incompressible flows, the SGS kinetic energy has to be modeled explicitly in compressible LES. The most commonly used model for SGS kinetic energy is Yoshizawa's model [29] which is derived from the multiscale direct interaction approximation [30]. Speziale *et al.* [31] showed that Yoshizawa's model is only applicable to compressible flows with small density fluctuations, and correlates poorly with the DNS results of isotropic turbulence at low Mach numbers. They suggested that these limitations could be reduced based on Favre-filtered fields. In compressible DSM, Favre-filtering is applied, and Yoshizawa's model is naturally generalized for SGS kinetic energy. Furthermore, Yoshizawa's model is based on the assumption of local equilibrium, i.e. the production of turbulent energy equals its dissipation, which is not the case most of the time. It has been shown that Yoshizawa's model tends to under-predict the magnitude of SGS kinetic energy [1].

An alternative and original approach to derive SGS kinetic energy is by solving its transport equation. One equation SGS models have been extensively used in incompressible LES [32, 33, 34, 35, 36, 37, 38, 39, 40], and have shown success especially in the prediction of inhomogeneous turbulent flows. For example, Horiuti [41] showed that the SGS kinetic energy equation model yielded improved performance than Smagorinsky model in the simulation of rectangular channel flow. For compressible LES, works on one equation SGS models are lacking. Therefore, we develop a compressible version of the dynamic Smagorinsky model with SGS kinetic energy equation which is termed "dynamic k-equation model" in the rest of this dissertation.

The localized dynamic k-equation model (LDKM), developed by Menon & kim [40], is an eddy viscosity model based on the SGS kinetic energy equation for incompressible flows. Recently, LDKM has been extended for compressible flows and applied to the LES of a sonic jet injected into a supersonic crossflow [26]. Extra terms were added to the SGS kinetic energy equation to account for compressibility effects. Both the incompressible and compressible SGS kinetic energy equations used in LDKM are simplified/modeled equations which appear to be adapted from the transport equations for turbulent kinetic energy [42]. A different methodology is used for the dynamic procedure as well. In the current study, the exact compressible SGS kinetic energy equation is derived formally. Each of the unclosed terms are modeled separately instead of being grouped into production, dissipation, etc., so that the contribution of each term can be evaluated individually. For example, dilatational dissipation and solenoidal dissipation are modeled separately unlike Gènin & Menon [26] who note that modeling them together is subject to the assumption of low Mach number. Furthermore, all of the extra SGS terms (besides SGS stress and SGS heat flux) in the filtered total energy equation [43, 44] are found to reappear in the SGS kinetic energy equation, which allows us to take them into account without adding extra computational cost. The traditional Germano identity is applied to the dynamic closure for most SGS terms.

## 1.4 Overview

In the current study, a novel one-equation eddy viscosity model is developed for the LES of compressible flows with complex geometry. The proposed model is applied to the simulations of a variety of flow field, such as quasi-incompressible turbulence, turbulence with locally high compression regions, turbulence with shock in the mean and supersonic turbulent boundary layer for validation. Large-eddy simulations are performed to study the detailed flow physics of the high speed jets in crossflow, where both a sonic jet injected into a supersonic crossflow and a supersonic jet injected into a subsonic crossflow are considered. The primary contributions of the current work are: i) develop LES capability and novel SGS models for high speed flows with complex geometries; ii) provide a high-fidelity simulation database for high speed transverse jets in crossflow; iii) explore the detailed physics of high speed jets in crossflow; iv) answer specific questions concerning the jet trajectory, entrainment, wall pressure distribution and dynamics of coherent vortical structures.

The dissertation is organized as follows. Chapter 2 introduces the algorithm and the background of large-eddy simulations. Chapter 3 presents the simulation results of high speed jet in crossflow, explores the detailed flow physics, and discusses specific topics such as wall pressure distribution, jet trajectory, entrainment and the dynamics of coherent vortical structures. Chapter 4 shows the development and validation of dynamic $k$-equation model for the LES of compressible flows. In Chapter 5, the performance of the proposed dynamic $k$-equation model is further evaluated by supersonic turbulent boundary layer, where the recycling-rescaling turbulent boundary layer generator is realized for fully unstructured compressible flow solver.

# Chapter 2

# Algorithm

## 2.1 Governing equations

The Navier–Stokes equations for compressible flows are

$$\begin{aligned}
\frac{\partial \rho}{\partial t} &= -\frac{\partial}{\partial x_j}\left(\rho u_j\right), \\
\frac{\partial \rho u_i}{\partial t} &= -\frac{\partial}{\partial x_j}\left(\rho u_i u_j + p\delta_{ij} - \sigma_{ij}\right), \\
\frac{\partial E_T}{\partial t} &= -\frac{\partial}{\partial x_j}\left\{\left(E_T + p\right) u_j - \sigma_{ij} u_i - Q_j\right\}, \\
p &= \rho R T
\end{aligned} \tag{2.1}$$

Here, $\rho$, $u_i$, $p$ and $E_T$ are the density, velocity, pressure and total energy, respectively. R is the specific gas constant. The viscous stress $\sigma_{ij}$ and heat flux $Q_j$ are given by

$$\sigma_{ij} = \frac{\mu}{Re}\left(\frac{\partial u_i}{\partial x_j} + \frac{\partial u_j}{\partial x_i} - \frac{2}{3}\frac{\partial u_k}{\partial x_k}\delta_{ij}\right), \tag{2.2}$$

$$Q_j = \frac{\mu}{\left(\gamma - 1\right) M_\infty^2 Re Pr}\frac{\partial T}{\partial x_j} \tag{2.3}$$

after standard non-dimensionalization, where $Re$, $M_\infty$ and $Pr$ denote the Reynolds number, Mach number and Prandtl number. $T$ is the temperature. And $\mu$ is the non-dimensionalized molecular viscosity which obeys Sutherland's viscosity law [45].

## 2.2 Numerical Scheme

The numerical scheme is that developed by Park & Mahesh [1] for solving the compressible Navier–Stokes equations (Eq. 2.1) on unstructured grids. The governing equations are discretized using a cell–centered finite volume scheme. Upon integration over the control volume (CV), application of the Gauss theorem, and some rearrangement, the governing equations may be written as

$$\begin{aligned}
\frac{\partial \rho_{\mathrm{cv}}}{\partial t} &= -\frac{1}{V_{\mathrm{cv}}} \sum_{\text{faces}} \rho_f v_N A_f, \\
\frac{\partial \left(\rho u_i\right)_{\mathrm{cv}}}{\partial t} &= -\frac{1}{V_{\mathrm{cv}}} \sum_{\text{faces}} \left[ \left(\rho u_i\right)_f v_N + p_f n_i - \sigma_{ik,f} n_k \right] A_f, \\
\frac{\partial \left(E_T\right)_{\mathrm{cv}}}{\partial t} &= -\frac{1}{V_{\mathrm{cv}}} \sum_{\text{faces}} \left[ \left(E_T + p\right)_f v_N - \sigma_{ik,f} u_{i,f} n_k - Q_{k,f} n_k \right] A_f,
\end{aligned} \tag{2.4}$$

where $V_{\mathrm{cv}}$ is the volume of CV, $A_f$ is the area of face, $n_i$ is the outward normal vector at surface, and $v_N$ is the face-normal velocity. The solution is advanced in time using a second–order explicit Adams–Bashforth scheme.

Discretization of the governing equations involves reconstruction of the variables at the faces from the CV center values. Also, the spatial accuracy of the algorithm is sensitive to this flux reconstruction. The simulations employ a Modified least–square method (MLSQ) [1] for this reconstruction, the modified wavenumber of which shows better spectral resolution than the $4^{th}$ order central difference scheme, at high wavenumbers. When tested on vortex convection, Taylor–Green problem, decaying isotropic turbulence and scalar convection, the MLSQ method is found to be more accurate than a simple symmetric reconstruction, and more stable than a least–square reconstruction. The viscous stress term is split into two parts, i.e. $\sigma_{ij} = \sigma_{ij}^s + \sigma_{ij}^c$, where $\sigma_{ij}^s = (\mu/Re)(\partial u_i/\partial x_j)$ is the incompressible part, and $\sigma_{ij}^c = (\mu/Re)[(\partial u_j/\partial x_i) - \frac{2}{3}(\partial u_k/\partial x_k)\delta_{ij}]$ is the compressible part. Such splitting ensures that the dominant incompressible component only depends on the nearest neighbors and is therefore more accurate at high wavenumbers, and devoid of odd-even decoupling.

The algorithm uses a shock–capturing scheme that was originally proposed by Yee, Sandham & Djomehri [46] for structured meshes and was extended by Park & Mahesh [1] to unstructured meshes, and further localized to reduce unnecessary numerical dissipation. The shock–capturing is implemented in predictor-corrector form. Once the predicted solution $\hat{\mathbf{q}}^{n+1}$ is obtained from $\mathbf{q}^n$, the final solution $\mathbf{q}^{n+1}$ at $t + \Delta t$ is determined from a corrector step:

$$\mathbf{q}_{\text{cv}}^{n+1} = \hat{\mathbf{q}}_{\text{cv}}^{n+1} - \frac{\Delta t}{V_{\text{cv}}} \sum_{\text{faces}} \left(\mathbf{F}_f^* \cdot \mathbf{n}_f\right) A_f, \tag{2.5}$$

where $\mathbf{F}_f^*$ is the filter numerical flux. Here, $\mathbf{q}^n$ and $\mathbf{q}^{n+1}$ are the conserved variable arrays at time step $n$ and $n+1$, and $\hat{\mathbf{q}}^{n+1}$ is the set of variables at time step $n+1$ but prior to the application of shock–capturing. The predictor step (base scheme) is symmetric and non-dissipative, and is designed to accurately represent broadband turbulence; while the corrector step is a characteristic-based filter that is active only in the vicinity of discontinuities. Therefore, the overall scheme avoids unnecessary numerical dissipation.

The algorithm was evaluated by Park & Mahesh [1] for shock/vortex interaction, shock tube problem, two-dimensional mixing layer and under-resolved turbulence. For shock/vortex interaction, the algorithm captures the deformation of vortex and shock wave accurately. In mixing layer problem, the formation of shocklets as well as the pairing and merging of vortex are well represented. Importantly, it is observed that any numerical dissipation is localized to the immediate vicinity of the discontinuity and the solution away from the shock sees zero numerical dissipation. When applied to an under-resolved turbulence problem, the algorithm shows minimal effects of numerical dissipation when the shock-capturing scheme is turned on and off. Moreover, the algorithm is found to work well even on tetrahedral meshes for all the test problems, and shocks are captured within two grid points in spite of coarse resolution. Further details about the algorithm are provided in the work of Park & Mahesh [1]. The algorithm has also been successfully applied to various flows with complex geometries such as roughness-induced transition in supersonic boundary layers [47] and simulations of high speed jets in crossflow [48].

## 2.3 Large-eddy simulation

Numerical simulations that solves the governing equations (2.1) are called Direct Numerical Simulation (DNS), because no flow modeling is involved. Therefore, DNS is believed to the most accurate and reliable simulation method. To represent all the details of a flow field, DNS requires the grid resolution to be high enough to resolve the smallest motions in the flow, which scale with the Kolmogorov length scale $\eta$ [49]. According to Kolmogorov's theory [49], the size of the smallest eddy decreases with increase of the Reynolds number, i.e. $\eta \sim Re^{-3/4}$. Therefore, the DNS of practical flows (usually have very high Reynolds numbers) are computationally expensive and sometimes impractical. Alternatively, one can perform the simulation on a relatively coarse mesh to revolve the large scale motions and model the small scale (subgrid-scale, SGS) ones to take into account their effects. Such simulations are called Large-eddy Simulation (LES).

LES decomposes flow variables into resolved (filtered) and SGS (residual) terms through filtering operation. For example, any flow variable can be decomposed as

$$\phi\left(x\right) = \bar{\phi}\left(x\right) + \phi'\left(x\right), \tag{2.6}$$

where

$$\bar{\phi}\left(x\right) = \int_{\Omega} G_{\Delta}\left(x, y\right) \phi\left(y\right) dy \tag{2.7}$$

denotes the spatial filtering of $\phi\left(x\right)$. $G_{\Delta}\left(x, y\right)$ is the kernel of the filter which satisfies the normalization condition

$$\int_{\Omega} G_{\Delta}\left(x, y\right) dy = 1. \tag{2.8}$$

In practice, especially for unstructured flow solvers, the filter is usually the grid filter with the filter width $\Delta$ being a measure of local grid size. The filtered quantities are solved numerically from the filtered governing equations, which provides an approximation to the large-scale motions in the flow fields. Within the filtered governing equations, there are SGS stress terms representing the influence of SGS motions on the resolved field. These SGS terms can not be calculated directly and therefore are modeled in terms of resolved quantities. Large-eddy simulations (LES) have gained great success in simulating practical flows where the Reynolds numbers are usually very high. By calculating the large-scale fluid motions directly from the filtered Navier-Stokes equations while modeling the unresolved motions, large-eddy simulations alleviate the Reynolds number restrictions in DNS, but preserve the ability to present the instantaneous flow characteristics and turbulent flow structures, as opposed to RANS (Reynolds Averaged Navier-Stokes) which only predicts the mean flow information.

### 2.3.1 The Filtered Navier-Stokes Equations

For compressible flow, the density weighted (Favre) filtering is applied, i.e.,

$$\tilde{\phi} = \frac{\overline{\rho\phi}}{\bar{\rho}}. \tag{2.9}$$

When Favre-filtered, the spatially filtered compressible Navier-Stokes equations take the form of

$$\begin{aligned}
\frac{\partial \bar{\rho}}{\partial t} &= -\frac{\partial \left(\bar{\rho}\widetilde{u_j}\right)}{\partial x_j}, \\
\frac{\partial \left(\bar{\rho}\widetilde{u_i}\right)}{\partial t} &= -\frac{\partial}{\partial x_j}\left(\bar{\rho}\widetilde{u_i}\widetilde{u_j} + \bar{p}\delta_{ij} - \widetilde{\sigma_{ij}} + \tau_{ij}\right), && (2.10) \\
\frac{\partial}{\partial t}\left(\bar{\rho}\widetilde{E}\right) &= -\frac{\partial}{\partial x_j}\left(\bar{\rho}\widetilde{E}\widetilde{u_j} + \bar{p}\widetilde{u_j} - \widetilde{\sigma_{ij}}\widetilde{u_i} - \overline{Q_j} + C_p q_j\right) + H, && (2.11) \\
\bar{p} &= \bar{\rho}R\widetilde{T},
\end{aligned}$$

where $\rho$, $u_i$, $p$, $E$ are density, velocity, pressure and specific total energy, respectively. The viscous stress $\widetilde{\sigma_{ij}}$ and heat flux $\overline{Q_j}$ are given by

$$\begin{aligned}
\widetilde{\sigma_{ij}} &= 2\bar{\mu}\widetilde{S_{ij}^{*}}, && (2.12) \\
\overline{Q_j} &= \bar{\kappa}\frac{\partial \widetilde{T}}{\partial x_j}, && (2.13)
\end{aligned}$$

where $\mu$ is the molecular viscosity, $\kappa$ is the thermal conductivity, $S_{ij}^{*}$ is the traceless strain rate tensor, i.e.

$$\begin{aligned}
\widetilde{S_{ij}^{*}} &= \widetilde{S_{ij}} - \frac{1}{3}\delta_{ij}\widetilde{S_{kk}} && (2.14) \\
&= \frac{1}{2}\left(\frac{\partial \widetilde{u_i}}{\partial x_j} + \frac{\partial \widetilde{u_j}}{\partial x_i}\right) - \frac{1}{3}\frac{\partial \widetilde{u_k}}{\partial x_k}\delta_{ij}\ ;
\end{aligned}$$

and

$$\begin{aligned} \tau_{ij} &= \bar{\rho}\left(\widetilde{u_i u_j} - \tilde{u}_i \tilde{u}_j\right), \quad (2.15) \\ q_j &= \bar{\rho}\left(\widetilde{T u_j} - \widetilde{T}\tilde{u}_j\right) \quad (2.16) \end{aligned}$$

are the SGS stress and SGS heat flux, respectively. In Eq. (2.11), the expressions for $E$ and $H$ are

$$\bar{\rho}\widetilde{E} = C_v \bar{\rho}\widetilde{T} + \frac{1}{2}\bar{\rho}\tilde{u}_i\tilde{u}_i + \bar{\rho}k \quad (2.17)$$

and

$$\begin{aligned} H = & -\frac{\partial}{\partial x_j}\left[\frac{1}{2}\left(\bar{\rho}\widetilde{u_i u_i u_j} - \bar{\rho}\widetilde{u_i u_i}\tilde{u}_j\right)\right] - \frac{\partial}{\partial x_j}\left[\frac{5}{3}\left(\bar{\mu}\widetilde{u_j\frac{\partial u_k}{\partial x_k}} - \bar{\mu}\tilde{u}_j\frac{\partial \tilde{u}_k}{\partial \tilde{x}_k}\right)\right] \\ & + \frac{\partial}{\partial x_j}\left[\bar{\mu}\frac{\partial k}{\partial x_j}\right] + \frac{\partial}{\partial x_j}\left[\bar{\mu}\frac{\partial}{\partial x_i}\left(\frac{\tau_{ij}}{\bar{\rho}}\right)\right], \end{aligned} \quad (2.18)$$

where $k$ in equations (2.17) and (2.18) is the SGS kinetic energy defined by

$$\bar{\rho}k = \frac{1}{2}\tau_{kk} = \frac{1}{2}\bar{\rho}\left(\widetilde{u_k u_k} - \tilde{u}_k\tilde{u}_k\right). \quad (2.19)$$

Two assumptions have been made to derive the above equations. First, the filtering operations and derivatives are assumed to be commutative. Second, the kinematic viscosity $\nu$, specific heats $C_p$ and $C_v$, and Prandtl number $Pr$ are assumed to be spatially uniform over the filter width, so that

$$\overline{\sigma_{ij}} = \overline{2\rho\nu S^*_{ij}} = 2\bar{\rho}\nu\widetilde{S^*_{ij}} = 2\bar{\mu}\widetilde{S^*_{ij}} = \widetilde{\sigma_{ij}} \quad (2.20)$$

and

$$\overline{Q_j} = \overline{\frac{\mu C_p}{Pr}\frac{\partial T}{\partial x_j}} = \frac{\bar{\mu}C_p}{Pr}\frac{\partial \widetilde{T}}{\partial x_j} = \bar{\kappa}\frac{\partial \widetilde{T}}{\partial x_j}. \quad (2.21)$$

The SGS stress, SGS heat flux and the first two terms in Eq. (2.18) can not be computed directly from the resolved quantities. Models for these terms are discussed below.

### 2.3.2 Dynamic Smagorinsky Model (DSM)

Early work on LES (or SGS modeling) dates back to 1960s, with the background of meteorological applications. The Smagorinsky model [50, 32] is an eddy viscosity model which contains a model coefficient $C_s$ that must be determined *a priori*. However $C_s$ is problem dependent, and in principle should be a function of time and space. To avoid the need to prescribe or tune the model coefficient, Germano *et al.* [51] devised the Dynamic Smagorinsky Model (DSM), where the model coefficient is dynamically calculated during the simulation using the resolved scales. The dynamic procedure uses the assumption of scale invariance by applying the coefficient obtained from the resolved scales to the SGS range. This is referred to as the Germano identity and has become the basis of several dynamic models. Many variants of Smagorinsky models have been developed, such as SGS kinetic energy models [32, 33, 34], spectral eddy viscosity models [52, 53] and structure function models [54, 55, 56]. The reader is referred to the review papers by Lesieur & Mètais [57] and Meneveau & Katz [58] for past SGS model developments. Most of these models are either developed for incompressible flows or restricted to flows with simple geometries. Relatively fewer models have been developed for compressible flows. The compressible DSM model developed by Moin *et al.* [28] is still the most popular model used in simulations of compressible flows.

In the compressible DSM, the $H$ term defined by Eq. (2.18) is assumed to be small and neglected. The SGS stress and SGS heat flux terms are modeled by

$$\begin{aligned} \tau_{ij} - \frac{\delta_{ij}}{3}\tau_{kk} &= -2C_s\bar{\rho}\Delta^2|\widetilde{S}|\widetilde{S^*_{ij}} && (2.22)\\ q_j &= -\bar{\rho}\frac{C_s\Delta^2|\widetilde{S}|}{Pr_T}\frac{\partial\tilde{T}}{\partial x_j} && (2.23)\end{aligned}$$

and Yoshizawa's formula is used to model $\tau_{kk} = 2\bar{\rho}k$; i.e.

$$\tau_{kk} = 2C_I\bar{\rho}\Delta^2|\widetilde{S}|^2 \tag{2.24}$$

where $|S| = \sqrt{2S_{ij}S_{ij}}$. The model coefficients $C_s$, $C_I$, $Pr_T$ are determined dynamically by the Germano identity, which assumes similarity of SGS quantities between the grid filter level and test filter level; for any term $a = \overline{\alpha\beta} - \bar{\alpha}\bar{\beta}$, we assume that on the test filter level, $A = \widehat{\overline{\alpha\beta}} - \widehat{\bar{\alpha}}\widehat{\bar{\beta}}$ holds. Here, $\widehat{\cdot}$ denotes test filtering. The Germano identity is then defined by $L = A - \hat{a} = \widehat{\bar{\alpha}\bar{\beta}} - \hat{\bar{\alpha}}\hat{\bar{\beta}}$. Assume the model for $a$ is $a = C \cdot m$, where $m$ is a function of the resolved (grid filter level) quantities; then at the test filter level, $A = C \cdot M$, where $M$ takes similar form as $m$ but is a function of the test-filtered quantities. Substituting the models for $A$ and $a$, Germano identity becomes

$$L = \widehat{\bar{\alpha}\bar{\beta}} - \hat{\bar{\alpha}}\hat{\bar{\beta}} = C\left(M - \hat{m}\right). \tag{2.25}$$

Both sides of equation (2.25) may be calculated from the resolved variables and the model coefficient $C$ can be solved dynamically as

$$C = \frac{\widehat{\bar{\alpha}\bar{\beta}} - \hat{\bar{\alpha}}\hat{\bar{\beta}}}{(M - \hat{m})}. \tag{2.26}$$

$C$ varies with time and space. Finally, to avoid computational instability, $C$ is regularized using a combination of least-square [59] and volume averaging, e.g. the formula for the model coefficient of SGS stress $C_s$ is

$$C_s \Delta^2 = \frac{1}{2} \frac{\left\langle L^*_{ij} M^*_{ij} \right\rangle}{\left\langle M^*_{ij} M^*_{ij} \right\rangle}$$

where

$$\begin{aligned} L_{ij} &= \left( \frac{\widehat{\overline{\rho u_i}\,\overline{\rho u_j}}}{\bar{\rho}} \right) - \frac{\widehat{\overline{\rho u_i}}\,\widehat{\overline{\rho u_j}}}{\hat{\bar{\rho}}} \\ L^*_{ij} &= L_{ij} - \frac{1}{3}\delta_{ij} L_{kk} \\ M^*_{ij} &= \bar{\rho}\widehat{|\widetilde{S}\widetilde{S}^*_{ij}|} - \hat{\bar{\rho}} \left( \frac{\widehat{\Delta}}{\Delta} \right)^2 |\widehat{\widetilde{S}}|\widehat{\widetilde{S}^*_{ij}}. \end{aligned} \tag{2.27}$$

Here, $\langle \cdot \rangle$ denotes spatial average over homogeneous directions. Expressions for $Pr_t$ in the SGS heat flux $q_j$ and other details about the compressible DSM may be found in Moin *et al.*'s work [28].

# Chapter 3

# Study of high speed jets in crossflow using large-eddy simulations

Large-eddy simulations (LES) are used to study an under-expanded sonic jet injected into a supersonic crossflow and an over-expanded supersonic jet injected into a subsonic crossflow, where the flow conditions are based on Santiago *et al.*'s (1997) and Beresh *et al.*'s (2005) experiments, respectively. The simulations successfully reproduce experimentally observed shock systems and vortical structures. The time averaged flow fields are compared to the experimental results, and reasonable agreement is observed. The behavior of the flow is discussed, and the similarities and differences between the two regimes are studied. The trajectory and entrainment of the transverse jet is investigated. A modification to Schetz & Billigs theory [4] theory is proposed, which yields good prediction of the jet trajectories in the current simulations in the near field. Along the jet center streamline, the jet entrainment grow faster compared to turbulent free jets. In the very far field, the growth rates of jet entrainment decrease to values that are close to those for turbulent free jets. The Strouhal numbers of relevant flow structures are computed from power spectral densities. Many flow motions are observed to be correlated in sonic jet in supersonic crossflow. The frequencies in supersonic injection are observed to be higher than those in sonic injection.

Table 3.1.1: Summary of simulations

| Case | ID | Crossflow boundary layer | grid |
|---|---|---|---|
| sonic jet in supersonic crossflow | $A1$ | laminar | 13 million |
|  | $A2$ | turbulent | 25 million, refinement in case $A1$ boundary layer only |
|  | $A3$ | turbulent | 75 million |
| supersonic jet in subsonic crossflow | $B1$ | laminar | 15 million |
|  | $B2$ | turbulent | 27 million, refinement in case $B1$ boundary layer only |

## 3.1 Simulation Details

### 3.1.1 Problem statement

The current study considers two of the most common regimes of high-speed jets in crossflow: a sonic jet injected into a supersonic crossflow, and a supersonic jet injected into a subsonic crossflow. The flow conditions are based on the experiments of Santiago & Dutton [2] and that of Beresh *et al.* [3, 19, 20], respectively. For sonic injection, the free stream Mach number is $M_\infty = 1.6$ and the Reynolds number based on the free stream velocity and jet diameter $D$ is $Re_D = 5.9 \times 10^4$. The density and pressure ratio between the nozzle chamber and crossflow are $\rho_{0j}/\rho_\infty = 5.5$ and $p_{0j}/p_\infty = 8.4$, which results in a jet-to-crossflow momentum flux ratio of $J = 1.7$. The boundary layer thickness, $\delta_{99}/D = 0.775$, is matched at $x/D = -5$. For supersonic injection, the free stream Mach number is $M_\infty = 0.8$, the nominal jet exit Mach number is $M_j = 3.73$, the jet-to-crossflow momentum ratio is $J = 10.2$, the density, pressure and temperature ratio between the nozzle chamber and crossflow are $\rho_{0j}/\rho_\infty = 47.1$, $p_{0j}/p_\infty = 49.1$ and $T_{0j}/T_\infty = 1.05$, respectively. The Reynolds number is $Re_D = 3.1 \times 10^4$ based on free stream conditions and the jet diameter $D$. The boundary layer thickness, $\delta_{99}/D = 1.553$, is matched at $x/D = 26.65$ in absence of the transverse jet. Table 3.1.1 summarizes the simulations performed in the current study. Both laminar and turbulent crossflow boundary layers have been considered for each regime. For turbulent inflow cases, grid refinement is performed in the near wall region to resolve and sustain the turbulent boundary layer before it interact with the transverse jet. The grid resolution of the other regions is similar to that of the laminar inflow cases, so that the effect of crossflow boundary layer type can be evaluated. In case $A3$ (sonic injection), the mesh is further refined, primarily outside of the boundary layer wherein the influence of grid resolution is investigated. Note that, in the experiments, the actually Reynolds numbers are $Re_D = 2.4 \times 10^5$ and $Re_D = 1.9 \times 10^5$ for sonic injection and supersonic injection, respectively. In the current simulations, the Reynolds number is reduced, which results in $Re_\theta \approx 4500$ in the crossflow turbulent boundary layer; so that the crossflow turbulent boundary layer can be reasonably resolved by the current LES without wall models. The Reynolds numbers in the current simulations are around 1/4 and 1/6 of the actual conditions, which is still high. It is therefore assumed that this reduction of Reynolds numbers should not affect much the overall flow structure and mean flow quantities.

### 3.1.2 Algorithm

The spatially filtered compressible Navier-Stokes equations for an ideal gas are solved in conservative form:

$$
\begin{aligned}
\frac{\partial \bar{\rho}}{\partial t} &= -\frac{\partial \left(\bar{\rho}\widetilde{u_j}\right)}{\partial x_j}, \\
\frac{\partial \left(\bar{\rho}\widetilde{u_i}\right)}{\partial t} &= -\frac{\partial}{\partial x_j}\left(\bar{\rho}\widetilde{u_i}\widetilde{u_j} + \bar{p}\delta_{ij} - \widetilde{\sigma_{ij}} + \tau_{ij}\right), \qquad (3.1) \\
\frac{\partial}{\partial t}\left(\bar{\rho}\widetilde{E}\right) &= -\frac{\partial}{\partial x_j}\left(\bar{\rho}\widetilde{E}\widetilde{u_j} + \bar{p}\widetilde{u_j} - \widetilde{\sigma_{ij}}\widetilde{u_i} - \overline{Q_j} + C_p q_j\right), \qquad (3.2) \\
\bar{p} &= \bar{\rho}R\widetilde{T},
\end{aligned}
$$

where $\rho$, $u_i$, $p$, $E$, $\sigma_{ij}$ and $Q_j$ are density, velocity, pressure, specific total energy, viscous stress and heat flux, respectively. Here,

$$
\bar{\phi}\left(x\right) = \int_\Omega G_\Delta\left(x, y\right)\phi\left(y\right)dy \qquad (3.3)
$$

denotes the spatial filtering of $\phi(x)$. $G_\Delta(x,y)$ is the kernel of the filter which satisfies the normalization condition

$$\int_\Omega G_\Delta(x,y)\,dy = 1. \tag{3.4}$$

For compressible flows, density weighted (Favre) filtering is applied, i.e.

$$\tilde{\phi} = \frac{\overline{\rho\phi}}{\bar{\rho}}. \tag{3.5}$$

In equations (3.1) and (3.2), $\tau_{ij}$ and $q_j$ are the SGS stress and SGS heat flux defined as

$$\begin{aligned} \tau_{ij} &= \bar{\rho}\left(\widetilde{u_i u_j} - \widetilde{u}_i\widetilde{u}_j\right) && (3.6)\\ q_j &= \bar{\rho}\left(\widetilde{Tu_j} - \widetilde{T}\widetilde{u_j}\right). && (3.7) \end{aligned}$$

The compressible Dynamic Smagorinsky Model (DSM) [28] is used, i.e.,

$$\begin{aligned} \tau_{ij} - \frac{\delta_{ij}}{3}\tau_{kk} &= -2C_s\bar{\rho}\Delta^2|\widetilde{S}|\widetilde{S^*_{ij}} && (3.8)\\ q_j &= -\bar{\rho}\frac{C_s\Delta^2|\widetilde{S}|}{Pr_T}\frac{\partial \tilde{T}}{\partial x_j}. && (3.9) \end{aligned}$$

Here $S_{ij}$ is the strain rate tensor, $S^*_{ij} = S_{ij} - \frac{1}{3}\delta_{ij}S_{kk}$ is traceless strain rate tensor, and

$$\tau_{kk} = 2C_I\bar{\rho}\Delta^2|\widetilde{S}|^2, \tag{3.10}$$

where $|S| = \sqrt{2S_{ij}S_{ij}}$, and $C_s$, $C_I$, $Pr_T$ are model coefficients that are determined dynamically by the Germano identity [51].

The above equations are solved using an algorithm developed for unstructured grids by Park & Mahesh [1]. The algorithm employs a least–square method for flux reconstruction on faces of control volumes (CV), which has better spectral resolution than the $4^{th}$ order central difference scheme at high wavenumbers, is more accurate than a simple symmetric reconstruction, and more stable than a standard least–square reconstruction. A viscous flux splitting technique is applied, which ensures that the dominant incompressible component only depends on the nearest neighbours and is therefore more accurate at high wavenumbers, and devoid of odd-even decoupling. The algorithm uses a shock–capturing scheme that was originally proposed by Yee et al. [46] for structured meshes and was extended by Park & Mahesh [1] to unstructured meshes, and further

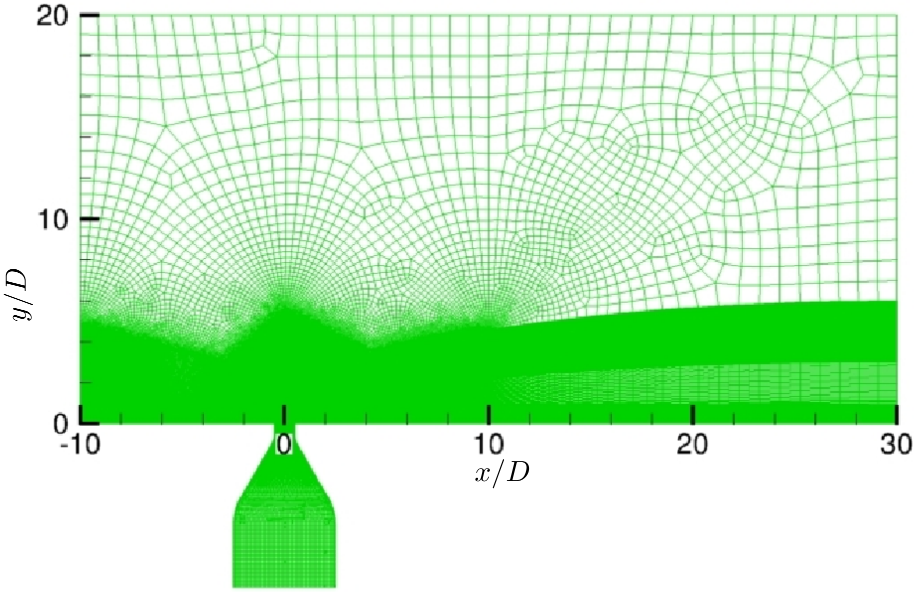

Figure 3.1: Computational mesh for sonic jet in supersonic crossflow.

localized to reduce unnecessary numerical dissipation. The shock–capturing is implemented in predictor-corrector form. The predictor step (base scheme) is symmetric and non-dissipative, and is designed to accurately represent broadband turbulence; while the corrector step is a characteristic-based filter that is active only in the vicinity of discontinuities. Therefore, the overall scheme avoids unnecessary numerical dissipation. Park & Mahesh [1] describe this methodology in detail, including a validation study using shock/vortex interaction, shock tube problem, two-dimensional mixing layer and homogeneous turbulence. The methodology has also been shown to perform well in various complex flows such as supersonic boundary layer transition due to roughness element [60] and distributed roughness [47], and LES of decaying isotropic turbulence and shock/turbulence interaction [61].

### 3.1.3 Computational Mesh and Boundary Conditions

Figure 3.1 shows the computational mesh and domain for the simulation of sonic jet in supersonic crossflow. Note that the origin of the coordinates is set at the center of jet exit, and the computational domain extends $40D \times 20D \times 30D$ in the axial, wall-normal and spanwise directions ($x$, $y$, and $z$) respectively. Preliminary computations showed that a domain of this size is large enough that the confinement effects of the boundary are absent. No-slip and adiabatic boundary conditions are imposed on the walls of the flat plate and the nozzle. Zero-gradient boundary conditions are applied to the top, the two sides and the outflow. At the jet inlet, the experimental chamber pressure and density are specified so that the desired Mach number and thermodynamic conditions are achieved at the jet exit in absence of the crossflow. A *tanh* vertical velocity profile is imposed which satisfies the continuity and no–slip wall boundary conditions. At the inlet of the crossflow, either laminar boundary layer profile or realistic turbulent boundary layer is imposed. The inflow turbulent data is generated from a separate simulation of boundary layer transition (shown in figure 3.2). The inflow generator operates under the same flow conditions (Reynolds number and Mach number) as in the simulation of jets in crossflow. The inflow data are then extracted at a location where the boundary layer thickness matches the experimental condition and stored temporally. The stored inflow data is then read by the simulation of jets in crossflow. Figure 3.3 shows the profiles of the mean streamwise velocity and turbulent intensities extracted at $x/D = 5$ upstream of the jet exit in absence of the jet. Reasonable agreement can be observed between the simulation of turbulent boundary layer with the proposed inflow generator and available DNS/experiment results.

Figure 3.4 shows the computational mesh for the simulation of supersonic jet in subsonic crossflow. In this simulation, the penetration of the jet is 1/3 of the height of experimental apparatus. For fair comparison, the computational domain has almost the same dimension as the wind tunnel test section to account for the confinement effect of the wind tunnel walls. The computational domain extends $100D \times 32D \times 32D$ in the axial ($x$), wall-normal ($y$) and spanwise ($z$) directions respectively, and the origin of the coordinates is again set to be the center of jet exit. Accordingly, adiabatic slip–wall boundary conditions are specified for the sides and the top; while the boundary conditions for the walls of the flat plate and the nozzle, the jet inlet and the inflow are set similarly to those for sonic injection.

As shown in figure 3.1 and figure 3.4, the computational mesh is unstructured and consists of hexahedral elements only. Fine grids are used at critical regions such as the surface of the flat plate, the nozzle wall and the near field of the jet. The grids

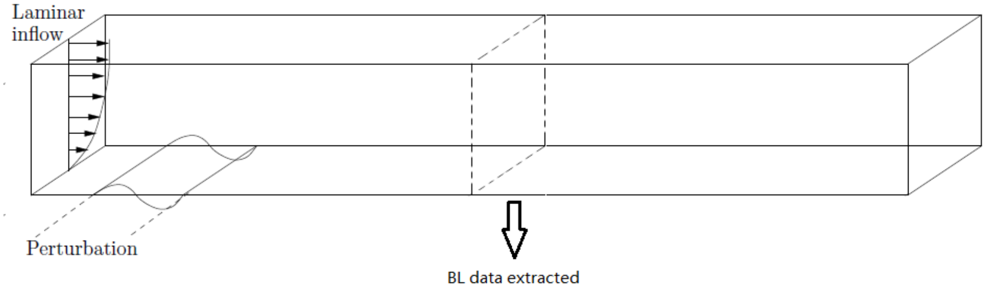

Figure 3.2: Schematic of turbulent inflow generator.

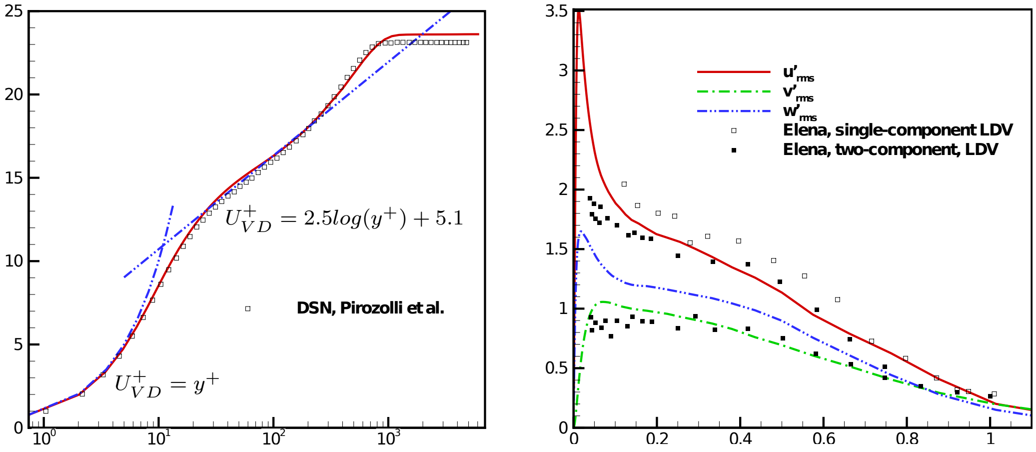

Figure 3.3: Mean velocity and turbulent intensity profiles of turbulent inflow boundary layer.

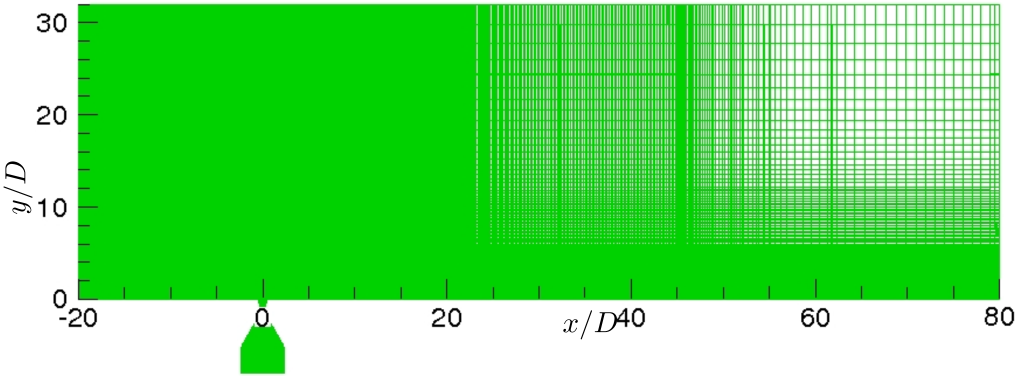

Figure 3.4: Computational mesh for supersonic jet in subsonic crossflow.

are then stretched quickly outside of those regions. The resolution is finest near the jet exit wall, where the grid spacing is $\Delta_r \approx 0.01D$ in radial direction, $\Delta_\theta \approx 0.03D$ in angular direction and $\Delta_y \approx 0.01D$ in $y$-direction for case $A1$ and $B1$ (laminar crossflow boundary layer). When the crossflow boundary layer is turbulent (case $A2$ and $B2$), $\Delta_r$ and $\Delta_\theta$ are meshed similarly to case $A1$ and $B2$, but $\Delta_y$ is refined accordingly with the grid refinement within the crossflow boundary layer, resulting in $\Delta_y \approx 0.001D$. Within the turbulent boundary layer, $\Delta_x \approx 0.03D$, $\Delta_y^{(1)} \approx 0.001D$ and $\Delta_z \approx 0.02D$ for sonic injection, and $\Delta_x \approx 0.045D$, $\Delta_y^{(1)} \approx 0.0015D$ and $\Delta_z \approx 0.03D$ for supersonic injection, resulting $\Delta_x^+ \approx 30$, $\Delta_y^{+(1)} \approx 1$ and $\Delta_z^+ \approx 20$ in wall unit for both cases. Here, the superscript "(1)" denotes the first grid point above the wall of the flat plate. At this grid resolution, the crossflow boundary layers can be reasonably predicted before they interact with the transverse jet (figure 3.3). In case $A3$, the grid resolution within the inflow boundary is similar to that in case $A2$, but the jet near field is substantially refined. For example, near the jet exit wall, the grid spacing are $\Delta_r \approx 0.001D$, $\Delta_\theta \approx 0.015D$ and $\Delta_y \approx 0.0005D$, respectively. The largest grid spacing is of order $\Delta_r \approx 1D$, as observed in figure 3.1 and figure 3.4. The resulting sizes of the computational meshes are listed in table 3.1.1 for each case. When laminar crossflow boundary layer is used, the computational meshes have approximately 13 million and 15 million control volumes for sonic injection and supersonic injection respectively. With turbulent crossflow boundary layer, a relatively coarse mesh with 25 million volumes was used at first for sonic injection, which is then refined to 75 million to evaluate the effect of grid resolution. For supersonic injection, the simulation with turbulent crossflow boundary layer uses around 27–million grid points.

The time advancement was explicit, and the computational time step is of order $0.001D/U_\infty$ for case $A1$ and $B1$; $0.0001D/U_\infty$ for case $A2$ and $B2$; and $0.00001D/U_\infty$ for case $A3$. The simulations are initialized with preliminary simulations of corresponding cases, where good representations of the flow fields have already been developed. The simulations are advanced for $40D/U_\infty$ and $100D/U_\infty$ period of time, for sonic and supersonic injection respectively, to allow any transients or flow adjustment to exit the domain before computing time-averaged statistics. The flow statistics are then collected for more than $80D/U_\infty$ and $200D/U_\infty$ non-dimensional time respectively to achieve acceptable convergence.

## 3.2 Comparison to experiments

### 3.2.1 Sonic jet in supersonic crossflow

Figure 3.5 compares the contours of mean Mach number and streamwise velocity on the central ($z/D = 0$) plane from the different simulation cases in table 3.1.1 to the experimental results. The most obvious difference between the simulation using laminar crossflow boundary layer (case $A1$) and other simulations (cases $A2$ and $A3$) or the experiment is the Mach number distribution within the crossflow boundary layer. Other than this, all of the simulation results are qualitatively similar to the experimental result. Close observation shows that the shape and inclined angle of the barrel shock are better predicted by simulations using turbulent crossflow boundary layer. This trend continues after grid refinement (case $A3$), where both the barrel shock and Mach disk are much better resolved.

Quantitatively, the streamwise and vertical velocity profiles are extracted at four different downstream locations on the central plane in figure 3.6. Note that there are more experimental data at $x/D = 3$ and $x/D = 5$, which are plotted together to indicate uncertainty of the experiment. Overall, the simulation results show reasonable agreement with the experimental data, and using turbulent inflow improves the agreement, especially in the far field. Some discrepancies are observed near the wall in the near field of the jet. Santiago & Dutton [2] note that their resolution in the near wall region is inadequate for this flow, and they do not observe the downstream recirculation region as observed by other studies (e.g. [15], [62]). The downstream recirculation shown in figure 3.5 indicates that at locations $x/D = 1$ and $x/D = 2$ the near wall region should have downwash vertical velocity and a relatively smaller mean streamwise velocity, as shown by the velocity profiles in the current simulations. Also, it is expected that the turbulent inflow boundary layer yields higher velocity gradients near the wall. The velocity profiles predicted from the fine grid simulation are close to those from the coarse grid simulation. However, the improvement owing to better grid resolution can be noticed from both the time-averaged quantities (figure 3.5) and the instantaneous flow field (section 3.3) where finer vortical structures can only be resolved with better grid resolution. Kawai & Lele [25] observed very similar behaviors when they compared

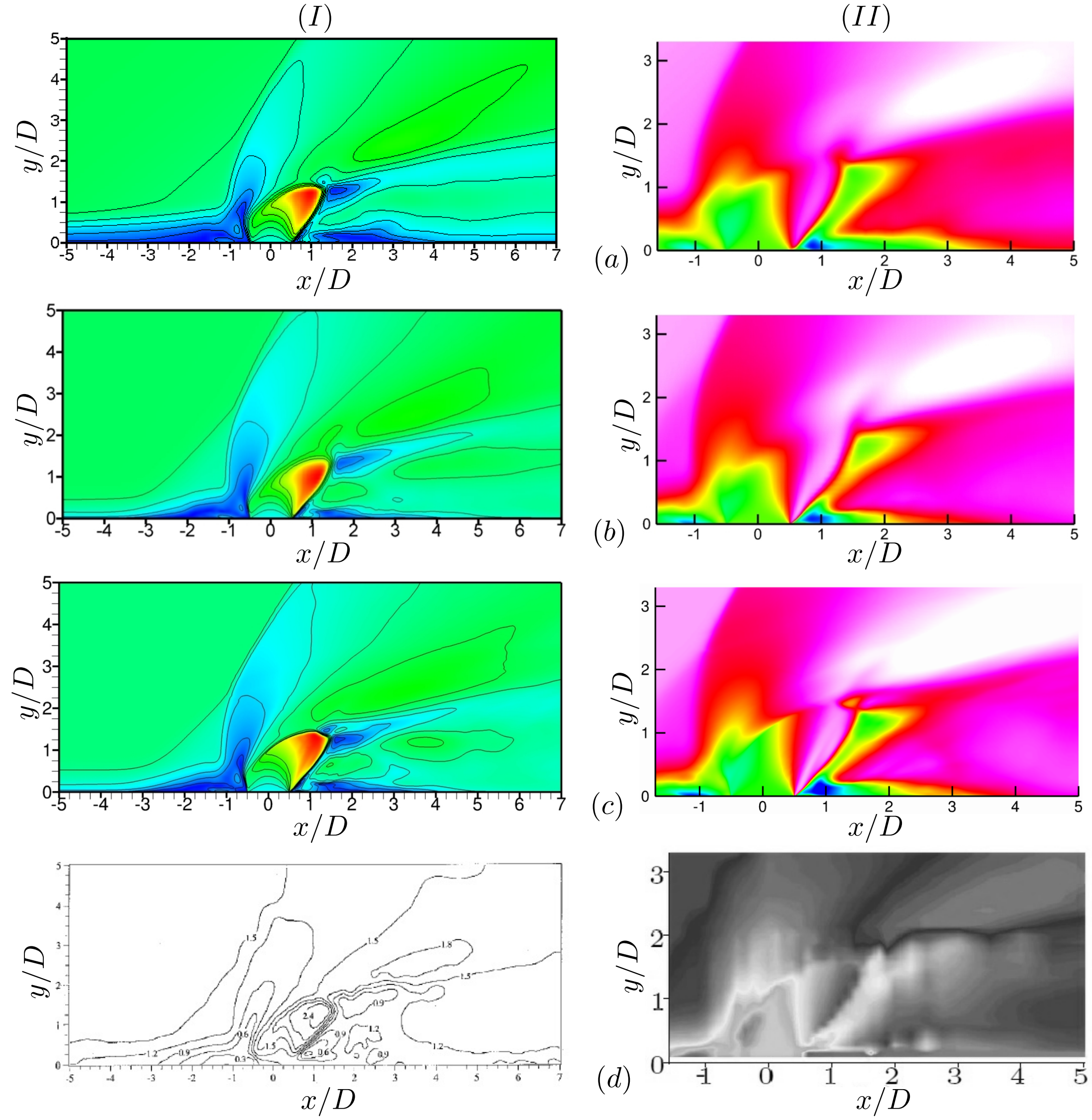

Figure 3.5: Time-averaged Mach number contours (column I) and $u$ velocity contours (column II) on central plane: row ($a$) – Case $A1$; row ($b$) – Case $A2$; row ($c$) – Case $A3$; row ($d$) – experiment.

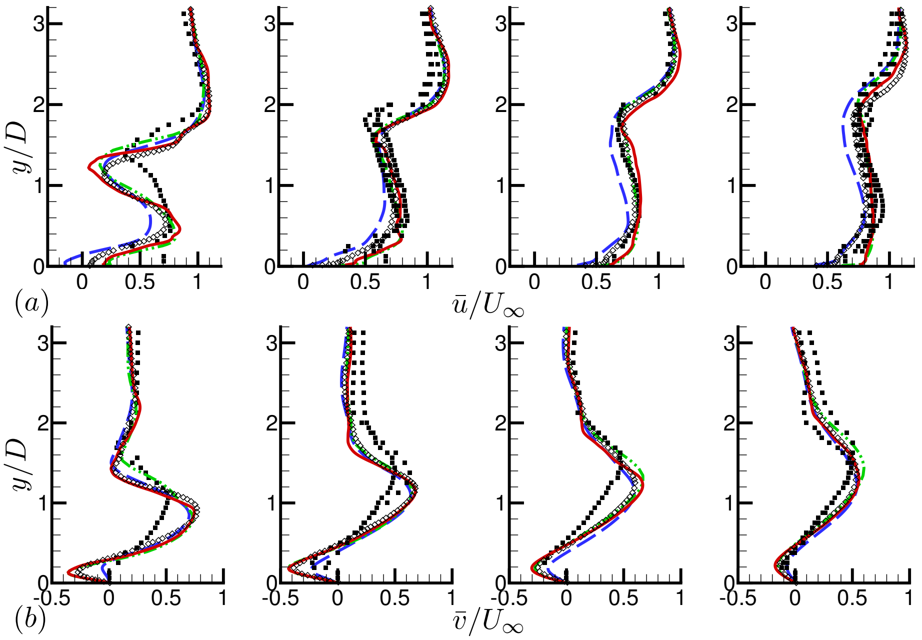

Figure 3.6: Comparisons of $(a)$ streamwise and $(b)$ wall-normal velocities between simulation and experiment at jet downstream locations $x/D = 2, 3, 4, 5$. solid lines – fine grid simulation; dash-dot-dot lines – coarse grid simulation; dashed lines – simulation using laminar crossflow boundary layer; filled symbols – experiment; hollow symbols – ILES of Kawai & Lele [25].

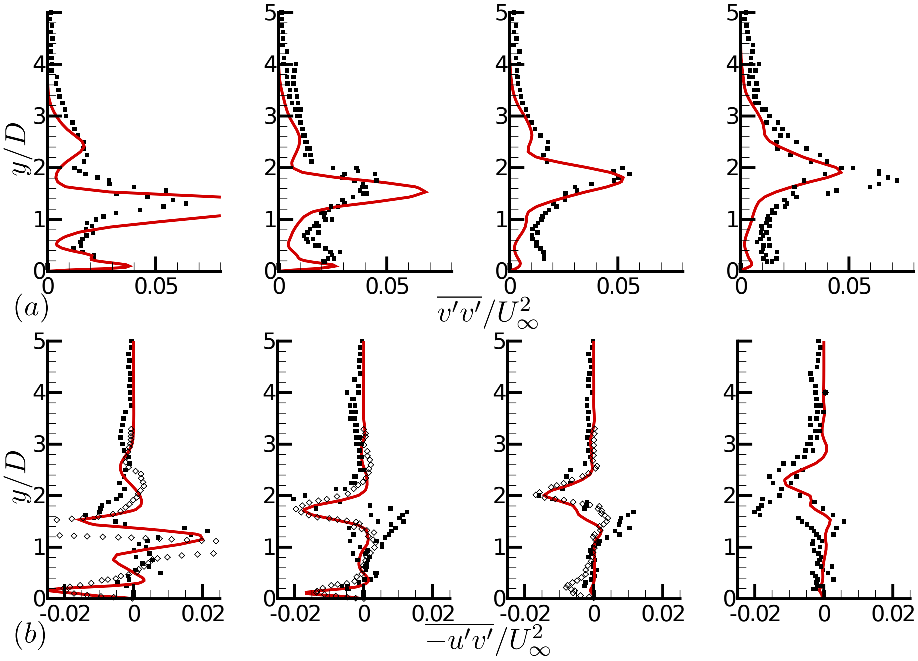

Figure 3.7: Comparisons of turbulent intensities, $(a)$ $\overline{v'v'}/U_\infty^2$ and $(b)$ $\overline{-u'v'}/U_\infty^2$, between simulation and experiment at jet downstream locations $x/D = 2, 3, 4, 5$. solid lines – simulation case $A2$; filled symbols – experiment; hollow symbols – ILES of Kawai & Lele [25].

their simulation results with the experiments and during the refinement of computational meshes. Their simulation results on the finest mesh with turbulent crossflow boundary layer are shown as the hollow symbols in figure 3.6, which are very close to the current LES. Note that in the current study, the Reynolds number is approximately 3 times as much as that in Kawai & Lele [25].

Figure 3.7 compares the resolved turbulent intensity profiles between the simulation using turbulent boundary layer and the experiment. The LES results of Kawai & Lele [25] are again compared at available locations. Generally, the agreement is good in the far field. In the near field, there are relatively large difference in quantity. However, the variations of the intensities along the $y$ coordinate agrees between the current simulation and experiment qualitatively, and the local peak locations in the curves match between the simulation and experiment approximately. The current simulation result is very close to that of Kawai & Lele [25] at $x/D = 3$ and $x/D = 4$. At $x/D = 2$, the current simulation result appears to agree better with the experiment. Overall, the comparison observed for the resolved turbulent kinetic energy suggests that the LES grid resolves most of the energy-containing motions.

### 3.2.2 Supersonic jet in subsonic crossflow

Figure 3.8 compares the time averaged streamwise and vertical velocity field with the experimental results. The vertical velocity fields predicted by the simulations show very good agreement with the experiment. In the simulation with laminar inflow, the low $u$-velocity region spreads more than the experiment, blurring the trajectory of minimum $u$-velocity. Using turbulent inflow improves this distribution of $u$-velocity and the agreement with experiment. The peak of the $u$-velocity deficit indicates the location of the jet core which has the largest impedance to the crossflowing freestream, while the peak of $v$-velocity marks the height of the CVP which induces the $v$-velocity component on the symmetrical plane. It can be observed that peaks of the $u$-velocity deficit are higher than those of $v$-velocity, because the kidney shaped CVP is below the jet core region.

Quantitatively, the mean velocity profiles are extracted at five different locations downstream of the jet, shown in figure 3.9. Consistent with figure 3.8, the peak of the streamwise velocity deficit using laminar inflow spreads wider than the experiment

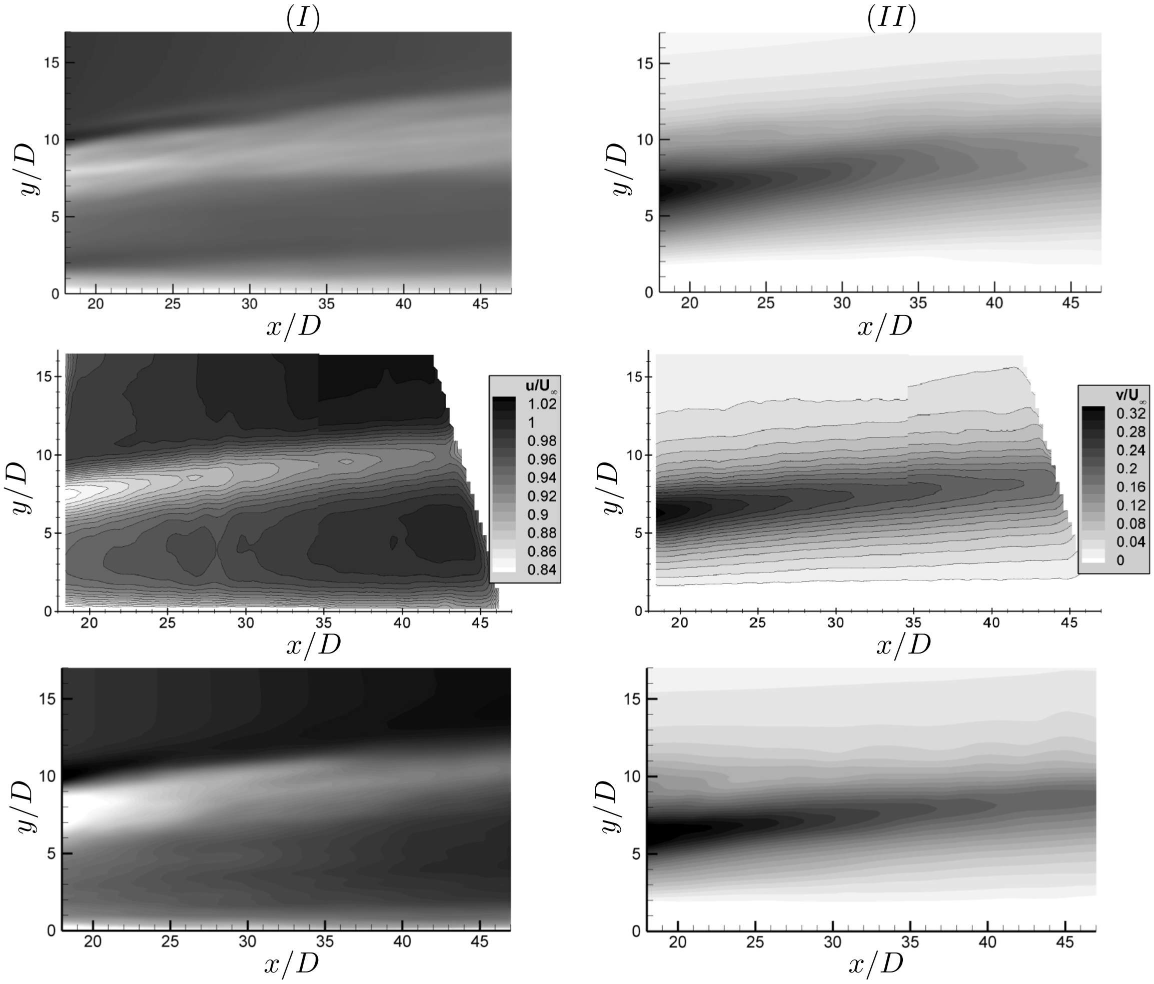

Figure 3.8: Time averaged $u$ velocity contour (column I) and $v$ velocity contour (column II) on central plane. First row, laminar inflow; Second row, experiment; Third row, turbulent inflow.

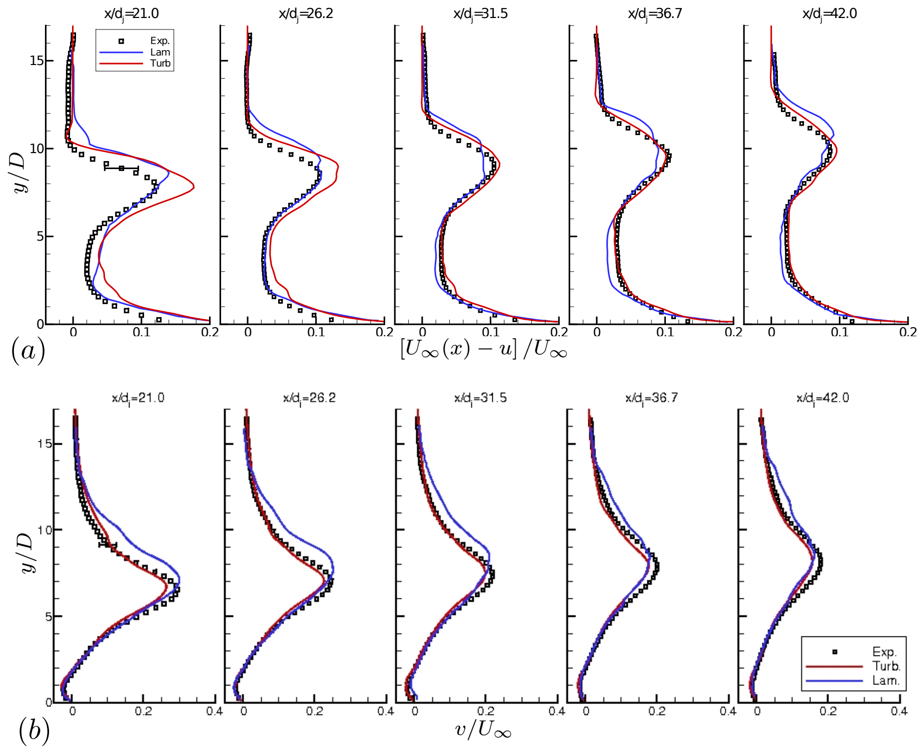

Figure 3.9: Comparisons of $(a)$ streamwise velocity and $(b)$ wall-normal velocity profiles between simulation and experiment at jet downstream locations x/D = 21, 26.2, 31.5, 36.7, 42.0. lines = simulations, symbols = experiment.

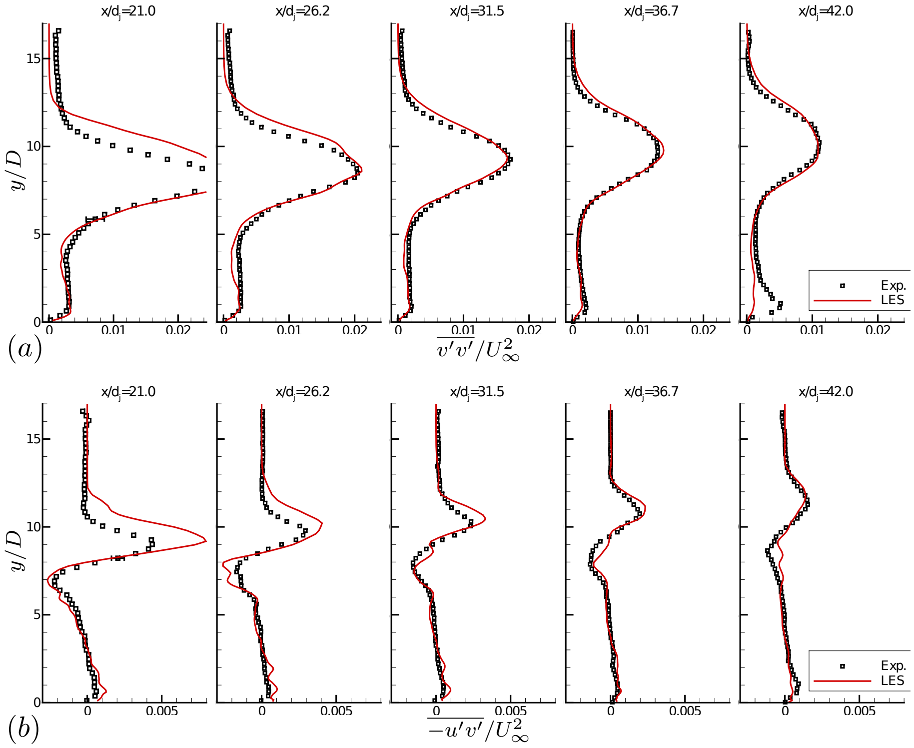

Figure 3.10: Comparisons of Reynolds stress $(a)$ $\overline{v'v'}/U_\infty^2$ and $(b)$ $\overline{-u'v'}/U_\infty^2$ between simulation and experiment at jet downstream locations x/D = 21, 26.2, 31.5, 36.7, 42.0. lines = simulation case $B2$, symbols = experiment.

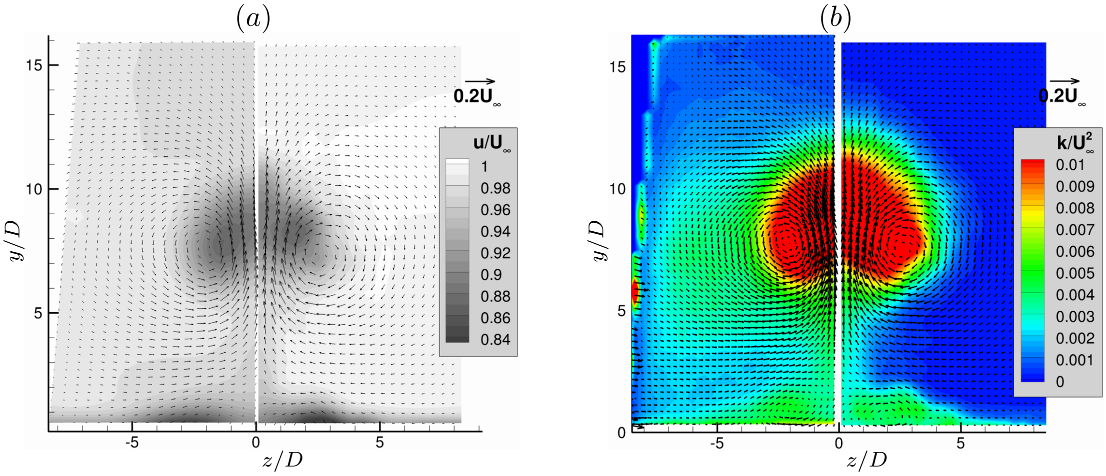

Figure 3.11: Comparisons of contours of (*a*) streamline velocity and (*b*) turbulent kinetic energy on the crossplane at $x/D = 33.8$ downstream of the jet. The in-plane velocity vector fields are superposed on each contour. In each figure, the left half is the experimental result, and the right half is from the current LES.

result at each location, which is improved by using turbulent inflow, especially in the far field. In terms of the vertical velocity, the simulation using turbulent inflow shows very good agreement with the experiment, while using laminar inflow over-predicts the trajectory of the jet defined by the heights of peak $v$. This is reasonable, because the laminar boundary layer has less momentum near the wall, which makes it easier to be penetrated [63]. Turbulent crossflow boundary layer can also cause more disturbance to the transverse jet and accelerate the "break down" of jet due to unsteadiness.

Figure 3.10 shows the intensity profiles at the five downstream locations in figure 3.9. When compared to the experiment, the agreement is very good. At $x/D = 21.0$, the simulation over-predicts the turbulent intensities slightly. At $x/D = 42.0$ near the wall, locally high level of $\overline{v'v'}$ is observed in the experiment, but not in the simulation. Observed from the distribution of $\overline{v'v'}$ near the wall at other locations, it is likely that the near-wall $\overline{v'v'}$ level decreases along the streamwise direction. Therefore, It does not appear to be physical for this locally high $\overline{v'v'}$ to occur near the wall at $x/D = 42.0$. Figure 3.11 (*a*) and (*b*) compare the mean streamwise velocity and turbulent kinetic

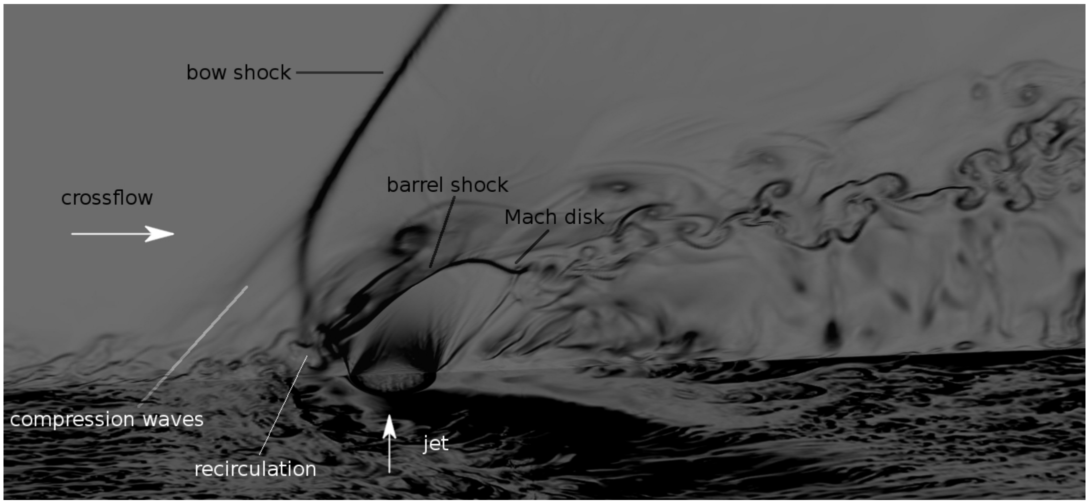

Figure 3.12: 3D view of instantaneous density gradient magnitude contours on symmetric and horizontal planes.

energy field with the experiment respectively on the crossplane at $x/D = 33.8$. In-plane velocity vector fields are superposed on each figure to show the CVP. The vector fields look almost identical with the experiment, and the contour fields show good agreement. Note that all of the statistics are evaluated at far downstream ($x/d > 20$). It is encouraging that the current simulations predict such accurate mean and second order turbulent statistics. In light of the good agreement between the simulations and experiments, the physics of high speed jets in crossflow are discussed based on the simulations using turbulent crossflow boundary layer (case $A3$ and $B2$) in the following sections.

## 3.3 Qualitative instantaneous flow behavior

Figure 3.12 shows contours of density gradient magnitude on the central and horizontal planes in case $A3$. The supersonic crossflow travels from left to right and contains a fully developed turbulent boundary layer. It sees the transverse jet as an obstacle, and responds by forming of a bow shock and a recirculation region in front of the jet. The recirculation region further induces a family of compression waves that merge into

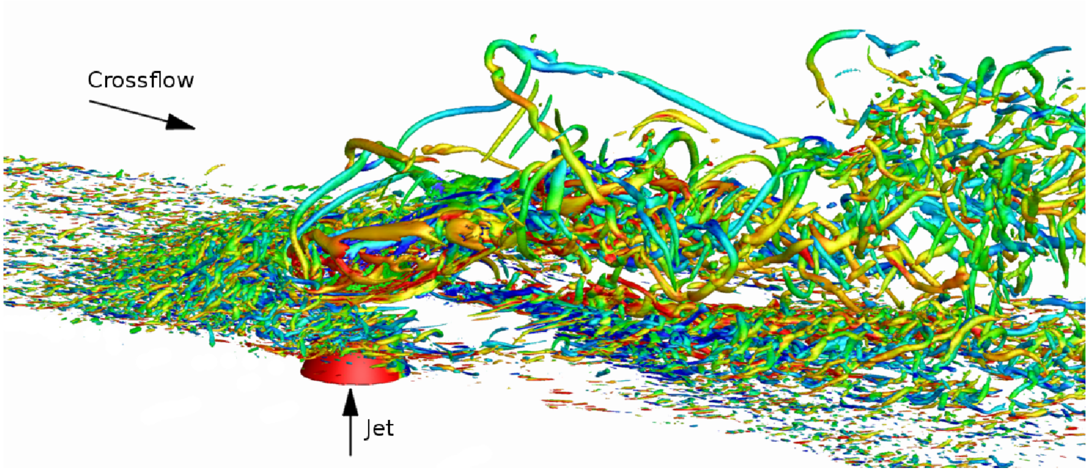

Figure 3.13: Iso-surface of Q criteria colored by streamwise vorticity $\omega_x$.

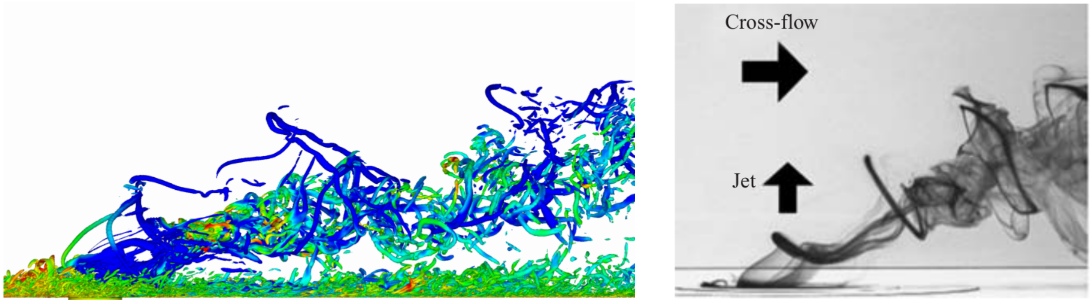

Figure 3.14: ($a$) Side view of iso-surface of Q criteria in figure 3.13; ($b$) image from the experiments of New *et al.* [64].

a “separation shock”. The separation shock and bow shock form a $\lambda$ shape, and are referred to as “$\lambda$ shock” by a number of studies (e.g. [24]). Exiting the orifice, the sonic jet tries to penetrate and expand, and sets up an inclined barrel shock and Mach disk on its periphery. On the windward side of the jet, the shear layer rolls up into vortices which detach from the jet boundary and are shed downstream. Coherent flow structures are observed downstream of the jet after the jet/crossflow interaction. These coherent vortices appear to be the Kelvin-Helmholtz vortices that originate from two shear layers. One is the shear layer between the jet fluid that pass through the Mach disk and that pass through the windward barrel shock; the other is the shear layer due to the velocity difference between the jet fluid that pass through the Mach disk and the ambient crossflow. We term the former shear layer as the upper inner shear layer, and the latter as the lower inner shear layer, to facilitate our discussions in the following sections. Note that, the inner shear layers and the resulting coherent vortices do not exist in low-speed jets in crossflow.

Figure 3.13 shows the iso-surface of the second invariant of velocity gradient tensor (Q–criterion) colored by the streamwise vorticity ($\omega_x$), which visualizes the instantaneous vortical structures. The flow is highly unsteady, and composed of turbulent eddies of different sizes. The recirculation bubbles wrap around the jet, and form horseshoe vortices. Downstream of the jet, there are two symmetric “irrotational” regions on the sides of the center plane, which contain few turbulent eddies. They correspond to the expansion and acceleration of the crossflow traveling around the jet. High density gradient magnitudes are observed in those regions (on the horizontal plane of figure 3.12). The jet plume has very complex structure with different dominant signs of $\omega_x$ on each side of the symmetrical plane. Statistically, this becomes the contour- rotating vortex pair. Also observed is an increase of turbulent eddy sizes downstream of the jet. These vortical structures are responsible for the mixing of the jet with the crossflow. Figure 3.14 (*a*) shows the side view of Q–criterion in figure 3.13, but colored by temperature. Figure 3.14 (*b*) is an image from the experiment of New *et al.* [64], which shows a low speed transverse jet with jet-to-crossflow velocity ratio $r = 1.0$. It is interesting to note the qualitative similarity between figure 3.14 (*a*) and figure 3.14 (*b*). It shows that the longitudinal vortices in figure 3.13 are actually part of the shear layer vortex “ring”, which connects the “shed” shear layer vortices in figure 3.12 with the jet plume.

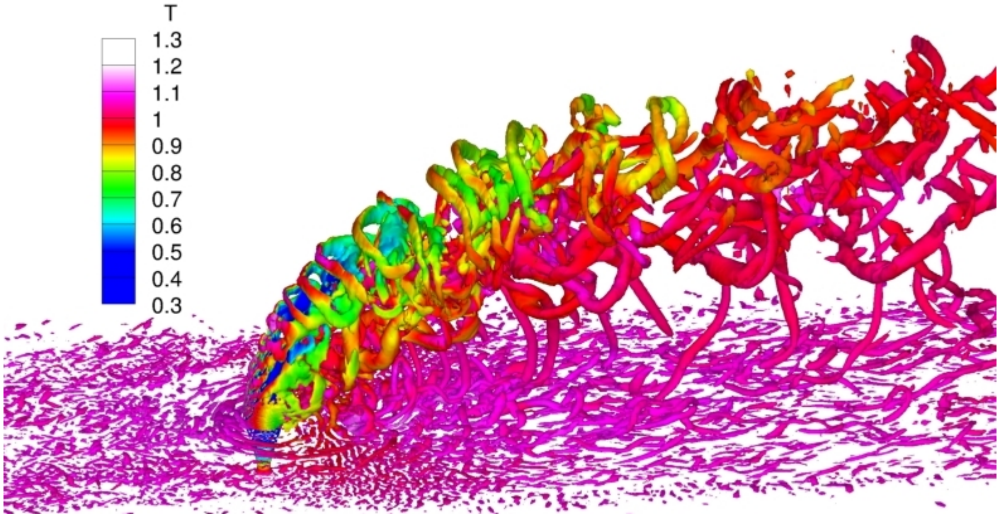

Figure 3.15: Iso-surface of the second invariant of velocity gradient tensor $Q$ colored by temperature $T$.

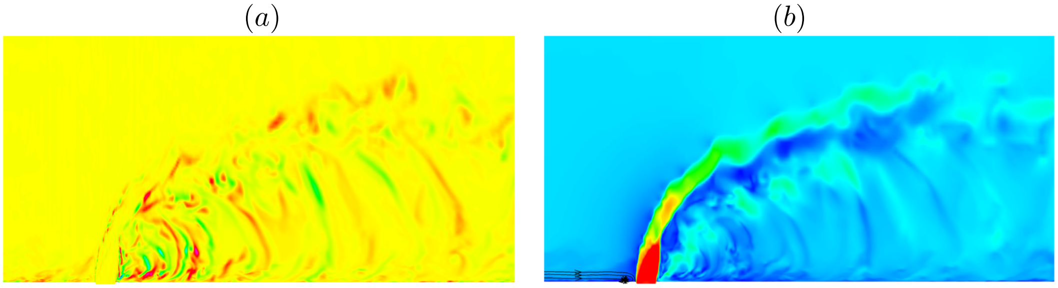

Figure 3.16: Instantaneous flow field of case $B2$ on the central plane: $(a)$ vertical vorticity component $(\omega_y)$ contour, $(b)$ Mach number contour.

Figure 3.15 shows the iso-surface of Q–criterion colored by temperature for the supersonic injection case $B2$. Again, the crossflow travels from left to right and contains a turbulent boundary layer. The turbulent inflow encounters the transverse supersonic jet, forming a recirculation region in front of the jet. The separation bubbles wrap around the jet and stretch along the streamwise direction, forming the horseshoe vortices. Note that the jet penetrates a lot more than the sonic jet due to much higher jet-to-crossflow momentum ratio. The shear layer vortices roll up on the windward side of the jet, grow and travel along with the jet, instead of "shedding" downstream as in the sonic injection case. These shear layer vortices have more regular ring-type structures surrounding the jet plume. The up-right cylindrical wake vortices are clearly seen, and the turbulent length scale in the boundary layer increases after the jet/crossflow interaction. The jet chamber conditions elaborated in section 3.1.1 develop a jet exit temperature of $T/T_\infty \approx 0.3$ at the jet exit, compared to $T/T_\infty = 1 \sim 1.1$ within the wall crossflow boundary layer. Due to this large temperature difference, the jet fluid and crossflow fluid can be approximately identified from the instantaneous temperature. It can be observed that the temperature of these cylindrical wake vortices is high and very close to that of the crossflow boundary layer. This agrees with Fric & Roshko [21]'s observation that wake vortices originate from the separation of the crossflow boundary layer.

Figure 3.16 ($a$) shows contours of the vertical vorticity component on the symmetry plane. It clearly shows that the wake vortices have different signs of circulation. It appears that the wake vortices with positive and negative $\omega_y$ arrange alternately most of the time, as noticed by past studies of low speed transverse jets (e.g. [21], [65]). Figure 3.16 ($b$) shows the instantaneous Mach number contour on the central plane. In front of the jet, the flow field resembles an incompressible jets in crossflow in that no bow shock and separation shock are formed because the crossflow is subsonic. The crossflow is retarded by the injected jet fluid, forming strong back pressure on the windward side of the jet which causes the separation of crossflow boundary layer, which can be visualized by the in-plane streamlines ahead of the jet. At the jet exit, the inclined barrel shock is clearly seen. Also observed are the shock cells within the jet plume, which cause pressure changes within the jet plume so that the jet boundary expands and contracts alternately. Also shown is the strong windward jet-crossflow shear layer, which rolls up

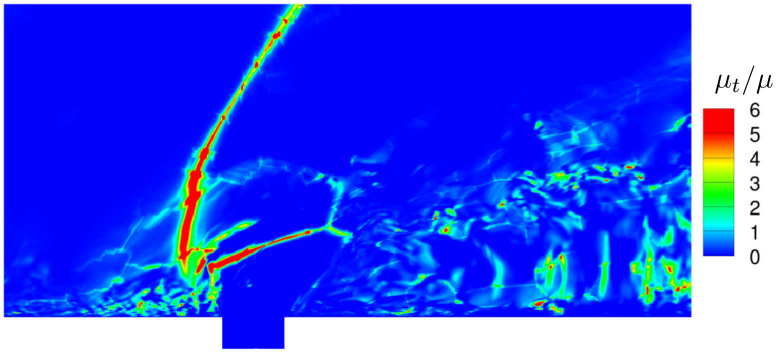

Figure 3.17: Instantaneous distribution of eddy viscosity in sonic injection.

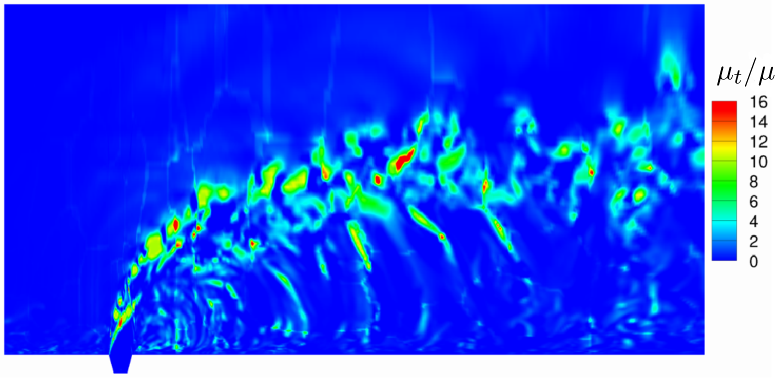

Figure 3.18: Instantaneous distribution of eddy viscosity in supersonic injection.

into vortices and causes the deflections of jet boundaries at the windward side of the jet.

Figures 3.17 and 3.18 shows the instantaneous contours of eddy viscosity normalized by molecular viscosity on the symmetrical plane for sonic injection and supersonic injection respectively. In DSM, eddy viscosity and eddy conductivity are defined as

$$\mu_t = C_s\bar{\rho}\Delta^2|\widetilde{S}| \tag{3.11}$$

$$\kappa_t = C_p\bar{\rho}\frac{C_s\Delta^2|\widetilde{S}|}{Pr_t} = \frac{C_p\mu_t}{Pr_t}. \tag{3.12}$$

Here $C_p$, $C_s$, $Pr_t$ and $|\widetilde{S}|$ are defined in section 3.1.2. It is observed in figures 3.17 and

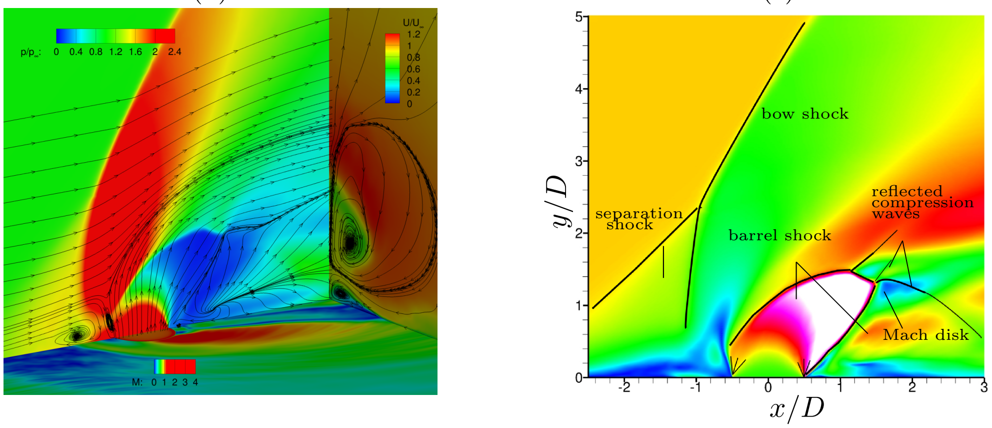
(a)

(b)

Figure 3.19: (*a*) 3D perspective of the mean flow field of sonic injection; (*b*) Mean Mach number contours on the central plane with marked shock system.

3.18 that, high eddy viscosity occurs after the shocks and in regions where energetic turbulent flow structures prevail such as jet plume, shear layer vortices, wake vortices and boundary layers. The undisturbed freestream, nozzle chamber and expansion regions have almost zero eddy viscosity. Note that the eddy viscosity in supersonic injection is larger than that in sonic injection. This is partially because the computational mesh is finer in sonic injection, so that less fluid motions are subgrid-scale.

## 3.4 Time-averaged flow features

Figure 3.19 (*a*) shows the 3D perspective of the mean flow field of the sonic jet in supersonic crossflow; where the central plane shows mean pressure contours, the near-wall horizontal plane shows mean Mach number contours, and streamwise velocity contours are shown on the downstream crossplane. The in-plane streamlines are superposed on the central– and cross– planes to show the flow patterns and vortical structures. Figure 3.19 (*b*) shows the mean Mach number, where dark lines are used to mark the shock waves. Extremely high pressure regions are observed behind the bow shock, and at the near wall region upstream of the jet, which sets up a adverse gradient near the wall. The adverse pressure gradient causes the crossflow boundary layer to separate, which further induces the separation shock in front of and above the major separation bubble. The

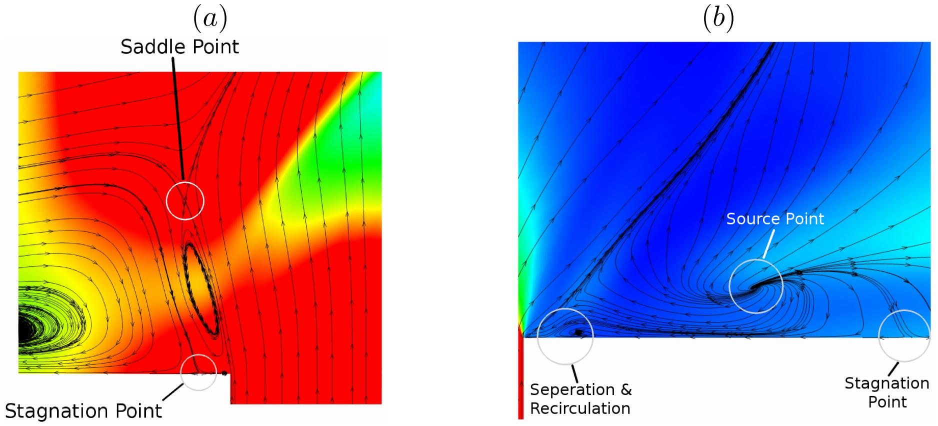

Figure 3.20: Close views of figure 3.19: (*a*) upstream of the jet; (*b*) downstream of the jet.

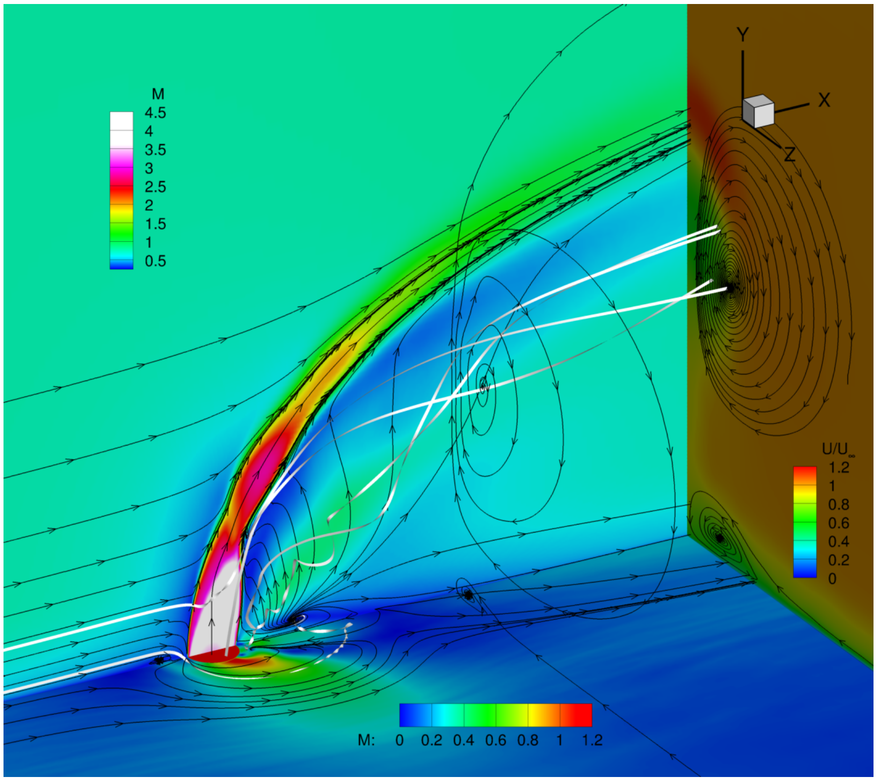

Figure 3.21: 3D perspective of mean flow field of supersonic injection superposed by surface and volume streamlines.

crossflow accelerates and expands when it travels around the jet, followed by decrease in pressure (central plane) and increase in Mach number (horizontal plane and figure 3.19 (*b*)). The Mach number contour on the horizontal plane shows that when traveling around the jet, the crossflow accelerates to supersonic speeds even very near the wall. Downstream of the jet, the pressure is extremely low, which induces reverse flow near the wall. The jet expands and accelerates (Figure 3.19 (*b*)) as it exits the nozzle exit and encounters the crossflowing freestream, forming an inclined barrel shock and Mach disk on its periphery. The streamlines show that the jet bends quickly towards the crossflow direction after it pass through the windward side barrel shock and the Mach disk. A source point is observed downstream of the jet on the central plane, which has also been observed in studies of incompressible jets in crossflow (e.g. [63], [66]). This originates from the reattachment of the crossflow after it travels around the jet. The streamlines on the downstream crossplane shows the CVP, as well as another pair of counter-rotating vortex pair near the wall. The CVP is perceived as the dominant mean flow structure downstream of the jet.

Figures 3.20 (*a*) and (*b*) show a close view of upstream and downstream streamlines, respectively. Upstream of the jet, a secondary separation bubble is observed which is referred to as the "hovering vortex" by a number of studies (e.g. [63]), and there is a stagnation point on the wall. A "saddle point" is found right above the "hovering vortex", which appears to be the intersection between the jet, crossflow, primary separation bubble and hovering vortex. Downstream of the jet, a large reverse flow region is observed below the source point. It separates as it approaches the jet exit from the leeward side, and forms a tiny separation bubble there. Further downstream, a stagnation point is predicted between the reverse flow and the main stream. The shock waves depicted in figure 3.12 are shown again in the mean Mach number contours in figure 3.19 (*b*). Additionally, the occurrence of reflected compression waves between the interaction of barrel shock and Mach disk can be conjectured from changes in the contours of Mach number and pressure, as well as the curvature of streamlines immediately downstream of the intersection of the leeward barrel shock and Mach disk. It appears that the upper reflection wave is induced by the velocity difference between the jet fluid that passes through the windward barrel shock (supersonic) and the jet fluid that goes through the Mach disk (subsonic). The lower compression wave seems to be due to the impingement of high speed upwardly entrained ambient crossflow on the low speed jet fluid that goes through the Mach disk. The reflected downwards compression wave is likely to impinge on the wall, and causes additional reflection and wall pressure rise (figure 3.23).

Figure 3.21 shows the 3D perspective of the mean flow field of the supersonic jet in subsonic crossflow. The central plane and horizontal plane show Mach number contours, and the crossplane shows the streamwise velocity contours. Surface streamlines are plotted to show the in-plane fluid motions. Similar to the sonic jet in supersonic crossflow, upstream and downstream recirculation regions are observed, as well as the CVP in the far field. Downstream of the jet, a source point is also observed on the central plane. The Mach number contours on the near wall horizontal plane show that the subsonic crossflow accelerates to supersonic speeds as it travel around the jet. The central plane shows very different shock structure from the sonic injection case. All the shocks are confined to the jet, and the crossflow appears to be devoid of shocks. As stated in section 3.3, there is no blow shock and separation shock when the crossflow is subsonic. The shapes of the barrel shock and Mach disk is very different from the sonic injection, due to different jet exit condition and jet-to-crossflow momentum ratio. There are approximately 3 discernible jet cells which decay as the jet evolves, and causes the jet to contract and expand alternately. Note that near the first jet contraction region, the downstream fluid appears to be aggressively engulfed, and the streamlines show suddenly turning towards the jet in that region. The downstream streamlines shows how the crossflow is entrained by the jet. Immediately downstream stream of the shock, the streamlines show a tornado-like pattern, which marks the early stage of the formation of the CVP. The upstream hovering vortex and downstream separation bubble are also observed in this case (not shown). However, the sizes of these vortices are tiny compared to those in the sonic injection case or the jet diameter.

## 3.5 Wall pressure, skin friction and near-wall streamline

Figure 3.22 compares the pressure distribution on the wall between sonic and supersonic injection cases. Near-wall streamlines are superposed on the wall planes. Both the distributions of pressure and near-wall streamlines show dramatic difference between the two regimes. In the sonic injection, the high pressure region in front of the jet is

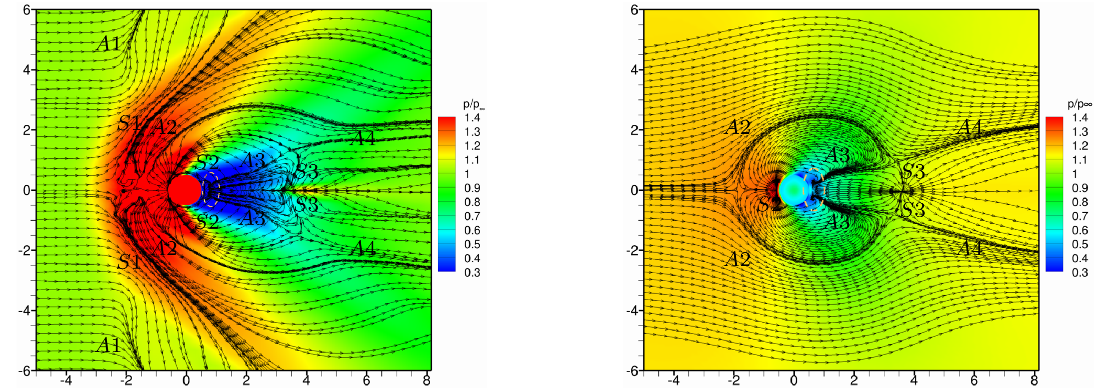
(*a*) (*b*)

Figure 3.22: Streamlines on horizontal plane adjacent to the wall, superposed on mean pressure field: (*a*) sonic injection; (*b*) supersonic injection.

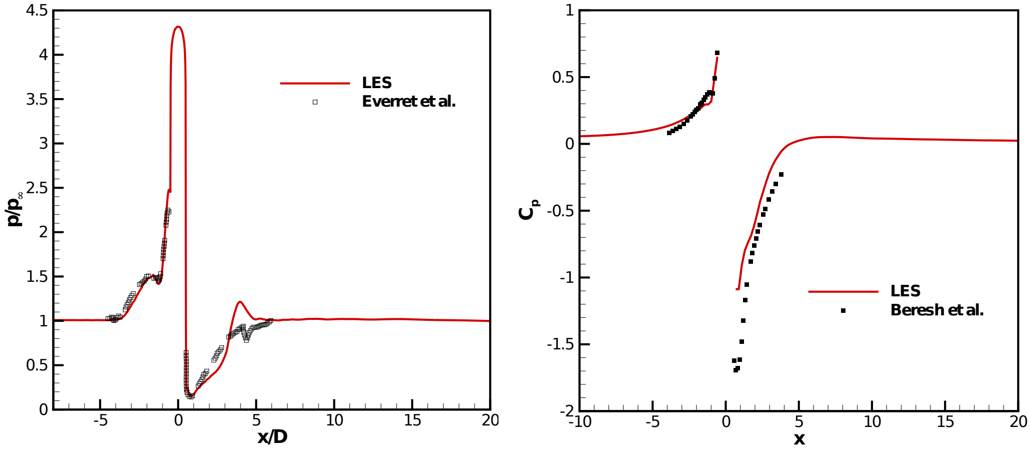
(*a*) (*b*)

Figure 3.23: Mean wall pressure distribution along central line: (*a*) case $A3$; (*b*) case $B2$.

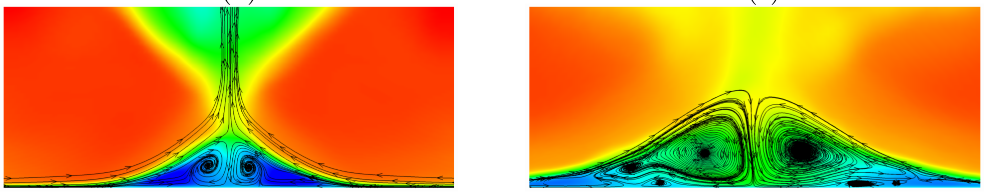
(*a*) (*b*)

Figure 3.24: Near wall $v - w$ streamlines at two different downstream crossplanes: (*a*) $x/D = 1.5$; (*b*) $x/D = 3.0$.

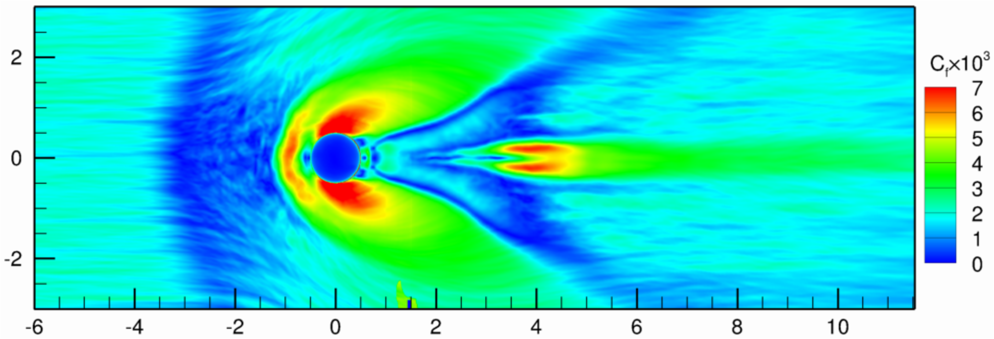

Figure 3.25: Contour of skin friction coefficients for sonic jet in supersonic crossflow.

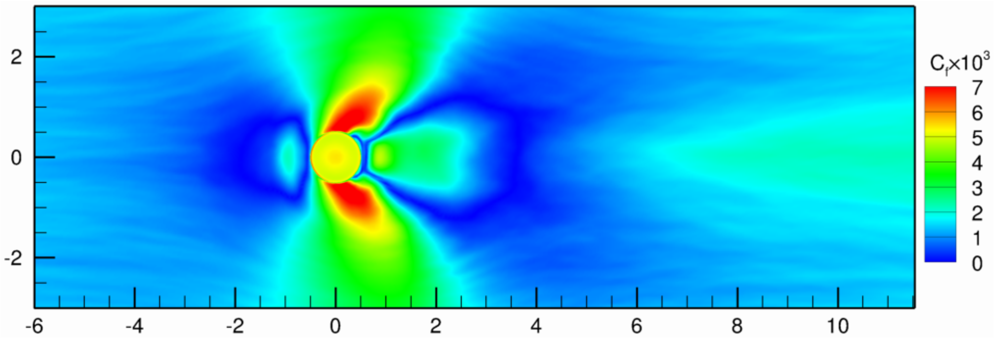

Figure 3.26: Contour of skin friction coefficients for supersonic jet in subsonic crossflow.

significantly larger than those in the supersonic injection, even when the high pressure region due to the bow shock is not accounted for. So is the low pressure region behind the jet. The value of the highest pressure in case $A3$ is higher than that in case $B2$, and the magnitude of the lowest pressure in case $A3$ is lower than that in case $B2$ as well. It is interesting to note that the back pressure region due to the blockage of the transverse jet in figure 3.22 ($a$) embraces the jet exit from the sides and extends to the rear of the jet. In contrast, in case $B2$, all the high pressure region is ahead of the jet exit centerline, which is more similar to the wall pressure distribution in flow past a cylinder. Figure 3.23 ($a$) and ($b$) show the distribution of the pressure and pressure coefficient $C_p$ for sonic injection and supersonic injection respectively, where $C_p = (p - p_\infty)/(\frac{1}{2}\rho u_\infty^2)$. The symbols are from the experiments of Everett & Morris [62] and Beresh *et al.* [18], respectively. For sonic injection, it is noticed that the maximum pressure downstream of the jet is at $x/D \approx 4.0$ on the center line, which may be related to the impingement of the downward reflected compression wave (figure 3.19) on the wall. The supersonic injection does not have similar pressure variation downstream of the jet, as shown in 3.23 ($b$).

Significantly more flow patterns are observed from the near-wall streamlines of sonic injection. In both figure 3.22 ($a$) and ($b$), labels starting with $A$ and $S$ are used to mark the attachment lines and separation lines, respectively. In figure 3.22 ($a$), the first pair of separation lines, $S1$, marks the foot of the bow shock. In front of it, the attachment lines $A1$ and their extrapolation to the symmetric line approximately marks the foot of the separation shock. The separation lines $S2$ are the head of the major separation bubble in front of the jet due to the adverse pressure gradient, while the attachment line $A2$ between $S1$ and $S2$ is the tip of the primary separation bubble. The region between $A2$ and $S2$ is where the horseshoe vortices form. Downstream of the jet, another pair of attachment lines $A3$ are observed, where the crossflow meet the reverse flow of the wake. Inside $A3$, there appear to be sub-level attachment lines. These are associated with the longitudinal secondary flows near the wall, which can be shown by the streamlines in crossplanes (figure 3.24). Also, the separation line $S3$ divide the wake region into reverse-flow-wake region and forward-flow-wake region, and the attachment lines $A4$ separates the crossflow and wake region in the far field. Again, secondary longitudinal motions are indicated by additional lines between lines ($A4$).

For supersonic injection (figure 3.22 (*b*)), there are no separation lines $S1$ due to the absence of the bow shock. Therefore, there are also no $A1$ attachment lines. Other lines correspond to the ones in figure 3.22 (*a*), and are labeled similarly. Lines with the same labels in both figures are due to similar flow mechanism, but are of different structures and shapes. In both figure 3.22 (*a*) and (*b*), there is a pair of “sink” points located symmetrically about the center line immediately downstream of the jet (within white dashed ellipse), which have (can only have) positive vertical velocity component (not shown). Based on figure 3.22, it is fair to conclude that the supersonic crossflow is much more significantly modified by the transverse jet than the subsonic crossflow is.

Figure 3.25 and figure 3.26 show the contours of skin friction coefficients ($C_f$) on wall plane. $C_f$ is calculated from the gradient of near wall tangential velocity component ($u_t$), i.e. $C_f = \mu_w(\partial u_t/\partial y)|_w$, where $\mu_w$ is the viscosity near the wall. This definition is appropriate in that it takes into account both the streamwise and spanwise velocity components, but it does not apply to the jet exit though certain contour levels are still shown at the nozzle exit in figure 3.25 and figure 3.26. In figure 3.25, approaching the jet, the skin friction first decreases because of the recirculation region in front of the jet. Moving downstream, the center of the primary separation bubble appears to have relatively large spanwise velocity component; therefore a small high skin friction region is observed in front of the jet. Immediately upstream of the jet the flow is almost stagnant, which results in low skin friction there. The supersonic case (figure 3.26) shows similar behavior in front of the jet, but has less changes in skin friction than that in the sonic injection case. On the sides of the jet for both cases, extremely high levels of skin friction are observed, which is due to the acceleration of the crossflow bypassing the jet. Downstream of the jets, figures 3.25 and 3.26 show very different behaviors. These complex wake structures in figure 3.22 (*a*) and 3.24 are again observed in figure 3.25. Inside the near wake region, the skin friction is of moderate level in both cases. But in this region, the skin friction of case $A3$ is lower than that in the center of primary separation bubble; while case $B2$ shows the opposite trend. There also appear to be a local maximum of $C_f$ near the jet on the center line of this wake region in case $A3$, which is not observed in case $B2$. This wake region is sightly closer to the jet exit in $B2$ than in case $A3$, which can also be observed figure 3.22. Further downstream of the jet, $C_f$ increases faster in case $A3$, and there exist two locally high $C_f$ region symmetric about

Table 3.6.1: Coefficients for laws of jet trajectory

| Fit | Researchers | a | b | c |
|---|---|---|---|---|
| power | Rogers (1971) | 0.387 | - 0.557 | 0.143 |
| | Rothstein & Wantuck (1992) | 2.173 | - 0.443 | 0.281 |
| | Gruber *et al.* (1997) | 1.23 | 0 | 1/3 |
| log | Mcdaniel & Graves (1986) | - 0.656 | 2.077 | 2.059 |
| | Rothstein & Wantuck (1992) | -0.6985 | 4.704 | 0.6373 |

the center line around between $x/d = 3$ and $x/d = 5$. By comparing with figure 3.22, this region is right downstream the separation line $S3$, where the wake has relatively high spanwise velocity component and starts to accelerate in the streamwise direction. Downstream of this region, the $C_f$ stays in moderate level within a slim band, which keeps decreasing along the streamwise direction. Out of this band, the average $C_f$ appears to be slightly lower than that in the undisturbed crossflow boundary layer. In figure 3.26, no such regions discussed above are observed. Far downstream, $C_f$ is higher near the centerline, and the high $C_f$ region keeps expanding along the streamwise direction. The averaged $C_f$ in the far downstream region appears to be higher than that of the inflow turbulent boundary layer.

## 3.6 Jet trajectory

Multiple definitions of jet trajectory exist; e.g. the local velocity maxima [67, 3] or the local scalar concentration maxima [65, 11, 13]. However, both concentration and velocity have multiple local maxima [67, 68], which makes the automatic determination of jet trajectory difficult. Similar to Muppidi & Mahesh [63], this paper defines the trajectory as the streamline originating from the center of the jet exit (center streamline) on the time averaged symmetry plane, which describes the path taken by the jet fluid more accurately and is more feasible in simulations.

The trajectories of the high speed jets in crossflow have been investigated by a

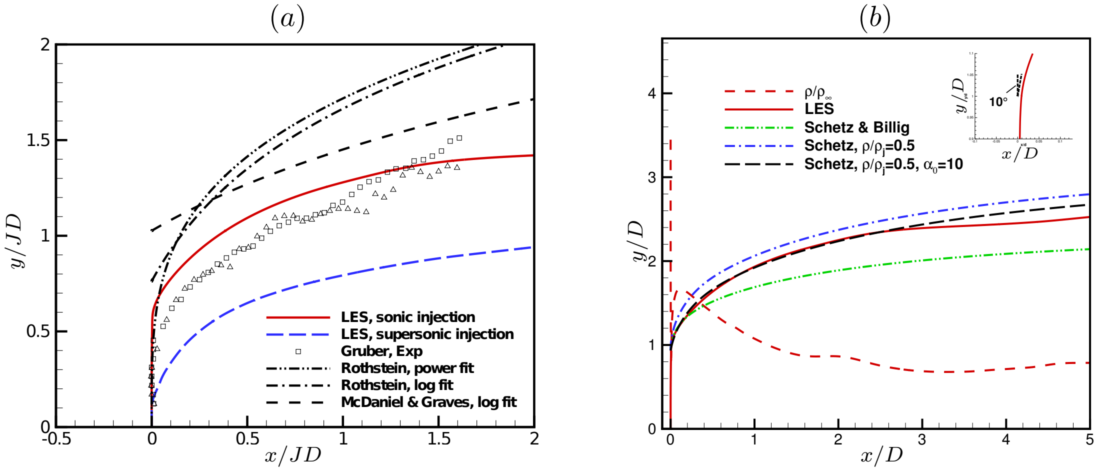

Figure 3.27: Trajectory of sonic jet in supersonic crossflow: (*a*) comparison with experimental data and empirical fits; (*b*) prediction of jet trajectory using modified theory of Schetz & Billig (1966).

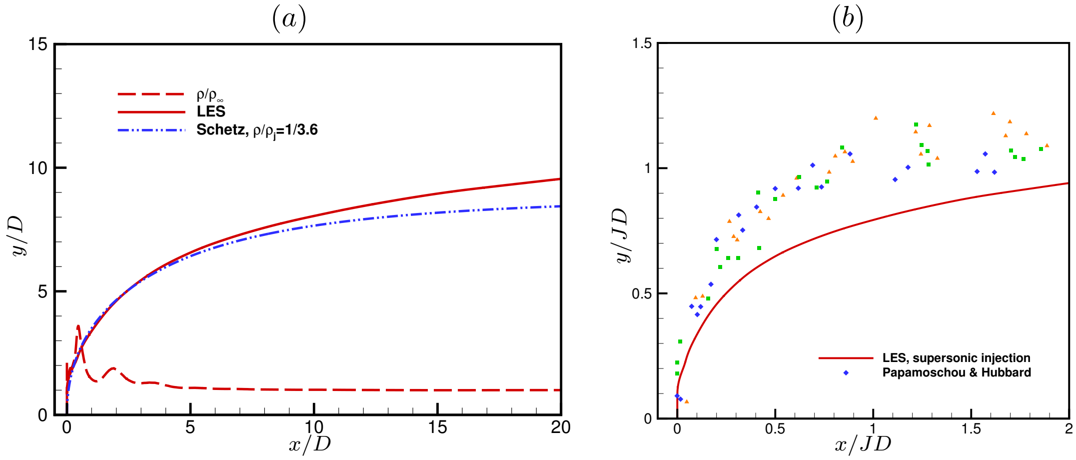

Figure 3.28: Trajectory of supersonic jet in subsonic crossflow. (*a*) prediction of jet trajectory using modified theory of Schetz & Billig (1966); (*b*) comparison with experimental data ($M_\infty = 2.0$, $J = 8.3$): $\blacksquare$ – $M_j = 2.1$, $\blacktriangle$ – $M_j = 2.8$, $\blacklozenge$ – $M_j = 3.5$.

substantial number of studies, all of which show that the jet-to-crossflow momentum ratio, $J$, is the dominant parameter that affects the jet trajectories. Generally, past work fits the jet trajectory data using a power law of form

$$\frac{y}{JD} = aJ^b \left(\frac{x}{JD}\right)^c \tag{3.13}$$

or a log law of form

$$\frac{y}{JD} = J^a ln \left[bJ \left(\frac{x}{JD} + \frac{c}{J}\right)\right]. \tag{3.14}$$

Here, $a$, $b$ and $c$ are coefficients that yield the best fit of the related experimental data. Table 3.6 summarizes the value of these coefficients used in different studies. Figure 3.27 ($a$) shows the jet trajectories in the current simulations, where the $x$ and $y$ coordinates are normalized by $JD$. The experimental data of Gruber *et al.* [11] and the empirical correlations from the studies of Rothstein & Wantuck [22] and Mcdaniel & Graves [16] are plotted together for comparison. It appears that the jet trajectory in the current simulation of sonic jet in supersonic crossflow agrees the best with the experiments of Gruber *et al.* [11]. Noting the diversity of the coefficients in table 7.1, it is not surprising to see in figure 3.27 ($a$) that the $JD$ scaling does not collapse various experimental and simulation data, and the jet trajectories under different flow conditions differ a lot from each other. However, changing the scaling law to widely used relations for incompressible flows (e.g. $\sqrt{J}D$) increases this scatter (not shown).

Schetz & Billig [4] analysed the force balance of a jet segment along the jet normal and axial directions, and derived a differential equation that can be used to predict the jet trajectory:

$$\frac{d\alpha}{d\bar{s}} = -\frac{C_D(\alpha)sin^2(\alpha)}{2.5\pi}\frac{1}{J}\left(\frac{\rho}{\rho_j}\right)(2.25 + 0.22\bar{s})^3 \tag{3.15}$$

where $\bar{s} = s/d$, and $C_D$ is a drag coefficient determined by

$$\begin{aligned} C_D &= 1.2 + (M_\infty sin\alpha)^{7/2} & 0 \leq M_\infty sin\alpha \leq 1, \\ C_D &= 1.06 + 1.14(M_\infty sin\alpha)^{-3} & M_\infty sin\alpha \geq 1. \end{aligned}$$

The jet trajectory can be obtained by integrating equation (3.15) for from $\pi/2$ to 0. Schetz & Billig [4] further assume that $\rho$ does not change along the jet, i.e. $\rho \equiv \rho_j$. Finally, the trajectory derived from equation (3.15) is applied after the Mach disk, before which the jet is assumed to be a vertical straight line. Schetz & Billig [4]'s method is applied to low speed jets in crossflow and compared with the experiments of Abramovich *et al.* [69]. The agreement is good for the case with $J = 4.75$, while relatively big discrepancy is observed when $J = 16.35$. In the present study, we apply equation (3.15) after the intersection of the center streamline and windward barrel shock, owing to the observation that the center streamline does not pass through the Mach disk, and the jet bends from the vertical direction rapidly only after this intersection. The dash-dot-dot curve in figure 3.27 ($b$) shows the prediction of the jet trajectory of case $A3$ by Schetz & Billig [4] 's theory, which under-predicts the jet penetration. However, the assumption of $\rho \equiv \rho_j$ along the jet maybe good enough for low speed jets in crossflow, it is not true for high speed transverse jets (dashed line in figure 3.27 ($b$)). Therefore, the density variation along the jet must be taken into account. We define an effective density ratio: $(\rho/\rho_j)^{eff} = \rho_f/\rho_b$. Here, $\rho_b$ is the density of the jet immediately behind the barrel shock, which is the effective jet exit where the jet actually sees the crossflow; and $\rho_f$ is the average density far downstream of the jet. The jet density variation in figure 3.27 shows that $\rho_b \approx 1.6$ and $\rho_f \approx 0.8$, which results in $(\rho/\rho_j)^{eff} \approx 0.5$. Using this effective density ratio, equation (3.15) predicts the trajectory marked by dash-dotted curve in figure 3.27 ($b$), which is much closer to the simulation result. Further we notice that after interaction with the barrel shock, the center streamline turns suddenly by approximately 10° (top right sub-figure in figure 3.27 ($b$)). Therefore, equation (3.15) should be integrated from 80° instead of 90°. This yields the long-dashed curve in figure 3.27 ($b$), which shows very good agreement with the current LES result, especially in the near field. We apply the same methodology to the supersonic injection (case $B2$), and the predicted trajectory by the proposed modification to Schetz's method is shown in figure 3.28 ($a$). In this case, $\rho_b \approx 3.6$ and $\rho_f \approx 1$, which results in $(\rho/\rho_j)^{eff} \approx 0.2778$; and the integration of equation (3.15) starts from 90° based on the observation that the streamline turns negligible angle after the barrel shock, which turns back when entering the second jet cell. The agreement is very good up to $x/D = 6$. It is encouraging that the modified Schetz's analysis can accurately predict the trajectory of transverse jet in the near field, though it is based on a number of assumptions [4]. Note that, Schetz & Billig [4]'s method may not be applicable to the far field, because it does not account for the effect of interactions between flow structures.

Figure 3.28 (*b*) compares jet trajectory from the simulation case $B2$ with the experimental results of Papamoschou & Hubbard [23], where the momentum ratio is 8.9 and close to the current simulations. Both the crossflow and the jet have very different flow condition as in the current simulation, but the trajectories are close to each other, which indicates again that the jet-to-crossflow momentum ratio $J$ is the dominant parameter that determines the jet penetration. In Papamoschou & Hubbar [23]'s work, they studied the effect of crossflow Mach number, and found that increasing the crossflow Mach number produces a slight increase in the jet penetration. They attribute this to the decrease of drag coefficient with the increase of crossflow Mach number (Schetz & Billig [4]). However, it may also be because that the turning of the crossflow due to the 3-dimensional bow shock increases with crossflow Mach number in moderate range. For example, figure 7 in Gènin & Menon [26]'s work shows obvious increase of crossflow upturning across the bow shock when the crossflow Mach number increases from 1.6 to 2.0. This increased turning gives the crossflow more vertical velocity component which is favorable to the penetration of the transverse jets. The conjecture is that the same jet would penetrate more in a supersonic crossflow than the subsonic crossflow. Therefore, it is reasonable to see that the jet trajectory in the current simulation is lower than those from Papamoschou & Hubbard [23]'s experiments.

The trajectories in the far field of Mach 3.7 supersonic injection has also been studied by Beresh *et al.* [3], where they defined the jet trajectories using the maximum loci of streamwise velocity deficit and vertical velocity, which are shown as the symbols $\Box$ and $\Diamond$ respectively in figure 3.29. The curves therein correspond trajectories calculated from the current simulation. It is shown that the trajectory defined by the loci of the maximum streamwise velocity deficit is higher than that defined by the loci of maximum vertical velocity, while both definitions yield lower jet trajectories than the definition based on the center streamline. The agreement between the current simulation and the experiment is very good for both definitions of trajectories used in Beresh *et al.* [3], which is actually foreseeable from the good agreement in the velocity profiles shown figure 3.9.

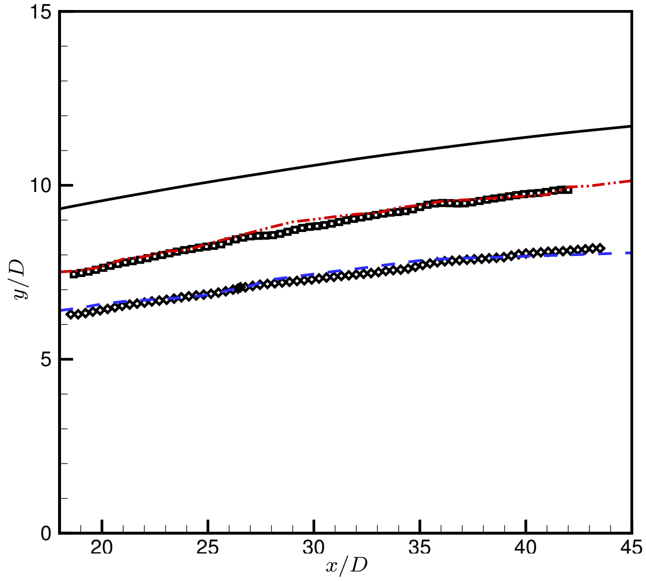

Figure 3.29: Trajectories of supersonic transverse jet by different definitions: solid – center streamline; dash-dot-dot – maximum loci of streamwise velocity deficit; dashed – maximum loci of vertical velocity. Symbols are experimental data from Beresh *et al.* [3].

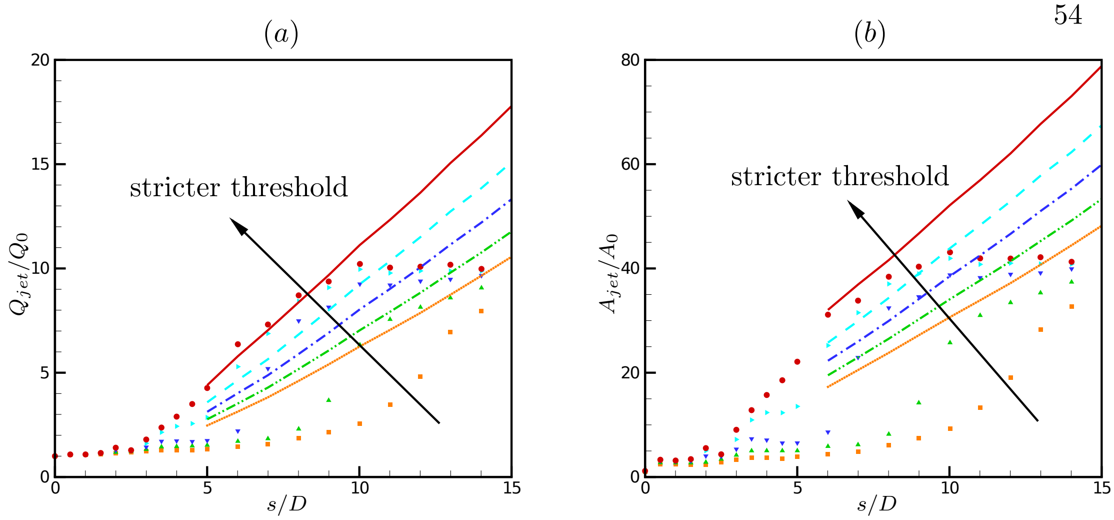

Figure 3.30: $(a)$ Entrainment plotted as a function of $s$ for various values of thresholds. $(b)$ Jet cross-sectional area along the length of the jet for different values of thresholds. Symbols denote criterion by axial velocity: ■, $\alpha = 0.1$; ▲, $\alpha = 0.05$; ▲, $\alpha = 0.02$; ►, $\alpha = 0.01$; ●, $\alpha = 0.005$. Lines denote turbulence kinetic energy criterion: dotted – $\beta = 0.02$; dash-dot-dot – $\beta = 0.01$; dash-dotted – $\beta = 0.005$; dashed – $\beta = 0.0025$; solid – $\beta = 0.001$.

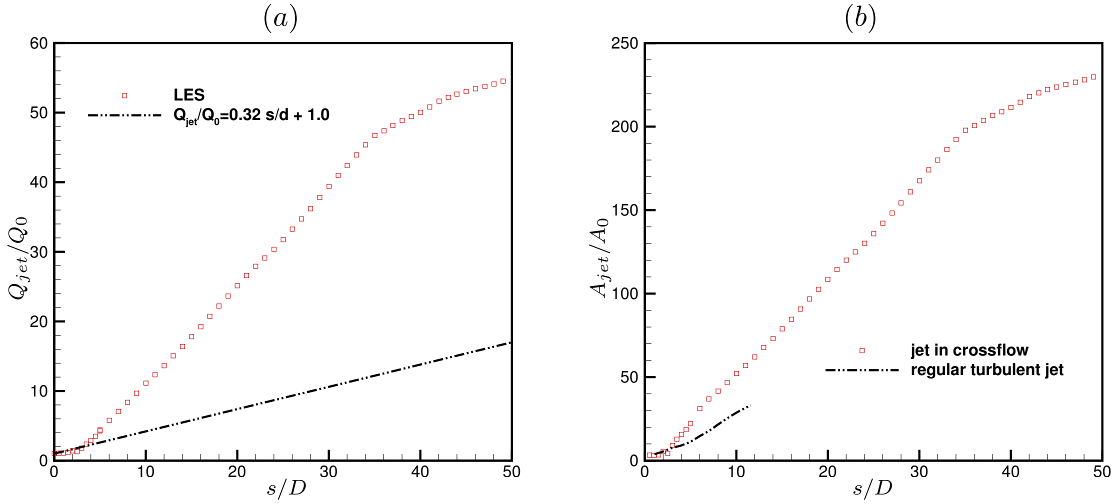

Figure 3.31: Entrainment of supersonic jet injected into subsonic crossflow: $(a)$ Jet mass flux along the length of the jet. $(b)$ Jet area variation along jet length. The dash-dot-dot curve is the jet area variation for a regular turbulent jet from the work of Babu & Mahesh [70]

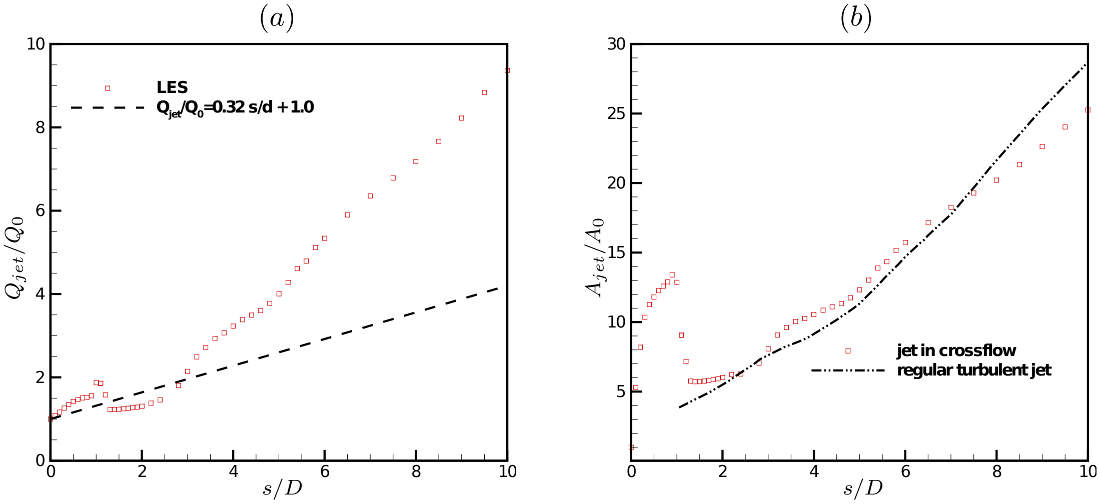

Figure 3.32: Entrainment of sonic jet injected into supersonic crossflow: (*a*) Jet mass flux along the length of the jet. (*b*) Jet area variation along jet length. The dash-dot-dot curve is the jet area variation for a regular turbulent jet from the work of Babu & Mahesh [70]

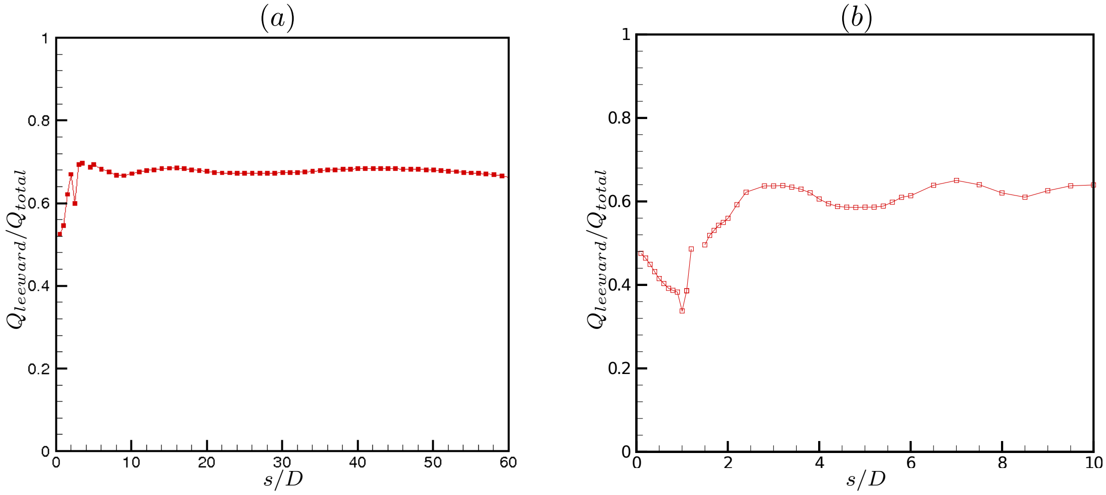

Figure 3.33: Percentage contribution of the leeward side of the jet to the total entrainment, plotted as a function of the jet length. a) supersonic injection; b) sonic injection.

## 3.7 Entrainment

The entrainment of the crossflow fluid by the jet can be estimated by calculating the jet mass flux across the trajectory-normal planes, i.e.

$$Q_{jet} = \int_{A_{jet}} (\rho u_s)\, dA, \tag{3.16}$$

where $Q_{jet}$ denotes the jet mass flux, $A_{jet}$ is the area of jet cross section that is normal to local jet trajectory, $u_s$ is the jet axial velocity. It is necessary to distinguish between the jet fluid and crossflow fluid, so that $A_{jet}$ can be determined as

$$A_{jet} = \{\sum_i \mathcal{A}_i \mid \mathcal{A}_i \in A_s, Criterion\}. \tag{3.17}$$

Here $A_s$ is the plane normal to the jet trajectory, and $\mathcal{A}_i$ is a facet on $A_s$ that satisfies the criterion. Because the passive scalar equation is not included in the current simulations, other criteria must be established to define the jet boundary. Here, we suggest use the jet axial velocity as a criterion in the near field, and use the turbulent kinetic energy in the far field. This choice of criteria is based on the observation that there is large jet axial velocity difference between the jet and freestream in the near field (e.g. figure 3.21) and large turbulent kinetic energy difference in the far field (e.g. figure 3.11 (*b*)) between the jet and the crossflow. Since turbulence enhances mixing, the value of turbulence kinetic energy somewhat indicates the level of mixing between the jet and the crossflow fluids, which also make it a reasonable criterion to separate the entrained and undisturbed crossflow.

At a specific trajectory-normal plane, the mathematical expression for the axial velocity criterion reads:

$$(u_s - U_\infty cos\,\theta) \geq \alpha\,(u_{s_{max}} - U_\infty cos\,\theta)\,, \tag{3.18}$$

where $u_{s_{max}}$ is the local maxium of $u_s$, $U_\infty$ is the free stream velocity, $\theta$ is the angle between $u_s$ and freestream ($x$) direction, and $\alpha$ is a threshold coefficient that adjust strictness of the criterion. The turbulent kinetic energy criterion for the far field takes the simple form of :

$$k \geq \beta k_{max}, \tag{3.19}$$

where $k = 0.5(\overline{u'^2} + \overline{v'^2} + \overline{w'^2})$ is the turbulent kinetic energy, $k_{max}$ is its maximum value on the trajectory-normal plane, and $\beta$ is the threshold coefficient similar to $\alpha$. Figure 3.30 shows the evolution of jet mass flux $Q_{jet}$ and cross-sectional area $A_{jet}$ along the center streamline calculated using different threshold for supersonic injection case $B2$. $\alpha$ varies from 0.1 to 0.005, while $\beta$ changes from 0.02 to 0.001. It is observed that decreasing the threshold value of $\alpha$ and $\beta$ results in increase of the calculated mass flux and $A_{jet}$. The curves based on the turbulent kinetic energy criterion do not appear to converge as the cutoff value of $k$ decreases. However, the 'curves' calculated from the axial velocity criterion do show certain trend of convergence as the decrease of the threshold axial velocity. First, it is reasonable that all the curves start from $Q_{jet}/Q_0 = 1.0$ at $s/D \approx 0.0$. Second, the curves for $\alpha = 0.01$ and $\alpha = 0.005$ stay close with each other even when $s/D$ is large. Furthermore, it is promising that the curves from the two proposed criteria, with $\alpha = 0.005$ and $\beta = 0.001$ respectively, collapse between $s/D = 5$ and $s/D = 10$, especially for the mass flux. Therefore, the proposed criteria are considered reasonable, and it is fair to choose $\alpha = 0.005$ and $\beta = 0.001$ as the threshold for the proposed two criteria, respectively. For sonic jet in supersonic crossflow, similar analysis shows that $\alpha = 0.05$ and $\beta = 0.01$ work the best.

Figure 3.31 ($a$) shows the entrainment of the supersonic jet injected into subsonic crossflow calculated from the the proposed method. Due to the observed similarity between this regime and the low speed jets in crossflow, the Ricou–Spalding correlation [71] for the volume flux of an incompressible regular jet, $Q_{jet}/Q_0 = 0.32s/D + 1.0$, is also plotted for comparison. Note that entrainment in the transverse jet is significantly larger than that in a turbulent free jet, as observed by Muppidi & Mahesh [66] for low speed jets in crossflow. At $s/D = 6$, the entrainment is about twice as much; and at $s/D = 10$, the entrainment is about three times as much. Moving to very far downstream, the entrainment rate starts decreasing after $s/D \approx 35$. The entrainment rate appears to settle at a magnitude that is comparable to the entrainment of a regular jet. This is reasonable, because the interaction between the jet and the crossflow becomes weaker and weaker as the jet bends into the freestream direction in the far field. It is also observed that close to the jet, $s/D < 4$, the entrainment of jet in crossflow is slightly smaller than free jet. This behavior is also observed in Muppidi & Mahesh [66]'s work, where passive scalar is used to calculate the jet entrainment. A small spikes in entrainment is observed at $s/D = 2$ whichever threshold values of $\alpha$ are used (figure 3.30($a$)). By comparing with figure 3.21, it is found that $x/D = 2$ corresponds the location where center streamline intersects with the barrel shock. This interaction causes the jet velocity decreases in magnitude. Equivalently, this yields a decreased threshold value due to equation (3.18), therefore more fluid will be counted as a part of jet, which causes increase in the calculated entrainment. Figure 3.31 ($b$) shows the jet area variation along jet length, where the data for turbulent free jet [70] is also plotted for comparison. Similar to jet entrainment, the area of the transverse jet grows faster than that of free jet, and the growth rate decreases after $s/D \approx 35$. In the very near field, a slightly slower grow rate than the regular jet is observed for $x/D < 3$; while a sudden increase in $A_{jet}$ is also observed at $s/D = 2$ and $s/D = 6$.

Figure 3.32 ($a$) shows the entrainment of sonic jet injected into supersonic crossflow. The Ricou–Spalding correlation is also plotted for comparison. Far from the jet exit $s/D > 3$, the entrainment of the sonic transverse jet behaves similarly to that of supersonic jet, and is significantly larger than that in a turbulent free jet. At $s/D \approx 1$, there is a spike on the curve, which again appears to be related with the incidence of the center streamline upon the barrel shock. Between $s/D \approx 1.25$ and $s/D \approx 3.0$, the entrainment of the transverse jet is slightly smaller than that of free jet. This may be associated with the curvature of the barrel shock and the reduced area of barrel shock cross-section near the barrel shock. The original jet mass flux reduces with this cross-sectional area due to the conservation of momentum, while the newly entrained mass flux can not compensate this reduction. Figure 3.32 ($b$) shows the jet area variation along the sonic jet length, where the data for turbulent free jet [70] is again plotted for comparison. A large difference is observed between figures 3.32 ($b$) and 3.31 ($b$). It shows that very near to the jet exit, the area of the jet increases very rapidly, because the under-expanded jet continues expanding as it exits the nozzle. The jet fluid is expelled outside of the periphery of the barrel shock due to the high pressure of the jet, which may interact with the crossflow intensely. The area then decreases as the jet interacts with the barrel shock, where the jet is under compression. It is interesting to note that far from the jet exit, the jet cross-sectional area increases similarly to that of incompressible free jet, and thus slower than that in the supersonic injection.

Figure 3.33 shows the percentage contribution of the leeward side of the jet to the

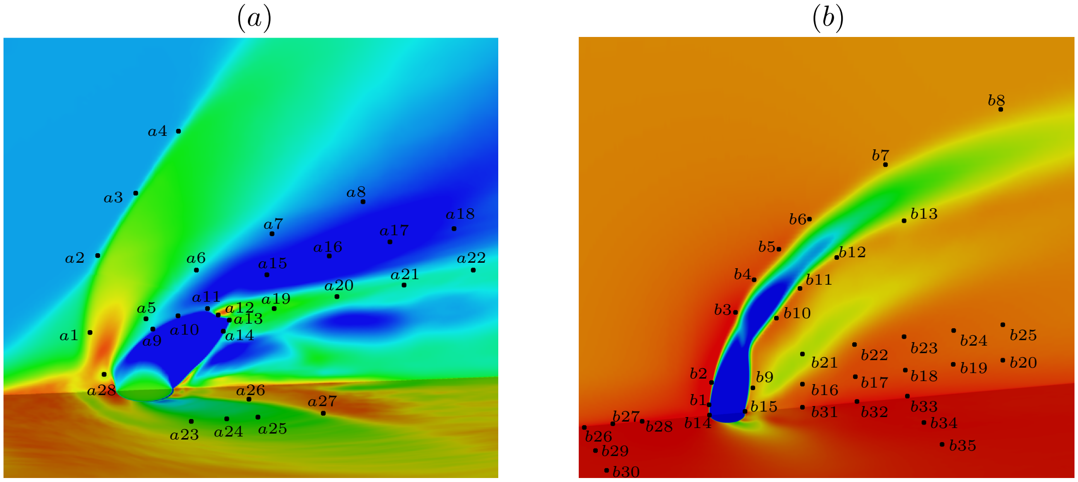

Figure 3.34: Locations and labels of flow probes: a) sonic injection; b) supersonic injection. The background contours show mean temperature on the center and horizontal near-wall planes.

total entrainment. Close to the jet, both the windward and the leeward sides of the jet contribute about the same to the total entrainment. In the far field, the leeward side of the jet consistently contribute more to the total entrainment. The ratio of the entrainment contributed by the leeward side of the jet to the total entrainment is around 60 % and 70% for sonic injection and supersonic injection, respectively. It indicates that the leeward side of the jet entrain almost twice as much as the windward side in the far field. At the jet near field, some oscillation is observed at $s/D = 2$ in figure 3.33 $(a)$, which is attributed to the interaction with the barrel shock. In sonic injection case, this ratio decreases first to less than 40 %, which then increases after $s/D \approx 1$. This indicates that in the jet near field, the windward shear layer vortices contribute the majority to the entrainment, until the CVP forms and grows. Figure 3.33 agrees with the work of Muppidi & Mahesh [66] qualitatively, and indicates the entrainment due to the jet windward shear layer is usually less than that due to the CVP on the leeward side of the jets.

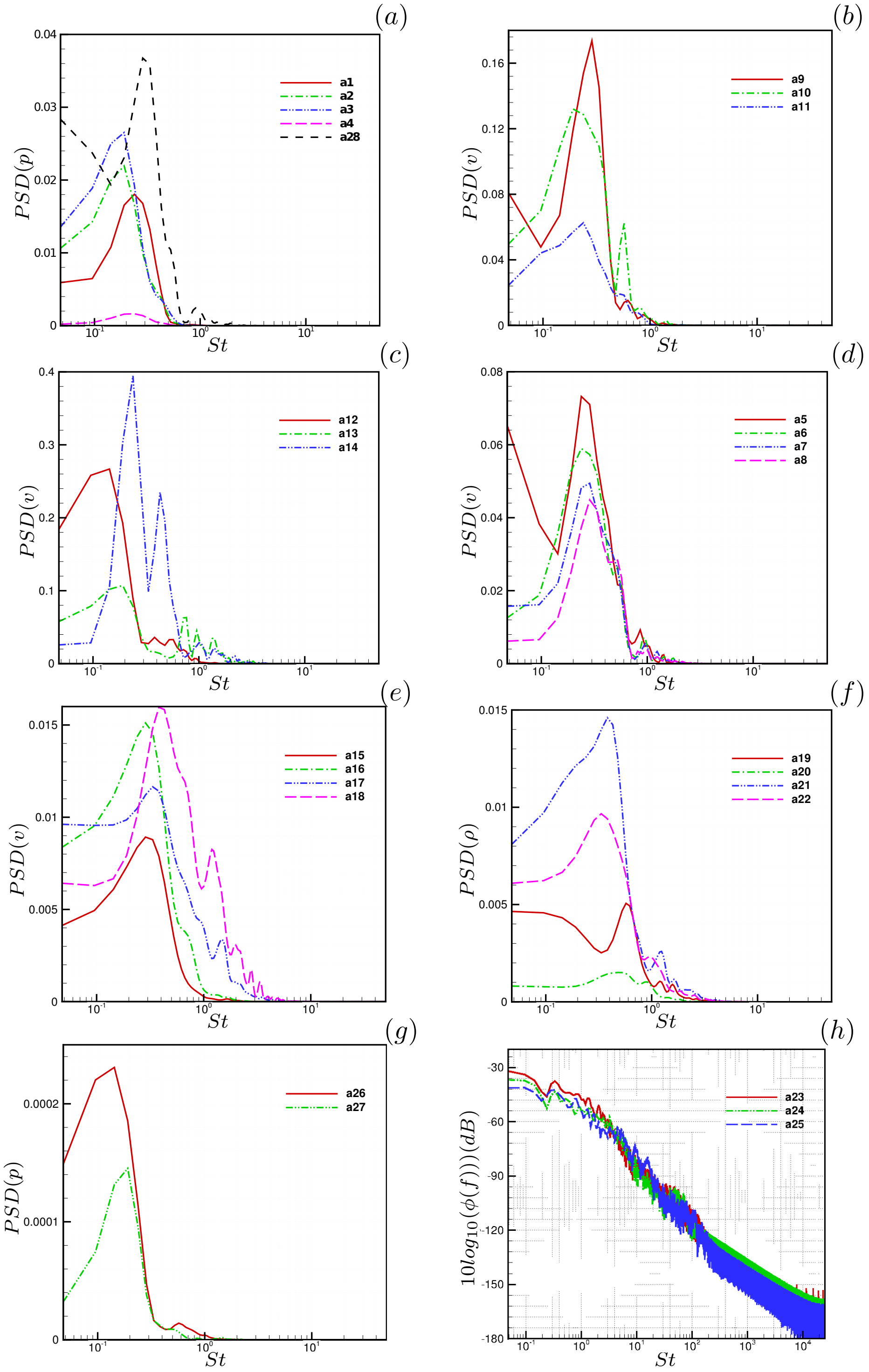

Figure 3.35: Power spectra densities of flow signals from different probes distributed in the flow field of sonic jet injected into supersonic crossflow (figure 3.34 $(a)$).

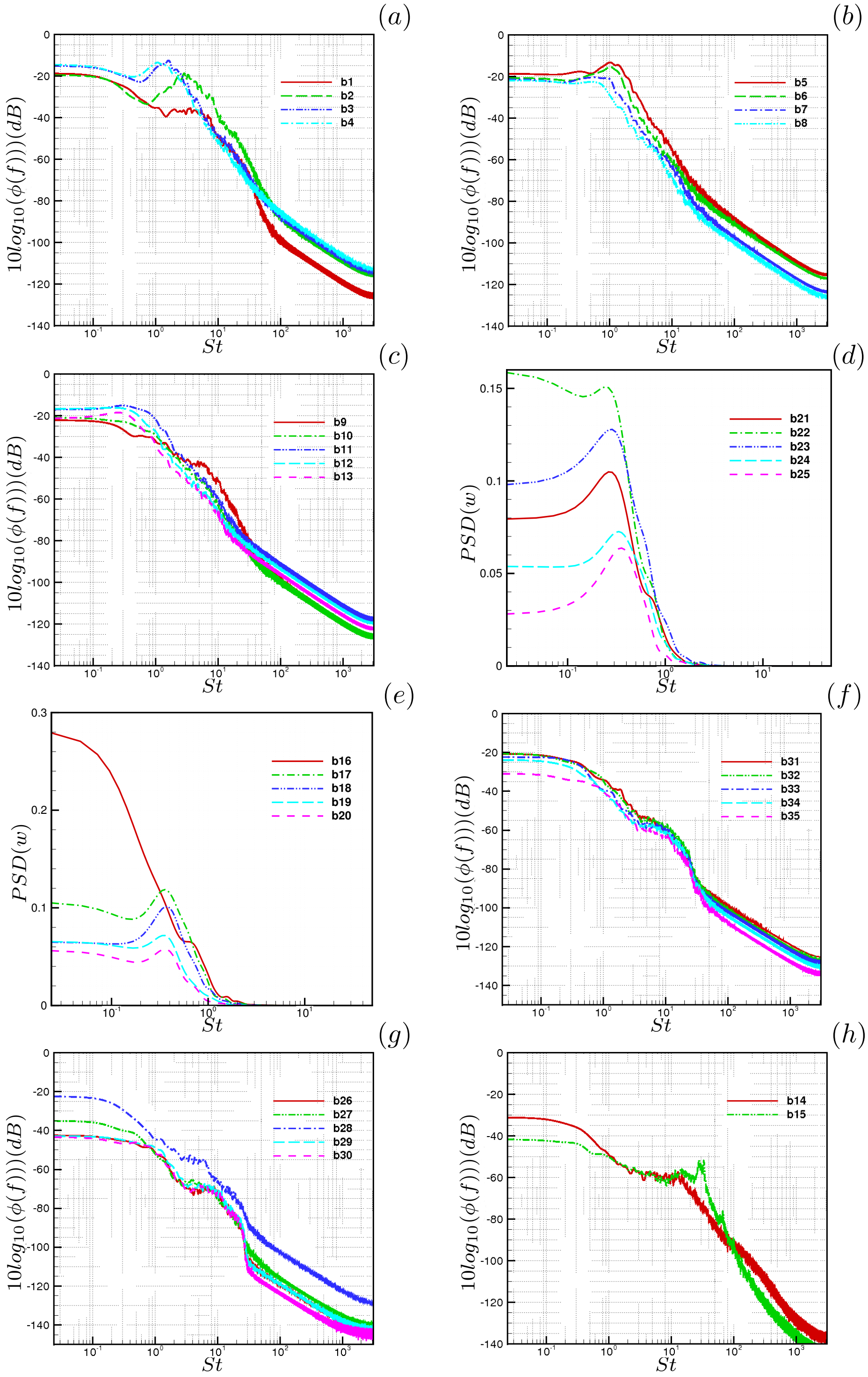

Figure 3.36: Power spectra densities of flow signals from different probes distributed in the flow field of supersonic jet injected into subsonic crossflow (figure 3.34 (*b*)).

## 3.8 Frequencies of important vortical structures

Probes are distributed over the flow field, where temporal signals of the primitive variables are collected at each time step and stored. The power spectral density (PSD) of these signals are then calculated and plotted as a function of Strouhal number defined based on the freestream velocity and jet diameter, i.e. $St = fD/U_\infty$. Here, $f$ is frequency. The frequencies (or $St$) at which the PSD peaks indicates the period of the dominant fluid motions at corresponding probe locations. Figures 3.34 (*a*) and (*b*) show the approximate locations of the selected flow probes in sonic injection and supersonic injection, respectively. Black dots denote the probes, which are labeled uniquely. Figures 3.35 and 3.36 show the PSD of the collected flow signals for sonic injection and supersonic injection, respectively. Note that only the PSDs of certain variables that show unambiguous peaks are chosen to be plotted, therefore the PSDs plotted in figures 3.35 and 3.36 might be for signals of different variables as pointed out through the labels of the ordinates in each figure.

Figure 3.35 shows the PSDs for sonic jet injected into a supersonic crossflow. The labels of the probes defined in figure 3.34 (*a*) are used as the legends in each sub-figures. From the animation of the flow field (not shown), it is observed that as the windward shear layer vorticies "shed", both the bow shock and barrel shocks deform and oscillate accordingly. Figure 3.35 (*a*), (*b*) and (*c*) show the PSDs of flow signals of probes aligning along the bow shock, windward barrel shock and leeward barrel shock (including Mach disk), respectively. The PSD curves show that the $St$ for the bow shock motion is between 0.2 and 0.25, which decreases slightly moving to the far field. The barrel shock (both windward and leeward) shows peak PSD at $St$ numbers that range from 0.2 to 0.3, but high frequency motions of the barrel shock can be observed in secondary peaks at high $St$. The probe around the Mach disk also show multiple slopes, with dominant low frequency motion of $St = 0.15$. Figure 3.35 (*d*) captures the dominant frequency of "shed" windward shear layer vortices. It is shown that, the dominant $St$ is between 0.25 and 0.3. The downstream probe shows slightly higher frequencies, because the flow accelerates there. The above $St$ numbers indicate that the deformation and oscillation of the bow shock and barrel shock are indeed related to the shedding event of the windward shear layer vortices. By comparing the pressure signal history and animation of flow field, Kawai & Lele [25] observed that the shedding of shear layer vortices is associated with the pressure change within the primary separation bubble in font of the jet. The dashed dark curve in figure 3.35 (*a*) shows the PSD of the pressure signal at $(-0.75d, 0.35d)$ in the primary separation bubble. It is shown that the dominant $St$ is very close to the numbers listed above, which supports Kawai & Lele [25]'s observation. Therefore, it appears that all the deformation and oscillation of the shock system and the shedding of the windward shear layer vortices are connected with unsteadiness of the primary separation bubble due to the interaction between the jet and the crossflow.

Figure 3.35 (*e*) shows the PSDs of signals from the upper inner shear layer defined in figure 3.12 of section 3.3. The dominant $St$ ranges from 0.3 to 0.4, and increases slightly as the flow evolves and accelerates. Figure 3.35 (*f*) shows the PSDs of signals from the lower inner shear layer, which shows higher dominant frequencies with $St$ ranges from 0.3 to 0.6. Near the jet, the dominant $St$ is 0.6. It appears to be related with the high frequency motions of the leeward barrel shock shown in figure 3.35 (*c*), where the secondary peak of the PSD of the signal from intersection of the leeward barrel shock and Mach disk has a $St$ of 0.7. Moving downstream, the frequencies keep decreasing. At the last location, the $St$ is 0.35, which is very close to the $St$ of the last probe in figure 3.35 (*e*). Figure 3.35 (*e*) and figure 3.35 (*f*) indicate that the upper and lower inner shear layer vortices collapse and interact as the jet evolves, resulting in a decreased $St$ in the lower inner shear layer and increased $St$ in the upper inner shear layer. Figure 3.35 (*g*) shows the dominant frequency at the boundary of the wake region, which is also featured sudden decrease of density gradient magnitude as shown in figure 3.12. This boundary is observed to be quasi-steady in the flow animation, and is shown to have a low $St$ of 0.15 in the near field and 0.2 further downstream. Figure 3.35 (*h*) shows the PSDs of the pressure signals from three different probes on the side of the jets, where is approximately on the way of the horseshoe vortices. All the PSD curves are very similar to each other, and there appears to be a small peak of PSD curves at $St \approx 0.35$. This is very closed to the frequency of the primary separation bubble. Probes are also placed between the wall and the lower inner shear layer downstream of the jet, where wake vortices locate if they exist. However, no specific dominant frequencies of fluid motions are observed, which confirms the former observation in section 3.3 that wake vortices do not prevail under this flow condition.

Figure 3.36 shows the PSDs of flow signals from supersonic jet injected into a subsonic crossflow. Similar notation in figure 3.35 is used. Figures 3.36 (*a*) and (*b*) attempt to resolve the frequencies of windward jet shear layer rollers. It is shown that the PSD curves peak at $St \approx 3.0$ in the jet near field, and $St \approx 1.5$ in the far field. As the jet evolves, the peaks become less and less obvious, indicating the decay and break-down of the jet shear layer. Figure 3.36 (*c*) shows the PSD curves of signals from the leeward side of jet shear layer. Changes in slopes are seen in these curves, but no unambiguous peaks can be observed. Figures 3.36 (*c*) and (*d*) show the $St$ of the upright wake vortices. It is oberved from these curves that the $St$ of the wake vortices is around 3.5. It is interesting to note that, at the first location in figure 3.36 (*e*) (solid curve), no peak can be found. However, at the first location in figure 3.36 (*d*) (solid curve), which has the same streamwise coordinate as the first location in 3.36 (*e*) but in a higher $y$ postion, has the obvious peak associated with the wake vortices. This is because (*i*) the wake vortices form at certain distance downstream of the jet, (*ii*) the wake vortices are inclined to the upwind ($-x$) direction (figure 3.16); therefore it is possible that when the wake vortices start to form, they can be seen at a higher location but are not discernible at a lower location with the same $x$ coordinate. Figures 3.36 (*f*) and (*g*) show the PSD curves of wall pressure signals from upstream and downstream of the jet, respectively. Changes in the slopes are observed between $St \approx 5 \backsim 10$. This may be related with the frequencies associated the boundary layer sweeping the wall. Close to the jet, increase in the overall PSD values is observed. Upstream of the jet, when the boundary layer is undisturbed, the PSD curves of signals from different spanwise locations collapse (figure 3.36 (*g*)). Downstream of the jet, the disturbed boundary layer appears to return faster to the original condition at spanwise locations than at the centerline (figure 3.36 (*g*)). Figure 3.36 (*h*) shows the PSD curves for pressure signals from the upstream and downstream edges of jet exits. Both locations are featured with high frequency changes in pressure field, with $St \approx 15$ at the upstream edge, and $St \approx 30$ at the downstream edge. These maybe related to the acoustic waves associated with jet expansion. It is interesting to note that the $St$ of the leeward edge is twice of that at the windward edge. Compared with figure 3.35, the flow motions in the supersonic injection have higher frequencies. Many motions in sonic injection case are correlated, with a driven force from the primary separation bubble; while the motions in supersonic crossflow do not show obvious correlations.

## 3.9 Summary

The physics of high speed jets in crossflow have been discussed based on the large-eddy simulations of two commonly used regimes: a sonic jet injected into a supersonic crossflow and a supersonic jet injected into a subsonic crossflow. The experimentally observed shock systems and vortical structures, such as the bow shock, separation shock, barrel shock, Mach disk, jet shear layer voritices, horseshoe vortices and the counter rotating vortex pair, have been successfully reproduced. It is found that the interaction of transverse jet with supersonic crossflow yields great differences than low-speed jet/crossflow interaction. The supersonic crossflow sees the jet as an obstacle and responds with the formation of a bow shock in front of the jet. The bow shock causes the separation of the crossflow boundary layer, as well as pressure increase downstream of the bow shock. This changes the wall pressure distribution and therefore the near wall flow field substantially. When the crossflow is subsonic, the interaction resembles the low-speed jets in crossflow, except that jet cells form within the jet plume if the jet is supersonic and not perfectly expanded. The jet cells cause the jet boundary to expand and contract alternately. The windward jet shear layer rolls up into vortices, which shed downstream periodically in sonic injection, but grow and travel along with the jet in supersonic injection. Downstream of the jet, two secondary shear layers form between the jet fluid that passes through the Mach disk, the jet fluid that passes through the barrel shock, and the ambient crossflow fluid. The secondary shear layers yield Kelvin-Helmholtz vortices downstream of the Mach disk. Such vortices do not exist for supersonic injection into subsonic crossflow or low-speed jets in crossflow. Clear upright wake vorticies are observed in supersonic injection but not in sonic injection. This is probably due to the low momentum ratio, so that the jet/crossflow interaction is different [65]. Because of the low penetration of sonic jet, the jet reorients and interacts with the wall early, which suppresses the formation of wake vortices. The time averaged flow fields are compared to the experimental results, and reasonable agreement is observed in both mean velocity and mean turbulent intensities. The effect of the crossflow flow boundary layer type is discussed, as well as the influence of grid resolution. It is interesting to find that the back pressure region due to the blockage of the transverse jet can extend downstream of the jet from the sides when the crossflow is supersonic, while it is entirely ahead of the jet center for subsonic crossflow/jet interaction. The trajectory and entrainment of transverse jet is studied. It is found that, when scaled with $JD$, the jet trajectories from different experiments and simulations show significant scatter. A Modification to Schetz & Billigs theory [4] is proposed, which yield good prediction of the jet trajectories for the current simulations in the near field. Along the jet center streamline, both the entrainment and jet cross-section grow faster than those for turbulent free jets. In the very far field, the growth rate of entrainment and jet cross-section decrease to values that are close to those for turbulent free jets. It is found that the jet leeward side flows contribute more to the total entrainment of the jet, indicating that the CVP is the primary entrainment mechanism instread of jet windward shear layer vortices. The Strouhal numbers of important flow structures are calculated using the power spectral density of the flow variables. Most motions in the sonic injection case are found to be correlated, and the primary separation bubble appears to be the source of these coherent motions. However in supersonic crossflow, the flow motions do not show obvious correlations. The frequencies of the flow structures in supersonic injection are observed to be higher that those in sonic injection.

# Chapter 4

# Dynamic $k$-equation model for the LES of compressible flows

This chapter presents a novel dynamic one equation eddy viscosity model for large-eddy simulation of compressible flows. The transport equation for sub-grid scale (SGS) kinetic energy is introduced to predict SGS kinetic energy. The exact SGS kinetic energy transport equation for compressible flows is derived formally. Each of the unclosed terms in the SGS kinetic energy equation is modeled separately and dynamically closed, instead of being grouped into production and dissipation terms, as in the Reynolds Averaged Navier-Stokes (RANS) equations. All of the SGS terms in the filtered total energy equation are found to reappear in the SGS kinetic energy equation. Therefore, these terms can be included in the total energy equation without adding extra computational cost. *A priori* tests using Direct Numerical Simulation (DNS) of decaying isotropic turbulence show that for Smagorinsky type eddy viscosity model, the correlation between SGS stress and the model is comparable to that from the original model. Also, the suggested model for pressure dilatation term in the SGS kinetic energy equation is found to have high correlation with its actual value. In *a posteriori* tests, the proposed dynamic k-equation model is applied to decaying isotropic turbulence and normal shock/isotropic turbulence interaction, and yields good agreement with available experimental and DNS data. Compared with the results of Dynamic Smagorinsky Model (DSM), the k-equation model predicts better energy spectra at high wave numbers, similar kinetic energy decay and fluctuations of thermodynamic quantities for decaying isotropic turbulence. For shock/turbulent interaction, k-equation model and DSM predict similar evolution of turbulent intensities across shocks, due to the dominant effect of linear interaction. The proposed k-equation model is more robust in that local averaging over neighboring control volumes (CV) is sufficient to regularize the dynamic procedure. The behavior of pressure dilation and dilatational dissipation is discussed through the budgets of SGS kinetic energy equation, and the importance of dilatational dissipation term is addressed.

## 4.1 Dynamic k-Equation Model

The key idea of the proposed dynamic k-equation model is to derive SGS kinetic energy (or the isotropic part of SGS stress, $\tau_{kk}$ in Eq. 2.22) by solving its transport equation, instead of using Yoshizawa's model (Eq. 2.24). It has been shown that Yoshizawa's model for SGS stress correlates very poorly with the results of direct numerical simulations of compressible isotropic turbulence [31], and under-predicts the magnitude of SGS kinetic energy [1]. On the other hand, the works of Deardorff [33], Schumann [34], Horiuti [41], Ghosal *et al.* [39] and Menon & Kim [40] show that using SGS kinetic energy equation yields better performance in LES of incompressible flows. Therefore, we extend this idea to compressible flows, and introduce the compressible SGS kinetic energy transport equation.

### 4.1.1 SGS Kinetic Energy Transport Equation

The SGS kinetic energy equation can be derived by subtracting the product of the Favre filtered velocity and the filtered momentum equation from the filtered product of velocity and momentum equation, i.e.,

$$\overline{[u_i \times (momentum\ equation)]} - \widetilde{u_i} \times \overline{(momentum\ equation)}.$$

After reduction and rearrangement (see Appendix A) of the above equation, the SGS kinetic energy equation can be obtained as

$$
\begin{aligned}
\frac{\partial \bar{\rho} k}{\partial t} \quad = \quad & -\frac{\partial \bar{\rho} k \tilde{u}_j}{\partial x_j} - \tau_{ij} \widetilde{S_{ij}} - 2\bar{\mu} \left[ \widetilde{S^*_{ij} S^*_{ij}} - \widetilde{S^*_{ij}} \widetilde{S^*_{ij}} \right] - \frac{\partial}{\partial x_j} \left[ \frac{5}{3} \left( \bar{\mu} \widetilde{u_j \frac{\partial u_k}{\partial x_k}} - \bar{\mu} \tilde{u}_j \frac{\partial \tilde{u}_k}{\partial \tilde{x}_k} \right) \right] \\
& + \frac{\partial}{\partial x_j} \left[ \tau_{ij} \tilde{u}_i + \bar{\mu} \frac{\partial k}{\partial x_j} + \bar{\mu} \frac{\partial}{\partial x_i} \left( \frac{\tau_{ij}}{\bar{\rho}} \right) + R q_j \right] - \frac{\partial}{\partial x_j} \left[ \frac{1}{2} \bar{\rho} \left( \widetilde{u_i u_i u_j} - \widetilde{u_i} \widetilde{u_i} \tilde{u}_j \right) \right] \ , \\
& + \left( \overline{p \frac{\partial u_k}{\partial x_k}} - \bar{p} \frac{\partial \tilde{u}_k}{\partial x_k} \right)
\end{aligned}
\tag{4.1}
$$

where $k$, $\tau_{ij}$, $q_j$ are SGS kinetic energy, SGS stress and SGS heat flux defined by equations (2.19), (2.15) and (2.16) respectively. $R$ is the specific gas constant with $R = C_p - C_v$. Eq. (4.1) is the exact form of the SGS kinetic energy equation. No additional assumption has been made beyond those in the derivation of the filtered Navier-Stokes equations. For convenience, the following notations are used:

$$
f_j = \frac{1}{2} \bar{\rho} \left( \widetilde{u_i u_i u_j} - \widetilde{u_i} \widetilde{u_i} \tilde{u}_j \right), \tag{4.2}
$$

$$
\epsilon_s = 2\bar{\mu} \left[ \widetilde{S^*_{ij} S^*_{ij}} - \widetilde{S^*_{ij}} \widetilde{S^*_{ij}} \right], \tag{4.3}
$$

$$
\epsilon_c = \frac{\partial}{\partial x_j} \left[ \frac{5}{3} \left( \bar{\mu} \widetilde{u_j \frac{\partial u_k}{\partial x_k}} - \bar{\mu} \tilde{u}_j \frac{\partial \tilde{u}_k}{\partial \tilde{x}_k} \right) \right], \tag{4.4}
$$

$$
\Pi = \overline{p \frac{\partial u_k}{\partial x_k}} - \bar{p} \frac{\partial \tilde{u}_k}{\partial x_k}. \tag{4.5}
$$

The SGS kinetic energy equation (4.1) reduces to

$$
\begin{aligned}
\frac{\partial \bar{\rho} k}{\partial t} \quad = \quad & -\frac{\partial \bar{\rho} k \tilde{u}_j}{\partial x_j} - \tau_{ij} \widetilde{S_{ij}} - \epsilon_s - \epsilon_c - \frac{\partial f_j}{\partial x_j} + \Pi \\
& + \frac{\partial}{\partial x_j} \left[ \tau_{ij} \tilde{u}_i + \bar{\mu} \frac{\partial k}{\partial x_j} + \bar{\mu} \frac{\partial}{\partial x_i} \left( \frac{\tau_{ij}}{\bar{\rho}} \right) + R q_j \right].
\end{aligned}
\tag{4.6}
$$

In Eq. (4.6), $-\frac{\partial \bar{\rho} k \tilde{u}_j}{\partial x_j}$ is the convection term; $-\tau_{ij} \widetilde{S_{ij}}$ is the production term, which is termed as SGS dissipation for the resolved kinetic energy [72] and represents the interscale energy transfer associated with the interaction of the resolved and unresolved scales; $-\epsilon_s$ is the solenoidal dissipation, $-\epsilon_c$ is the dilatational dissipation, $f_j$ is the triple correlation term, $\Pi$ is pressure dilatation, and the rest are diffusion terms. Note that the dilatational dissipation term is expanded to yield the approximation:

$$\epsilon_c \approx \frac{5}{3}\left[\bar{\mu}\widetilde{\left(\frac{\partial u_k}{\partial x_k}\right)^2} - \bar{\mu}\left(\frac{\partial \tilde{u}_k}{\partial x_k}\right)^2\right]. \tag{4.7}$$

In Eq. (4.6), the SGS stress $\tau_{ij}$ and SGS heat flux $q_j$ are modeled in the filtered Navier-Stokes equations (Eq. 2.1 and Eq. 2.11), and terms $\epsilon_s$, $\epsilon_c$, $f_j$ and $\Pi$ are to be modeled for the SGS kinetic energy equation.

Note that when the compressibility becomes negligible, $\epsilon_c$ and $\Pi$ approach zero, $Rq_j$ reduces to $\overline{u_j\frac{\partial p}{\partial x_j}} - \tilde{u}_j\overline{\frac{\partial p}{\partial x_j}}$, and $-\epsilon_s + \frac{\partial}{\partial x_j}\left[\bar{\mu}\frac{\partial}{\partial x_i}\left(\frac{\tau_{ij}}{\bar{\rho}}\right)\right]$ yields $-\bar{\mu}\left(\widetilde{\frac{\partial u_i}{\partial x_j}\frac{\partial u_i}{\partial x_j}} - \frac{\partial \tilde{u}_i}{\partial x_j}\frac{\partial \tilde{u}_i}{\partial x_j}\right)$. Consequently, in the incompressible limit, Eq. (4.1) reduces to

$$\begin{aligned}\frac{\partial \bar{\rho} k}{\partial t} &= -\frac{\partial \bar{\rho} k \tilde{u}_j}{\partial x_j} - \tau_{ij}\widetilde{S_{ij}} - \bar{\mu}\left(\widetilde{\frac{\partial u_i}{\partial x_j}\frac{\partial u_i}{\partial x_j}} - \frac{\partial \tilde{u}_i}{\partial x_j}\frac{\partial \tilde{u}_i}{\partial x_j}\right) - \left(\overline{u_j\frac{\partial p}{\partial x_j}} - \tilde{u}_j\overline{\frac{\partial p}{\partial x_j}}\right) \\ &\quad + \frac{\partial\left(\tau_{ij}\tilde{u}_i\right)}{\partial x_j} + \frac{\partial}{\partial x_j}\left[\bar{\mu}\frac{\partial k}{\partial x_j}\right] - \frac{\partial}{\partial x_j}\left[\frac{1}{2}\bar{\rho}\left(\widetilde{u_i u_i u_j} - \widetilde{u_i u_i}\tilde{u}_j\right)\right]\end{aligned}, \tag{4.8}$$

which is the SGS kinetic energy equation for incompressible flows [32, 34] after dividing by $\rho$ on both sides.

### 4.1.2 Residual Term H in the Filtered Total Energy Equation

In most of the LES modeling of compressible flows (e.g. Ref. [28], [73]), the residual term $H$ in the filtered energy equation (2.11) is neglected, partially because there are too many unclosed terms in $H$ adding to the complexity of modeling. However, for the proposed dynamic k-equation model we can take into account all of the terms in $H$ without adding extra computation and modeling cost. Recall the expression for $H$ (Eq. 2.18),

$$
\begin{aligned}
H \quad = \quad & -\frac{\partial}{\partial x_j}\left[\frac{1}{2}\left(\bar{\rho}\widetilde{u_i u_i u_j} - \bar{\rho}\widetilde{u_i u_i}\tilde{u_j}\right)\right] - \frac{\partial}{\partial x_j}\left[\frac{5}{3}\left(\bar{\mu}\widetilde{u_j\frac{\partial u_k}{\partial x_k}} - \bar{\mu}\tilde{u_j}\frac{\partial \tilde{u_k}}{\partial \tilde{x_k}}\right)\right] \\
& + \frac{\partial}{\partial x_j}\left[\bar{\mu}\frac{\partial k}{\partial x_j}\right] + \frac{\partial}{\partial x_j}\left[\bar{\mu}\frac{\partial}{\partial x_i}\left(\frac{\tau_{ij}}{\bar{\rho}}\right)\right]
\end{aligned}
.
$$

Compared with Eq (4.1), all the terms of $H$ reappear in the SGS kinetic energy transport equation. Therefore, the complete filtered total energy equation will be automatically closed once the SGS kinetic energy equation is modeled. Using the same notation as in the SGS kinetic energy equation (4.6), the filtered total energy equation can be re-written as

$$
\begin{aligned}
\frac{\partial}{\partial t}\left(\bar{\rho}\widetilde{E}\right) \quad = \quad & -\frac{\partial}{\partial x_j}\left(\bar{\rho}\widetilde{E}\widetilde{u_j} + \bar{p}\widetilde{u_j} - \widetilde{\sigma_{ij}}\widetilde{u_i} - \overline{Q_j} + C_p q_j\right) \\
& + \frac{\partial}{\partial x_j}\left[\tilde{\mu}\frac{\partial k}{\partial x_j}\right] + \frac{\partial}{\partial x_j}\left[\bar{\mu}\frac{\partial}{\partial x_i}\left(\frac{\tau_{ij}}{\bar{\rho}}\right)\right] - \frac{\partial f_j}{\partial x_j} - \epsilon_c .
\end{aligned}
\tag{4.9}
$$

### 4.1.3 SGS Modeling

Similar to the compressible DSM, eddy viscosity and eddy diffusivity models are used for the SGS tress $\tau_{ij}$ and the SGS heat flux $q_j$ respectively. However with the SGS kinetic energy equation, $\sqrt{k}$ is chosen as the velocity scale instead of $\Delta|\widetilde{S}|$, i.e.

$$
\tau_{ij} - \frac{2}{3}\bar{\rho}k\delta_{ij} \quad = \quad -2C_s\Delta\bar{\rho}\sqrt{k}\widetilde{S^*_{ij}}, \tag{4.10}
$$

$$
q_j \quad = \quad -\frac{\mu_t}{Pr_t}\frac{\partial \widetilde{T}}{\partial x_j} = -\frac{C_s\Delta\bar{\rho}\sqrt{k}}{Pr_t}\frac{\partial \widetilde{T}}{\partial x_j}. \tag{4.11}
$$

Here, $\mu_t = C_s\Delta\bar{\rho}\sqrt{k}$ is the eddy viscosity; $C_s$ and $Pr_t$ are the model coefficients to be determined dynamically by Germano identity. For convenience, we define 'eddy conductivity', $\kappa_t = C_p\frac{\mu_t}{Pr_t}$, which will be compared with thermal conductivity in the later section. The closure of energy equations requires models for $f_j$, $\epsilon_s$, $\epsilon_c$ and $\Pi$. We propose the following models for these terms:

$$\begin{aligned} f_j &= C_f \bar{\rho} \Delta \sqrt{k} \frac{\partial k}{\partial x_j}, && (4.12)\\ \epsilon_s &= C_{\epsilon s} \bar{\rho} k^{3/2} \Delta^{-1}, && (4.13)\\ \epsilon_c &= C_{\epsilon c} M_t^2 \bar{\rho} k^{3/2} \Delta^{-1}, && (4.14)\\ \Pi &= C_\Pi \Delta^2 \frac{\partial \bar{p}}{\partial x_j} \frac{\partial^2 \widetilde{u_k}}{\partial x_j \partial x_k}, && (4.15) \end{aligned}$$

where $C_f$, $C_{\epsilon s}$, $C_{\epsilon c}$, $C_\Pi$ are closure coefficients; $\Delta$ is the nominal filter width; $M_t = \frac{\sqrt{2k}}{a}$ is the SGS turbulent Mach number, where $a$ is the mean speed of sound. Models for $f_j$ and $\epsilon_s$ are adapted from the models of corresponding terms for incompressible RANS equations [42]. The model for dilatational dissipation term $\epsilon_c$ is taken from Sarkar *et al.* [74], and the model for pressure dilatational term $\Pi$ is based on series expansion. For any term that has the structure of $\overline{fg} - \bar{f}\bar{g}$, Bedford & Yeo [75] show that

$$\begin{aligned} \overline{fg} - \bar{f}\bar{g} &= 2\alpha \frac{\partial \bar{f}}{\partial x_k} \frac{\partial \bar{g}}{\partial x_k} + \frac{1}{2!} (2\alpha)^2 \frac{\partial^2 \bar{f}}{\partial x_k \partial x_l} \frac{\partial^2 \bar{g}}{\partial x_k \partial x_l} \\ &+ \frac{1}{3!} (2\alpha)^2 \frac{\partial^3 \bar{f}}{\partial x_k \partial x_l \partial x_m} \frac{\partial^2 \bar{g}}{\partial x_k \partial x_l \partial x_m} + ... \end{aligned} \qquad (4.16)$$

where

$$\alpha(y) = \int_{-\infty}^{\infty} x^2 G(x,y)\, dx \qquad (4.17)$$

and $G(x,y)$ is the kernel of the filter. For a box filter, $\alpha = \Delta^2/24$. In practice, $\alpha$ is approximated by $\alpha = C\Delta^2$, and $C$ is absorbed in the model coefficient $C_\Pi$.

Most of the model coefficients can be dynamically computed through Germano identity. However, since the model for solenoidal dissipation $\epsilon_s$ does not scale well across filters [76], the Germano identity for $\epsilon_s$ yields very small values of $C_{\epsilon s}$ which considerably under-predicts the magnitude of $\epsilon_s$ [1], causing incorrect evolution of SGS kinetic energy. Being modeled similarly, $\epsilon_c$ suffers from the same problem, and gives insufficient dissipation to SGS kinetic energy after the shock, which further affects the resolved quantities through the total energy equation (Section 4.4). To circumvent this problem, instead of using Germano identity, which assumes similarity of SGS stresses between the grid filter level and the test filter level, we use the analogy between the grid-filter-level

SGS stress and the Leonard stress $L$ across the test filter level, as used by Menon & Kim [40]. Specifically, as stated in section 2.3.2, in Germano identity, for any terms that are of form $a = \overline{\alpha\beta} - \bar{\alpha}\bar{\beta}$ and modeled as $a = C \cdot m$, it is assumed that on the test filter level $A = \widehat{\overline{\alpha\beta}} - \widehat{\bar{\alpha}}\widehat{\bar{\beta}} = C \cdot M$ holds; so that the model coefficient $C$ can be solved by equation:

$$L = \widehat{\bar{\alpha}\bar{\beta}} - \widehat{\bar{\alpha}}\widehat{\bar{\beta}} = C\left(M - \hat{m}\right),$$

where $L$ is the Leonard stress term. In contrast, Menon & Kim [40] assume that on the test filter level,

$$A = \widehat{\bar{\alpha}\bar{\beta}} - \widehat{\bar{\alpha}}\widehat{\bar{\beta}} = C \cdot M,$$

from which the model coefficient $C$ is directly solvable. Applying this methodology to $\epsilon_s$ and $\epsilon_c$, the resulting equations for $C_{\epsilon s}$ and $C_{\epsilon c}$ are

$$2\left[\widehat{\bar{\mu}\widetilde{S^*_{ij}}\widetilde{S^*_{ij}}} - \widehat{\bar{\mu}}\widehat{\widetilde{S^*_{ij}}}\widehat{\widetilde{S^*_{ij}}}\right] = C_{\epsilon s}\widehat{\bar{\rho}}K^{3/2}\widehat{\Delta}^{-1} \tag{4.18}$$

and

$$\frac{5}{3}\left[\widehat{\bar{\mu}\left(\frac{\partial\widetilde{u_k}}{\partial x_k}\right)^2} - \widehat{\bar{\mu}}\left(\frac{\partial\widehat{\widetilde{u_k}}}{\partial x_k}\right)^2\right] = 2C_{\epsilon c}\frac{\widehat{\bar{\rho}}^2}{\gamma\widehat{\bar{p}}}K^{5/2}\widehat{\Delta}^{-1}, \tag{4.19}$$

where $K$ is 'sub-test-filter scale' kinetic energy and of form

$$K = \widehat{k} + \frac{1}{2}\left(\widehat{\widetilde{u_i}\widetilde{u_i}} - \widehat{\widetilde{u_i}}\widehat{\widetilde{u_i}}\right).$$

Equations (4.18) and (4.19) yield reasonable values of $C_{\epsilon s}$ and $C_{\epsilon c}$, which appear to give correct decaying rate of SGS kinetic energy of temporal decaying isotropic turbulence and reasonable evolution of SGS kinetic energy across shocks. Note that this method is only applied to the determination of $C_{\epsilon s}$ and $C_{\epsilon c}$, and the Germano identity is used everywhere else.

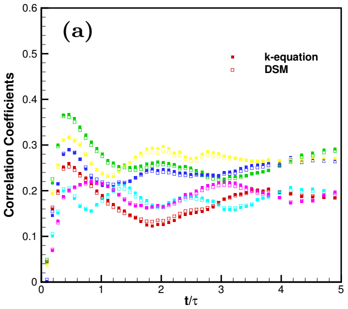

Figure 4.1: Correlation coefficients for SGS stresses $\tau_{ij}$: red – $\tau_{11}$, green – $\tau_{12}$, blue – $\tau_{13}$, cyan – $\tau_{22}$, yellow– $\tau_{23}$, pink – $\tau_{33}$; $(a)$ $M_t = 0.2$, $(b)$ $M_t = 0.4$, $(c)$ $M_t = 0.6$.

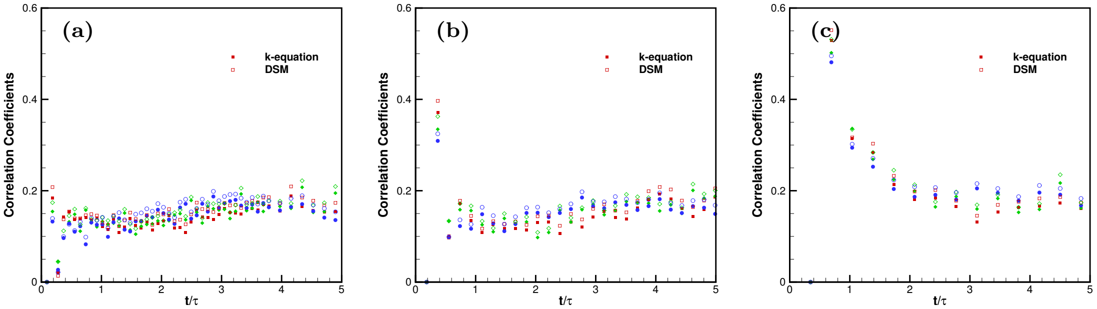

Figure 4.2: Correlation coefficients for SGS heat flux $q_j$: red – $q_1$, green – $q_2$, blue – $q_3$; $(a)$ $M_t = 0.2$, $(b)$ $M_t = 0.4$, $(c)$ $M_t = 0.6$.

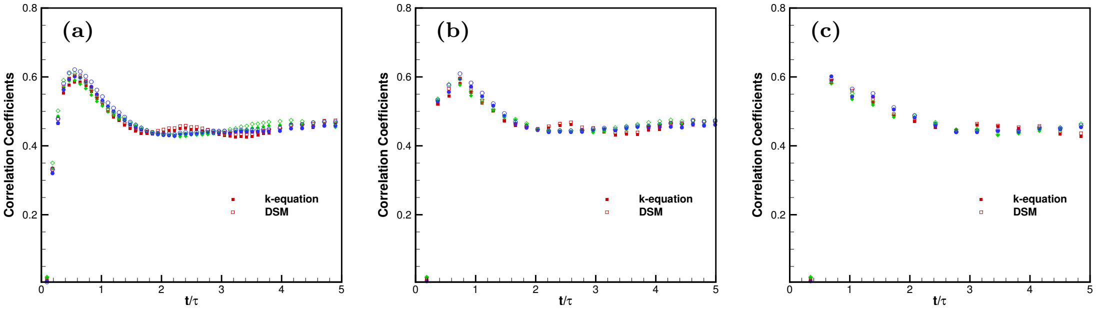

Figure 4.3: Correlation coefficients for $\dfrac{\partial \tau_{ij}}{\partial x_j}$: red – $\dfrac{\partial \tau_{1j}}{\partial x_j}$, green – $\dfrac{\partial \tau_{2j}}{\partial x_j}$, blue – $\dfrac{\partial \tau_{3j}}{\partial x_j}$; $(a)$ $M_t = 0.2$, $(b)$ $M_t = 0.4$, $(c)$ $M_t = 0.6$.

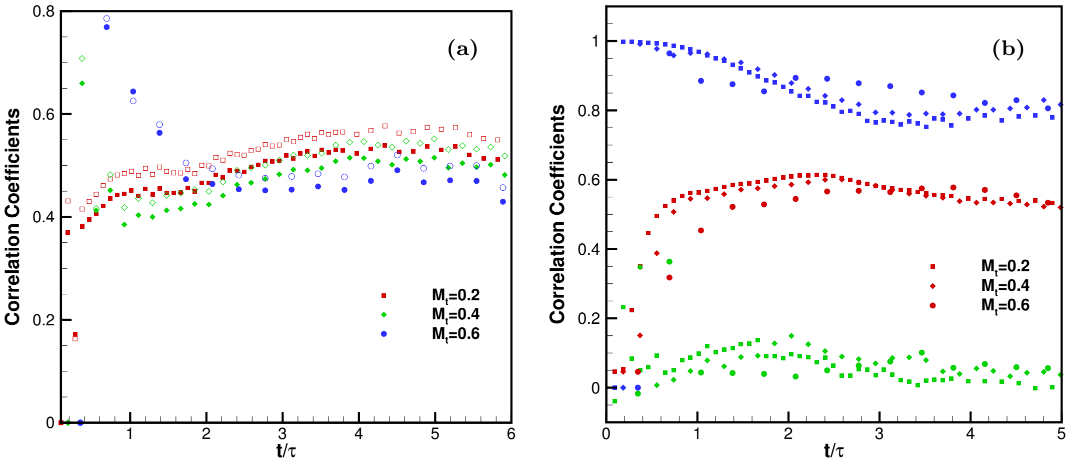

Figure 4.4: Correlation coefficients for: $(a)$ $\dfrac{\partial q_j}{\partial x_j}$, filled symbols – k-equation model, hollow symbols – DSM; $(b)$ red – $\epsilon_s$, green – $\epsilon_c$ and blue – $\Pi$.

## 4.2 *A Priori* Tests

This section presents *a priori* tests for the SGS models using DNS results of temporal decaying isotropic turbulence. The DNS employed a pseudo-spectral Fourier collocation scheme for spatial discretization and fourth-order Runge-Kutta method for time advancement. The skew-symmetric form of the convection terms is used to suppress aliasing errors. Details and validation of the numerical method are discussed b Ghosh & Mahesh [77]. The initial three dimensional energy spectrum is

$$E(k) = \frac{16}{3}\sqrt{\frac{\pi}{2}}\frac{M_t^2}{k_0}\left(\frac{k}{k_0}\right)^4 exp\left(-2k^2/k_0^2\right), \tag{4.20}$$

where $k_0 = 4$. This energy spectrum gives initial root mean square (RMS) velocity fluctuation of $u_{rms} = M_t/\sqrt{3}$, initial Taylor microscale of $\lambda_0 = 2/k_0$, and thus eddy turn-over time of $\tau = u_{rms}/\lambda_0 = 2\sqrt{3}/(k_0 M_t)$. Three cases are considered here, which have initial turbulent Mach numbers of $M_t = 0.2, 0.4, 0.6$ respectively. The initial Taylor micro-scale Reynolds number is set as $Re_\lambda = u_{rms}\lambda_0/\nu = 67.6$ for all cases. The simulations are performed on $2\pi^3$ cubical domain with $256^3$ control volumes. The grid resolution is doubled in each direction compared to corresponding simulations of Spyropoulos & Blaisdell [78] under similar flow conditions. The DNS data is filtered onto a $32^3$ grid, and correlation coefficients between the exact SGS terms and their modeled values are computed. Here, the box filter is used, since it has a positive definite kernel which allows positive SGS kinetic energy to be obtained [43]. Figure 4.1 and figure 4.2 show the correlation coefficients over time between the exact SGS stress components, SGS heat flux components and their models, respectively. DSM (Eq. 2.22 and Eq. 2.23, denoted by hollow symbols) and the k-equation model (Eq. 4.10 and Eq. 4.11, denoted by filled symbols) are compared as well. For all cases and all components of the SGS stress and SGS heat flux, DSM and the k-equation model yield very similar level of correlation, which is known to be low for the Smagorinski model. The shear stresses are observed to correlate better than normal stresses (Figure 4.1). Shown in figure 4.2, the correlation coefficients for SGS heat flux appear to be higher in highly compressible case ($M_t = 0.6$) than the other two cases ($M_t = 0.2$ and $M_t = 0.4$). Figure 4.3 and figure 4.4 (*a*) show the correlation coefficients for the divergence of SGS stress and that of SGS heat flux. These divergence terms are more important, because SGS stress and heat flux appear in the form of divergence in the momentum and energy equations. These figures show that the divergence of these modeled terms have better correlation than their components. Again, k-equation model and DSM give very similar correlation level in $\frac{\partial \tau_{ij}}{\partial x_j}$, while the correlation coefficients for $\frac{\partial q_j}{\partial x_j}$ in the k-equation model are a little smaller than, but still comparable to DSM. The correlations for $\epsilon_s$, $\epsilon_c$ and $\Pi$ are shown in figure 4.4 (*b*). It is encouraging that the proposed model for pressure dilatation $\Pi$ (Eq. 4.15) correlates very well with the actual values at all three turbulent Mach numbers. The model for $\epsilon_s$ also correlates reasonably well with its actual value, and the correlation coefficients are the second largest among all the SGS terms. For the dilatational dissipation $\epsilon_c$, the correlation coefficients are comparable to those for $\tau_{ij}$ and $q_j$. The correlation for triple product term is found to be the lowest (not shown). Among all the correlations, it also appears that only SGS heat flux related quantities (figure 4.2 and figure 4.4 (*a*)) show discernable Mach number dependence.

## 4.3 *A Posteriori* Tests

As noted in numerous studies (e.g. Ref. [79], [43]), *a priori* tests of SGS models are certainly of some value, but need careful interpretation. In order to draw conclusions about the performance of SGS models, *a posteriori* tests are performed in the next section.

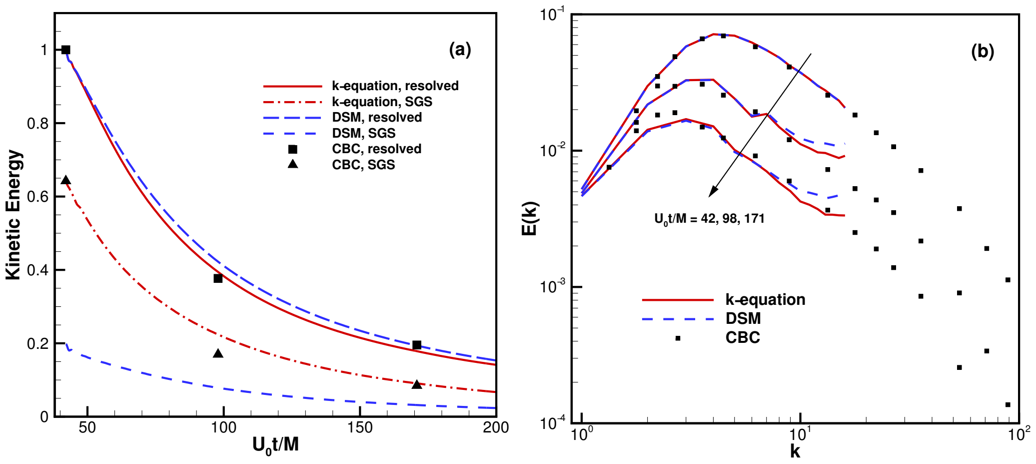

Figure 4.5: k-equation model for the CBC decaying isotropic turbulence on $32^3$ resolution.

The numerical base scheme is introduced in Chapter 2, where minimal numerical dissipation is emphasized. This makes the numerical scheme suitable for the implementation of SGS models in that almost all of the dissipations will come from the SGS models, so that the contribution/effect of SGS models can be ambiguously evaluated. Incorporated into the above numerical scheme, the proposed dynamic k–equation model is applied to decaying isotropic turbulence and normal shock/isotropic turbulence interaction.

### 4.3.1 Decaying Isotropic Turbulence

Two cases are considered here. One is a nearly incompressible simulation which is compared to the experiment of Comte-Bellot & Corrsin (CBC) [80], the other is compressible simulation where the filtered DNS results in section 4.2 are used for validation. Also compared are LES results using DSM. All Large-eddy Simulations are performed on a $32^3$ periodic cubical domain, and spatial averaging over homogeneous directions are applied during the dynamic procedures.

#### Quasi-incompressible simulation

The experiment of Comte-Bellot & Corrsin is simulated as temporally decaying isotropic turbulence through time–space correlation. The initial energy spectrum is obtained from

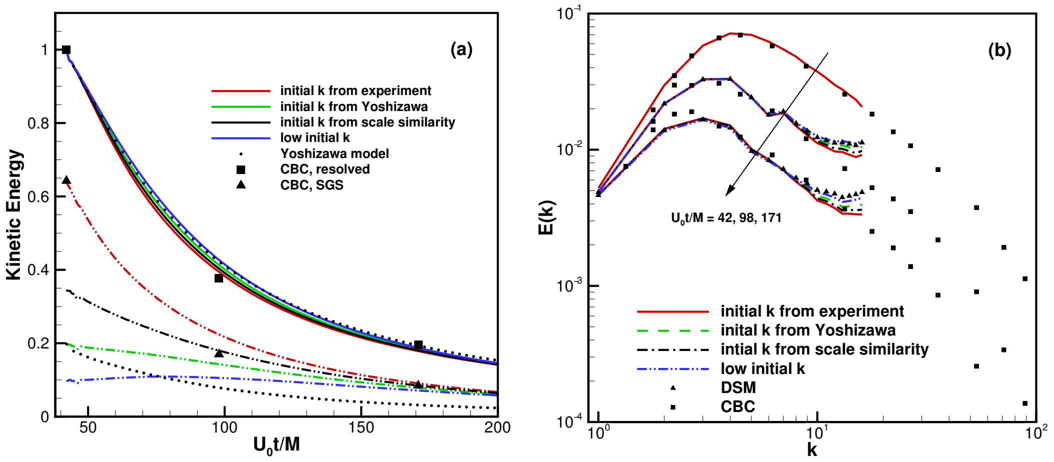

Figure 4.6: Effect of initial SGS kinetic energy. Solid curves: resolved kinetic energy; Non-solid curves: SGS kinetic energy.

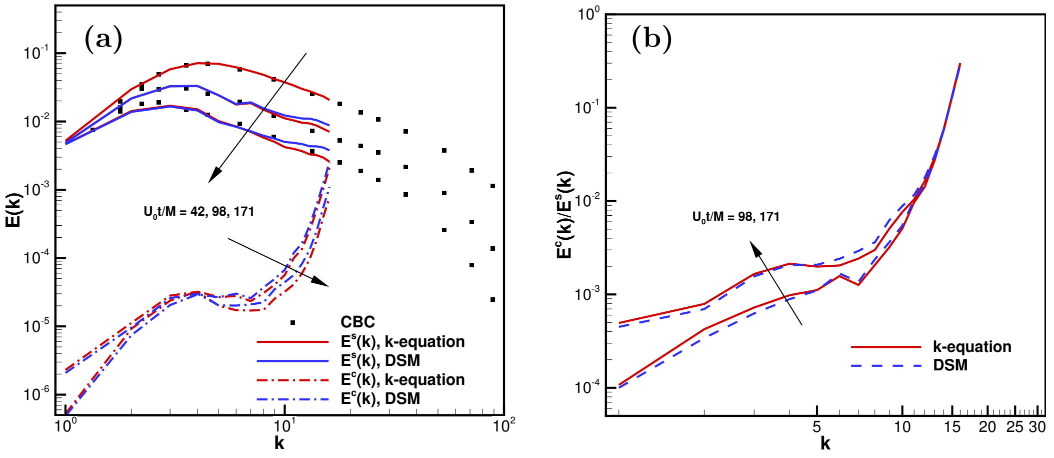

Figure 4.7: (*a*) Decomposition of 3D energy spectra; (*b*) Ratio of compressible energy spectra to solenoidal part. k is initialized with experimental condition in k-equation model.

the experiment at nondimensional time $U_0t/M = 42$. Initially, the velocity field is purely solenoidal, while the pressure field is computed from the incompressible Poisson equation. The density is assumed to be uniform, so the initial temperature field has similar spectrum as pressure due to the equation of state. SGS kinetic energy is initialized using Yoshizawa's model, however, its magnitude is scaled up so that the mean value of SGS kinetic energy matches the experimental SGS kinetic energy which can be estimated by integrating the energy spectrum over wave numbers that are higher than the cutoff wave number. Figure 4.5 (*a*) shows the temporal decay of kinetic energy, while figure 4.5 (*b*) shows the energy spectra at different time instants $U_0t/M = 42, 98, 171$ during the CBC experiment. DSM results under the same conditions are shown for comparison. As shown in figure 4.5 (*a*), the results from the dynamic k-equation model are very encouraging in that both decay of resolved kinetic energy and SGS kinetic energy agree well with the experiment. Yoshizawa's model used in DSM under-predicts the SGS kinetic energy. Figure 4.5 (*b*) shows that the energy spectra predicted by the k-equation model agree better with the experiments, and less energy is piled up at higher wave numbers compared with DSM results.

Figure 4.6 shows the effects of initial SGS kinetic energy. Figure 4.6 (*a*) shows that the initial decay rate of resolved kinetic energy is slightly smaller when a lower value of initial SGS kinetic energy is specified, since the eddy viscosity is proportional to $\sqrt{k}$ (Eq. 4.10). But this influence is small over a wide range of initial $k$, so that the k-equation model has the potential to yield reasonable prediction when the SGS kinetic energy is not accurate. Note that even with the very small magnitude of initial $k$ the proposed $k$-equation model gives comparable prediction of resolved energy decay with DSM. Also, the SGS kinetic energy always recovers to its "correct" value as flow evolves. From figure 4.6 (*b*), it seems that the effect of initial SGS kinetic energy only shows up at high wave numbers, where the energy cusp is smaller or comparable to the DSM results. Figure 4.6 also suggests that $\frac{1}{2}\left(\widehat{\widetilde{u_i}\widetilde{u_i}} - \widehat{\widetilde{u_i}}\widehat{\widetilde{u_i}}\right)$ (scale similarity) is a good estimation of initial SGS kinetic energy if the actual value is unknown.

Energy cusps are observed in the energy spectra shown in Figure 4.5 (*b*) and Figure 4.6 (*b*). Decomposing the energy spectra into compressible part $E^c(k)$ and solenoidal part $E^s(k)$ [81], as shown in Figure 4.7 (*a*), reveals that the energy cusps are mainly caused by the compressible part of energy. Because of periodic boundary conditions,

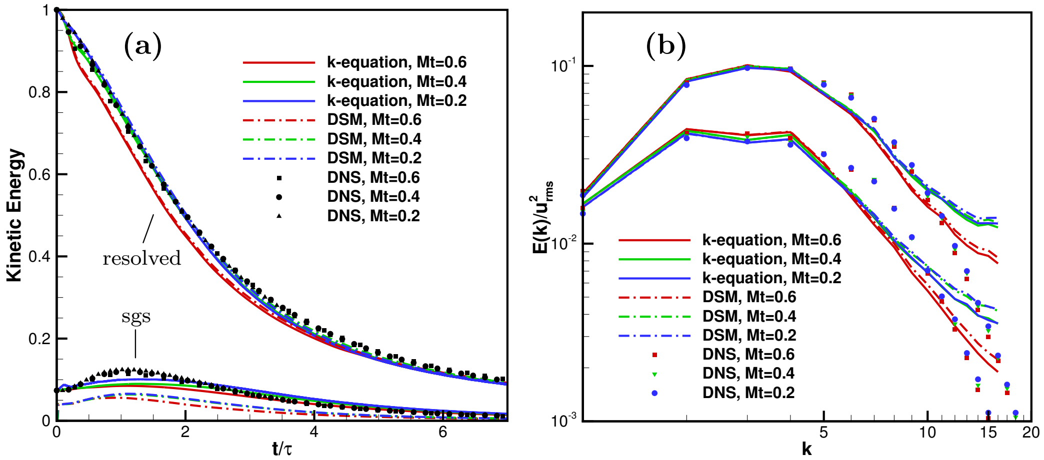

Figure 4.8: Initial energy spectrum from Eq. (4.20): (*a*) Time evolutions of kinetic energy; (*b*) energy spectra at two different instants: solid lines – $t/\tau = 2.217$, dash-dot lines – $t/\tau = 4.434$.

initial acoustic transients will never exit the computational domain, and will steepen up over time. Figure 4.7 (*b*) shows that at moderate length scales the solenoidal part of kinetic energy decays faster than the compressible part, and the ratio of $E^c(k)$ to $E^s(k)$ increases over time; however, the compressible kinetic energy accounts for only around 0.1% of the solenoidal energy. At high wave numbers, the ratio of $E^c(k)$ to $E^s(k)$ is up to 30%, and does not appear to change over time.

### Compressible simulations

The compressible LES have the same initial spectra ($\backsim k^4 e^{-k^2}$) as the *a priori* tests in section 4.2. Three turbulent Mach numbers of $M_t = 0.2,\ 0.4,\ 0.6$ are considered. The initial SGS kinetic energy is derived from the filtered DNS results. Figure 4.8 (*a*) compares the time evolution of kinetic energy with the filtered DNS results, and DSM results as well. In terms of resolved kinetic energy decay, good agreement can be observed between LES and filtered DNS for $M_t = 0.2$ and $M_t = 0.4$ cases. $M_t = 0.6$ case suffers from initial transient due to "inconsistent" initial condition [82], and is a little off from DNS results. Figure 4.8 (*b*) shows the energy spectra at time $t/\tau = 2.217$ and $t/\tau = 4.434$. Consistent with energy decay shown in figure 4.8 (*a*), the difference in

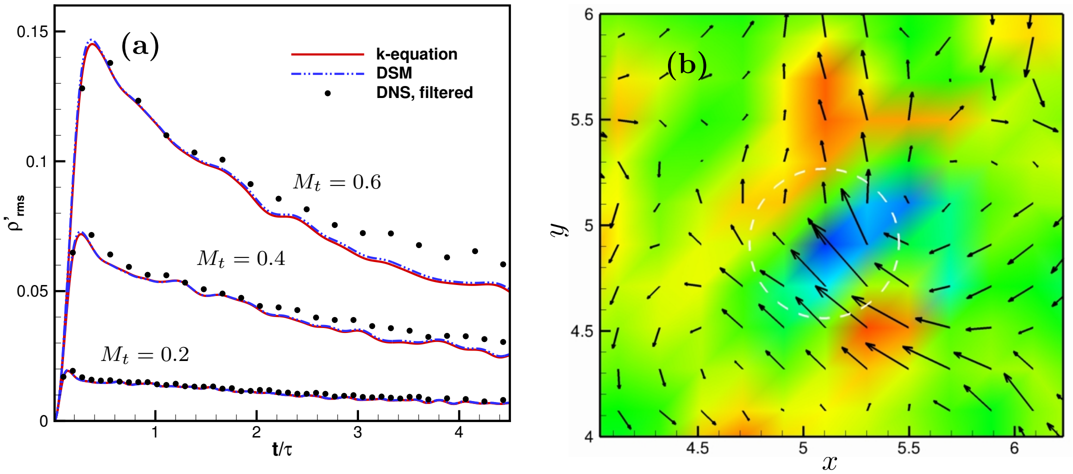

Figure 4.9: (*a*) Time evolutions of rms density fluctuations; (*b*) divergence contour superposed by in plane velocity vectors for case $M_t = 0.6$ at time $t/\tau = 1.0$.

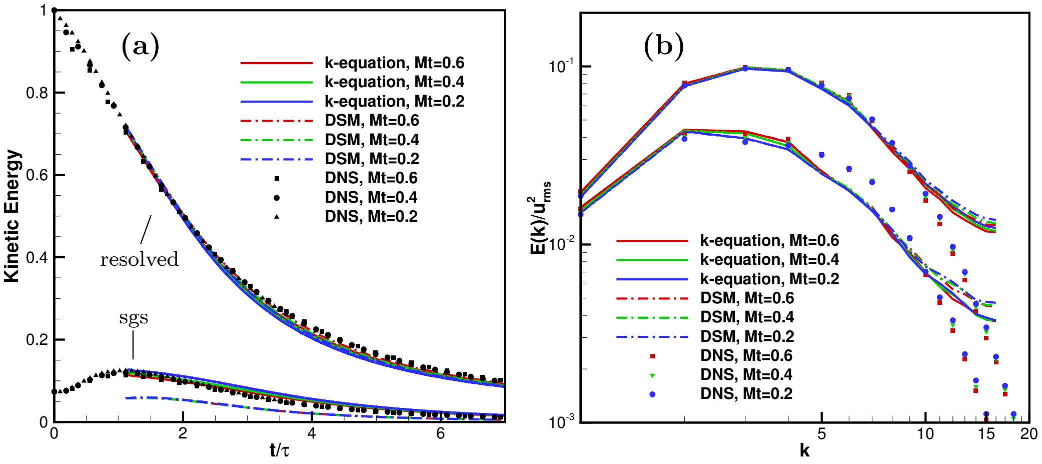

Figure 4.10: Initial condition from filtered DNS at $t/\tau \approx 1.1$: (*a*) Time evolutions of kinetic energy; (*b*) energy spectra at two different instants: solid lines – $t/\tau = 2.217$, dash-dot lines – $t/\tau = 4.434$.

energy spectra between cases $M_t = 0.2$ and $M_t = 0.4$ is very small, while case $M_t = 0.6$ differs from others due to initial transients, and the difference is mainly in high wave numbers. Compared with DSM results, the k-equation model yields similar decay of resolved kinetic energy. However, the SGS kinetic energy predicted by the proposed transport equation (Eq. 4.6) agrees with the DNS results much better than Yoshizawa's formula in DSM (figure 4.8 (*a*)). Consistent with the quasi-incompressible simulation (figure 4.5), the k-equation model predicted better energy spectra than DSM at high wave numbers, as observed in figure 4.8 (*b*). Given that DSM is known to perform well for decaying isotropic turbulence, the improvement of the proposed dynamic k-equation model is encouraging.

Figure 4.9 (*a*) compares the time evolution of the RMS density fluctuations with the filtered DNS results. Good agreement can be observed for simulations at all of the three Mach numbers. The simulation results using the k-equation model and DSM are very close. Figure 4.9 (*b*) shows the contours of velocity divergence on plane $z = 3.83$ for $M_t = 0.6$ at time $t/\tau = 1.0$, along with the in plane velocity vectors. In the region of peak negative divergence, marked by the white circle, a sudden decrease of normal velocity component is observed. At the upstream CV center, the Mach number is found to be $M_1 = 1.238$. From the Rankine–Hugoniot relation, the pressure jump ratio for this Mach number is estimated to be $p_2/p_1 = 1.62$. From the simulation, the pressure ratio is found to be $p_2/p_1 = 1.71$, which is very close to the Rankine–Hugoniot relation, considering the flow is not stationary. This ability of the proposed SGS model to model turbulence with highly compressible local regions is encouraging.

To access the effect of initial transients, LES was performed using the filtered DNS field at $t/\tau \approx 1.1$ as the initial condition. Figure 4.10 shows the kinetic energy decay and energy spectra. Shown in figure 4.10 (*a*), the decay of resolved kinetic energy in $M_t = 0.6$ is noticeably improved. Moreover, the SGS kinetic energy from k-equation model also achieves better agreement with the DNS, while Yoshizawa's formula in DSM continues under-predicting the SGS kinetic energy. In figure 4.10 (*b*), the energy spectra for $M_t = 0.6$ collapse with the other two cases after removal of initial transients. Compared with figure 4.8 (*b*), all spectra agree with the DNS better at medium wave numbers, especially at $t/\tau = 2.217$. The remaining difference between the LES and DNS at high wave numbers and medium wave numbers at $t/\tau = 4.434$ is likely to be related with the

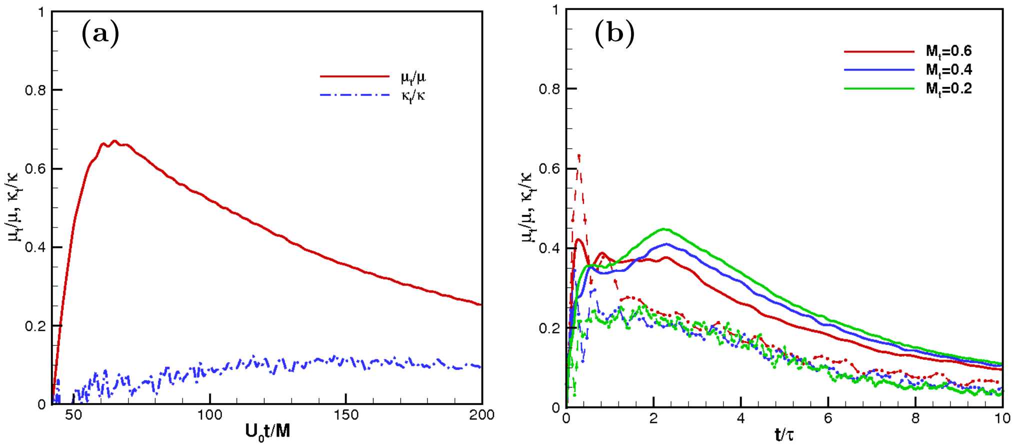

Figure 4.11: Eddy viscosity and conductivity for the decaying isotropic turbulence: (a) CBC; (b) compressible case, where solid lines are eddy viscosity, symbols on dashed lines are eddy conductivity, and different colors denote different inital $M_t$.

artificial initial $\backsim k^4 e^{-k^2}$ energy spectra, because good agreement in both kinetic energy decay and spectra is observed in incompressible simulations when physical initial energy spectra from CBC's experiment is used. Figure 4.10 also shows that the improvement from the k-equation model is consistent and independent from the initial conditions.

### Eddy viscosity and 'eddy conductivity'

Figures 4.11 (a) and (b) show the time evolution of eddy viscosity and 'eddy conductivity' for quasi-incompressible and fully compressible isotropic turbulence, respectively. For the quasi-incompressible case, the eddy viscosity contributes up to 70% of the molecular viscosity, and decreases as the turbulence decays. The eddy conductivity is approximately constant as the flow evolves, and its value is only around 10% of the thermal conductivity. For highly compressible cases, the maximum ratio of eddy viscosity to molecular viscosity is less than, but still comparable to, that in CBC isotropic turbulence; while the maximum ratio of eddy conductivity to the thermal conductivity is more than twice of that for the CBC case. Large initial transients in $\mu_t/\mu$ and $\kappa_t/\kappa$ are observed as the flows adapt to the initial conditions generated by the 3-D energy spectrum (Eq. 4.20). It also appears that the eddy viscosity decreases with $M_t$, while the eddy conductivity increases slightly with $M_t$.

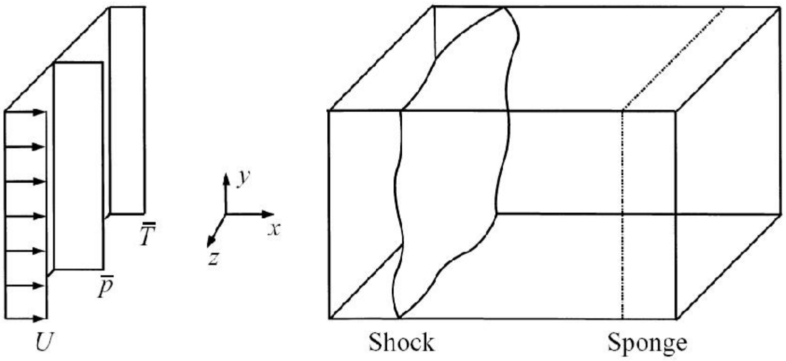

Figure 4.12: Schematic of shock/turbulence interaction problem.

### 4.3.2 Normal Shock/Isotropic Turbulence Interaction

Shock/turbulence interactions prevail in high speed turbulent flows. It is necessary for a good compressible SGS model to accurately predict the evolution of the turbulent flow across a normal shock wave. The schematic of the problem is shown in figure 4.12. Isotropic turbulence is introduced at the inflow, decays spatially over a short distance and then interacts with a statistically stationary normal shock. A sponge layer is used at the end of the computational domain to absorb reflected acoustic oscillations. Spatial averaging over homogeneous directions ($y - z$ planes) is applied during the dynamic procedures.

Two cases are considered. The first case has low $Re$ which corresponds to the DNS of Mahesh, Lele & Moin [83], where the inflow Mach number is $M = 1.29$, the turbulent Mach number of the inflow is $M_t = 0.14$, and the micro-scale Reynolds number is $Re_\lambda = 19.1$. The second case corresponds to the DNS of Larsson & Lele [84], which has higher $Re$, freestream Mach number $M$ and turbulent Mach number $M_t$ ($M = 1.5$, $M_t = 0.221$, $Re_\lambda = 40.0$). The two simulations are carried out on the same computation domain with exactly the same mesh. The domain has the dimension of $L_x = 10$ in streamwise direction, $L_y = L_z = 2\pi$ in the transverse directions. The mesh has $180 \times 32^2$ CVs, which is uniform in the transverse directions and clustered in the vicinity of the shock in streamwise direction.

The inflow isotropic turbulence is generated using a similar method to Mahesh *et al.*s [83]'s isotropic turbulence, which has the initial energy spectrum of Eq. (4.20)

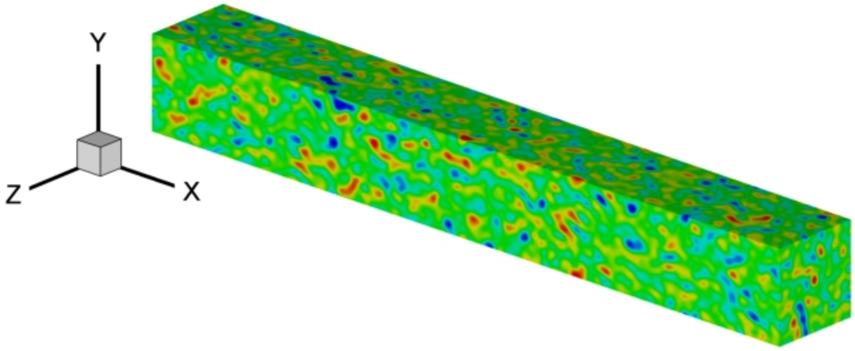

Figure 4.13: Decaying isotropic turbulence in long periodic box.

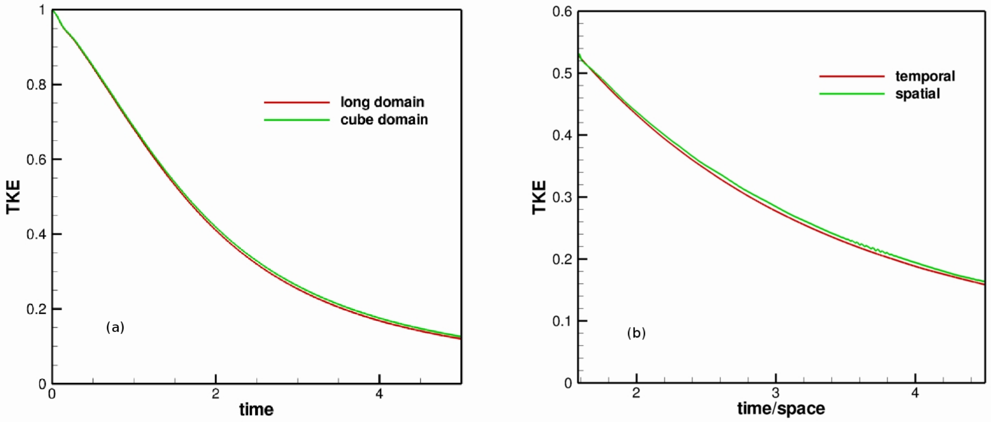

Figure 4.14: Validation of inflow turbulence generation and implementation.

and is allowed to decay temporally until the designated $M_t$ and $Re_\lambda$ are reached. Then, an instantaneous realization of the flow field is taken and used as the inflow of shock/turbulence interaction problem using Taylor's hypothesis. Simulation of isotropic turbulence is performed on a uniformly meshed long periodic box which has the dimension of $n\pi \times 2\pi \times 2\pi$ (figure 4.13). $n$ is chosen big enough to generate an inflow data sequence that is long enough to provide unduplicated isotropic inflow turbulence for several flow-through times, so that converged statistics can be achieved. For the current case, $n$ is chosen as 16, which will provide around 5 flow-through time of inflow data and is proven to be enough for the statistics to converge. This methodology is validated by temporally and spatially decaying isotropic turbulence as shown in figure 4.14, where figure 4.14 (*a*) compares the temporal decay of kinetic energy for isotropic turbulence in a periodic cube and a long periodic box, starting with the same energy spectrum. Figure 4.14 (*b*) compares the energy decay rate of temporally decaying isotropic turbulence and the spatially decaying turbulence where the inflow isotropic turbulence is extracted from the temporal case at time $t/\tau = 1.58$. Good agreement is observed for both cases. Then, the isotropic turbulent inflow is allowed to convect into the computational domain of shock/turbulence interaction.

### Instantaneous field

Figure 4.15 shows instantaneous density contours on the central plane $z = 0$. The overlaid contour lines are isopressure lines which shows the shock wave. The upstream turbulence causes the shock front to distort in the transverse ($y$ and $z$) directions. The distortion is found to be stronger at the high $Re$ and high $M_t$ case where the shock front also breaks occasionally. Downstream of the shock, more small scale flow structures can also be observed for the high $Re$ case.

### Turbulent intensities

Figure 4.16 compares the distribution of averaged turbulent intensities calculated from the k-equation model with the DNS [83] and DSM results. In figure 4.16 (*a*) and (*b*), the turbulent intensities are normalized by the their values immediately upstream of the shock, to compare to the DNS. Good agreement is observed between the k-equation model and DNS results. Note that the turbulent intensities are very high in the

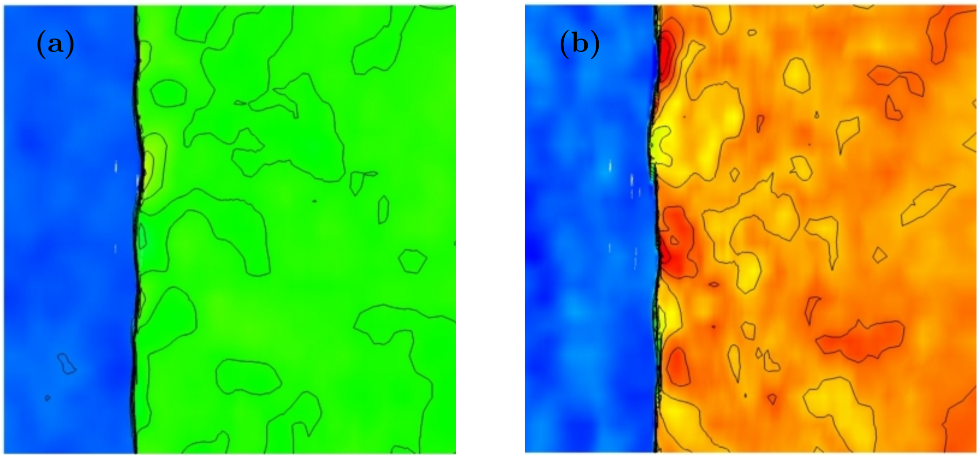

Figure 4.15: Instantaneous density fields superposed by isopressure lines on central plane: (a) low $Re$; (b) high $Re$.

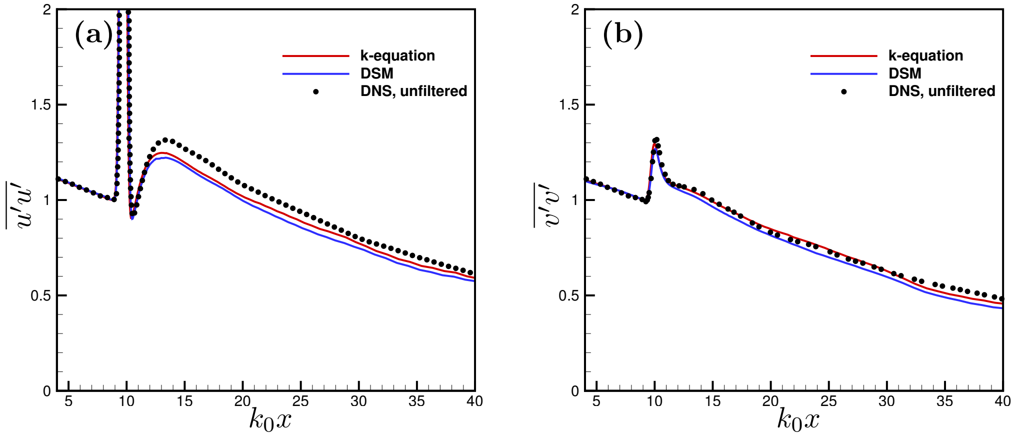

Figure 4.16: Distribution of averaged turbulent intensities for low $Re$ case.

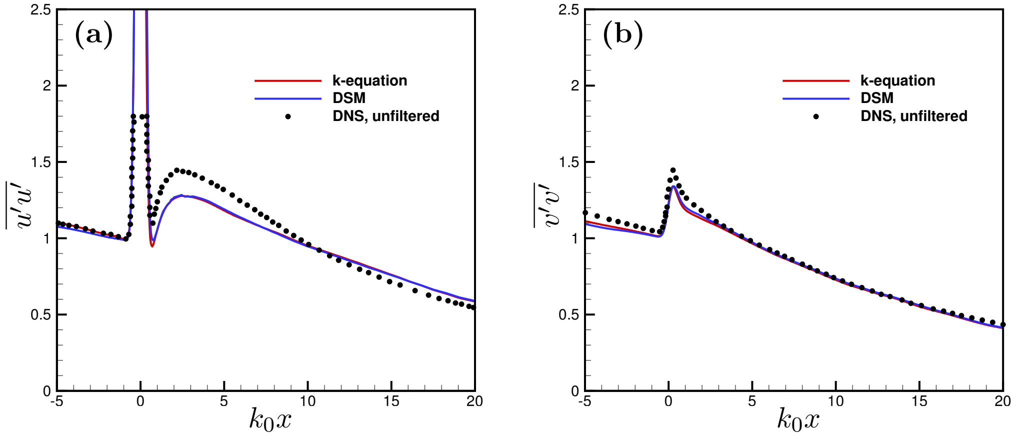

Figure 4.17: Distribution of averaged turbulent intensities for High $Re$ case. The shock position has been shifted to $x = 0$ for comparison with DNS.

immediate vicinity of the shock wave. This behavior is due to statistical intermittency associated with motions of the shock wave. Due to shock oscillation, the shock jump would show up as unsteadiness to a fixed probe. Such behavior is also observed in DNS of shock/turbulent interaction where the shock thickness is resolved [85, 83]. Figure 4.17 compares the distribution of averaged turbulent intensities calculated from the k-equation model with the DNS and DSM results for the high $Re$ case [84]. All of the curves in figure 4.17 are normalized by $\overline{u'u'}$ immediately upstream of the shock as in DNS. Overall, the agreement is reasonable. The k-equation model under-predicts decaying rate of $\overline{u'u'}$ in the far downstream. However, considering that the current LES uses only $1.8 \times 10^5$ CVs compared to $1.5 \times 10^8$ CVs in the DNS, the agreement is quite good. Note that, the DNS inflow is somehow less isotropic than the current LES inflow due to different inflow generation methodologies. This may be responsible for the small difference between the LES and DNS in $\overline{v'v'}$ at the inflow. Compared with DSM, $\overline{u'u'}$ predicted by the k-equation model is slightly closer to DNS results for low $Re$ case (figure 4.16 ($a$)); while for high $Re$ case, the k-equation model results are almost identical to those of DSM (figure 4.17). This is reasonable, because strong shock and turbulent interaction is dominated by linear effects [83], so that the contribution of SGS models at the shock front is less obvious.

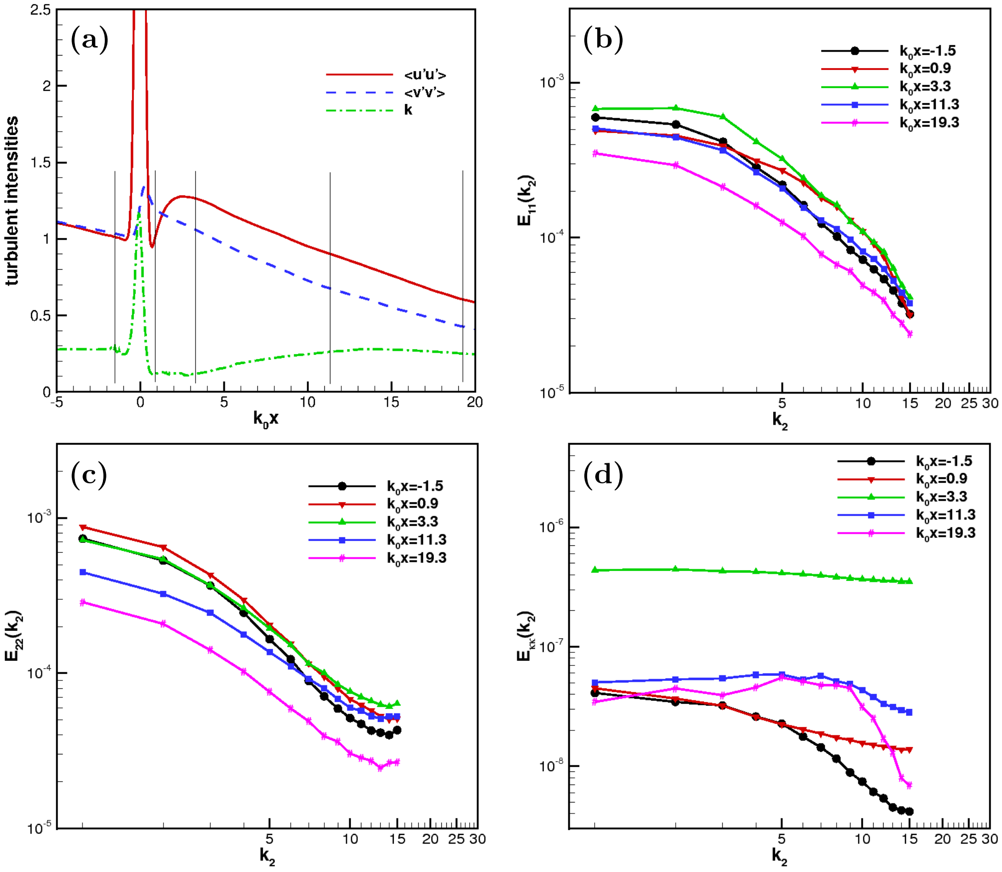

Figure 4.18: Evolution of turbulent energies (a) and one dimensional energy spectra: (b) $E_{11}$; (c) $E_{22}$; (d) $E_{kk}$ (energy spectra of SGS kinetic energy).

### Energy spectra

Figure 4.18 shows one dimensional energy spectra of velocity components and SGS kinetic energy at different locations. In the current simulation, the flow is isotropic upstream of the shock and axisymmetric downstream of the shock, so that $E_{22}(k_2) \approx E_{33}(k_2)$; therefore $E_{33}$ is not plotted here. Distributions of SGS kinetic energy $k$ is also plotted in figure 4.18 $(a)$ with vertical black lines marking the locations where the energy spectra are calculated. As shown, $k_0x = -1.5$ is at the shock upstream; $k_0x = 0.9$ is almost immediately downstream of the shock; $k_0x = 3.3$ is a location near the peak value of $\overline{u'u'}$ at shock downstream; and $k_0x = 11.3$ and $k_0x = 19.3$ are two far

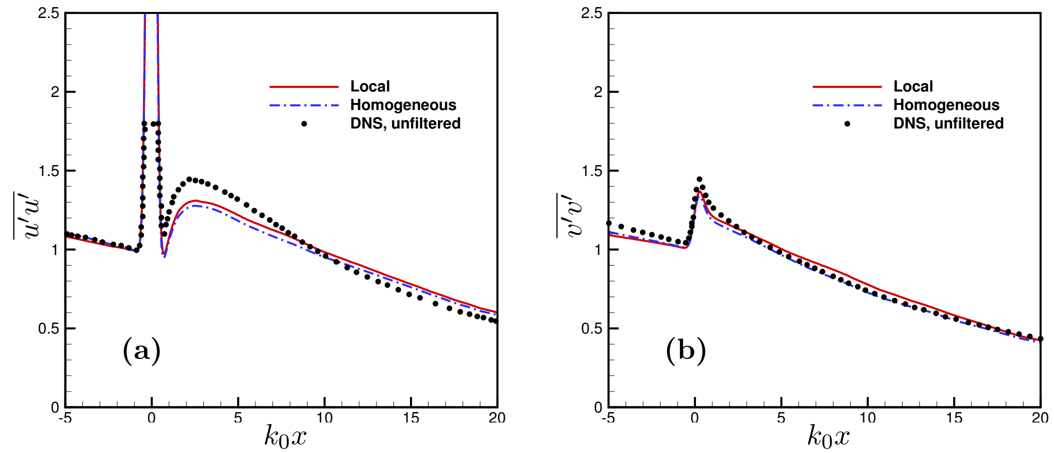

Figure 4.19: Comparison of local averaging and averaging over homogeneous directions.

downstream locations.

Note that even the smallest scales have large energy levels. Seen from figure 4.18 (*b*), across the shock (from $k_0x = -1.5$ to $k_0x = 0.9$), the energy spectrum of $E_{11}$ is amplified in medium wave numbers, decreases in small wave numbers and is preserved at high wave numbers. This indicates a decrease of turbulent length scale in $x$ direction. From $k_0x = 0.9$ to $k_0x = 3.3$, amplification of $E_{11}$ is observed to be at higher and smaller wave numbers. Figure 4.18 (*c*) shows $E_{22}$ is more enhanced at small scales across the shock, which is similar to the observation of Lee *et al.* [85]. Further downstream, the spectrum drops over the entire range of wave numbers.

Figure 4.18 (*d*) shows the evolution of the one dimensional energy spectra of SGS kinetic energy. Interestingly, the evolution of $E_{kk}$ shows more activity at small scales. For example, $E_{kk}$ is magnified more at high wave numbers from $k_0x = -1.5$ to $k_0x = 0.9$ and $k_0x = 3.3$, and decays faster at small scales from $k_0x = 3.3$ to $k_0x = 11.3$ and to $k_0x = 19.3$. At $k_0x = 3.3$, the spectrum is enhanced by more than one order of magnitude, and the small scales possess as high energy as large scales.

### Localization

The dynamic Smagorinsky model [51, 28] is known to require regularization to ensure stability. Averaging over homogeneous directions is most common. Such averaging is not practical for flows without homogeneous directions or flow solvers that use unstructured

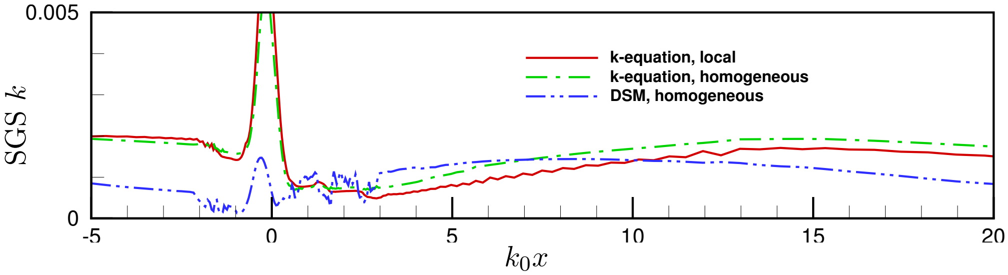

Figure 4.20: Distribution of mean SGS kinetic energy for high *Re* case of shock/turbulent interaction.

girds. The proposed dynamic k-equation model appears to have an advantage over the DSM in that it is stable during the use of local averaging over the neighboring CVs for the dynamic procedures. Figure 4.19 compares the results of k-equation model derived from local averaging and averaging over homogeneous directions. When locally averaged, the model is slightly less dissipative, so that the decay rate of turbulent energy (intensities) is slightly slower at the inflow and downstream of the shock. Similar behavior of the decay rate of turbulent kinetic energy is also observed in simulations of temporally and spatially decaying isotropic turbulence when local averaging is used, and is considered reasonable. Local averaging over-predicts the turbulent intensities a little bit more than homogeneous averaging at far downstream, but the difference is still small. The robustness of the localized k-equation model may be attributed to two reasons. First, the performance (in terms of the resolved field) of k-equation model is less sensitive to $k$ even for initial value problems (figure 4.6). Second, the introduction of k-equation introduces history effects into SGS kinetic energy, so that the change of $k$ is milder than Yoshizawa model which is more sensitive to instantaneous flow condition and grid resolution. As shown in figure 4.20, in the shock near field, where the mesh is clustered and the interaction is also more intense, much more oscillation in the mean SGS kinetic energy is observed for DSM than the k-equation model using either local or homogeneous averaging. The unphysical oscillation of SGS kinetic energy in DSM may well generate locally small or high eddy viscosity, and cause unexpected numerical instability. The overall performance of the localized dynamic k-equation model is promising, which facilitates its application to simulations of complex flow fields on unstructured grids.

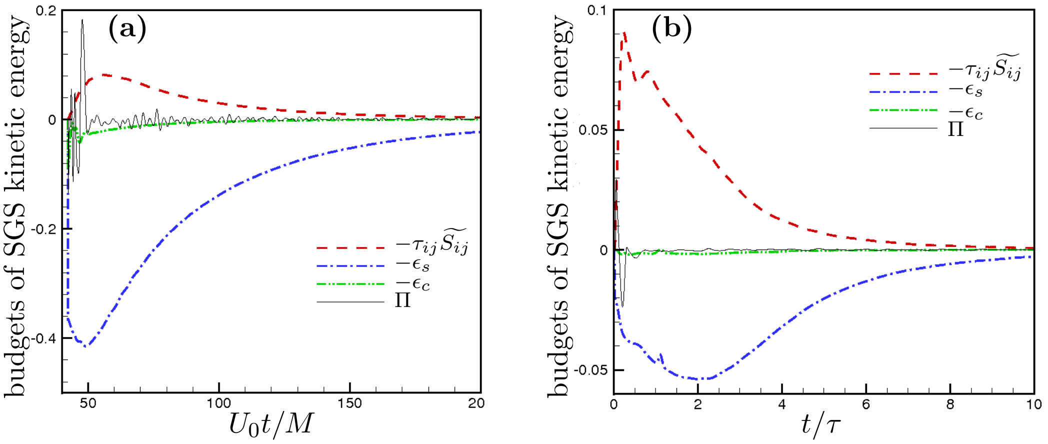

Figure 4.21: Budget of SGS k-equation for the decaying isotropic turbulence: (a) CBC; (b) compressible case with $M_t = 0.6$ initially.

## 4.4 Relevance of dilatational dissipation and pressure dilatation terms

The pressure dilatation term and dilatational dissipation term are the primary terms that differentiate the compressible SGS kinetic energy equation from its incompressible counterpart. To evaluate their relevance, the budgets of terms in the SGS kinetic energy equation are studied. Figure 4.21 shows the temporal evolution of each term on the right hand side of SGS kinetic energy equation for decaying isotropic turbulence. All the terms are normalized by $\rho u_{rms}^2/\tau$ at $t = 0$. Figure 4.21 (a) is for CBC isotropic turbulence, and figure 4.21 (b) is for the highly compressible case with initial $M_t = 0.6$ and $Re_\lambda = 67.6$. Due to spatial homogeneity, the spatial average of terms in divergence form in SGS kinetic energy equation is zero, thus these terms are not plotted. Shown in figure 4.21 (a), the terms $\epsilon_s$ and $-\tau_{ij}\widetilde{S_{ij}}$ are the most prominent terms. The term $-\tau_{ij}\widetilde{S_{ij}}$ is the SGS dissipation term in the transport equation for resolved kinetic energy [72], and acts as the production term for SGS kinetic energy. $\epsilon_s$ is the dissipation term and is consistently larger than $-\tau_{ij}\widetilde{S_{ij}}$, which causes the SGS kinetic energy to decay. Both the magnitudes of $\epsilon_s$ and $-\tau_{ij}\widetilde{S_{ij}}$, as well as the difference between them, decreases temporally, which results in a reducing decay rate of SGS kinetic energy as observed in figure 4.5 ($a$). Large initial transients are observed for pressure dilatation $\Pi$, which is due to the forced incompressible behavior in the initial condition (inconsistent initial

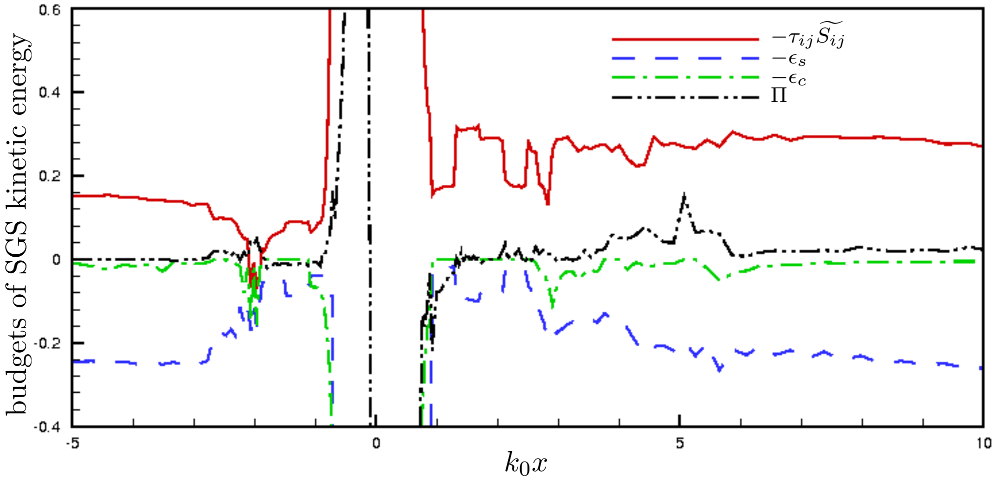

Figure 4.22: Budgets of SGS kinetic energy for shock/turbulence interaction.

condition [86]). Similar transient behavior can also be observed for $\epsilon_c$, but the magnitude is much smaller. Figure 4.21 (b) shows that in the highly compressible simulation, these terms behave similarly to the quasi-incompressible case, except that the production term $-\tau_{ij}\widetilde{S_{ij}}$ is higher than the dissipation term $\epsilon_s$ initially. So the SGS kinetic energy will increase at the beginning then decay afterwards, as shown in figure 4.8 (a).

Figure 4.22 shows the budgets of SGS kinetic energy equation for shock/turbulence interaction with high $Re$ and high $M_t$. All the curves in figure 4.22 are normalized by $\rho k/\tau$ at the inlet, where $k$ is the SGS kinetic energy, and $\tau$ is the eddy turn-over time of the inflow turbulence. The whole domain can be approximately divided into three regions: before shock ($k_0x < -0.8$), intermittency region ($-0.8 < k_0x < 0.8$) and post shock ($k_0x > 0.8$). Here, we focus on the regions before and after the shock wave. Before the shock, the flow is essentially spatially decaying isotropic turbulence, and the relevance of these four terms are similar to temporally decaying isotropic turbulence. In the near field ahead of the shock, all the terms drop in magnitude due to the clustered mesh. In the vicinity of the shock, all of the terms increase significantly due to intermittency. Downstream of the shock, the magnitude of production term $-\tau_{ij}\widetilde{S_{ij}}$ is higher than that before the shock; while the solenoidal dissipation $\epsilon_s$ keeps similar levels as before. It appears that both pressure dilatation $\Pi$ and dilatational dissipation $\epsilon_c$ become more important across the shock. Far downstream, $\epsilon_c$ and $\Pi$ decrease in

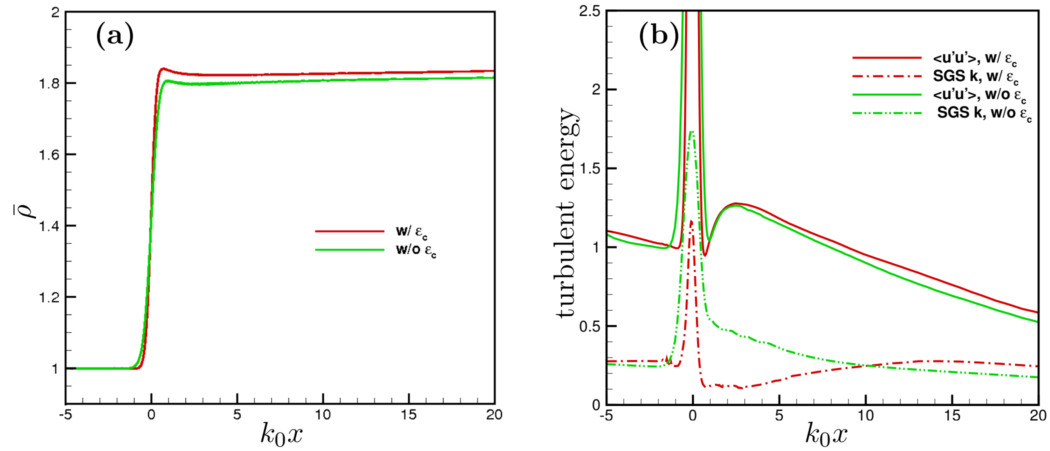

Figure 4.23: Effect of dilatational dissipation $\epsilon_c$, on (a) the mean density and (b) turbulent intensity.

magnitude, and the four terms behave similarly to decaying turbulence.

From the analysis of the budgets of SGS kinetic energy equation, we see that the dilatational dissipation term has negligible effect on the sub-grid scale turbulence away from shock. However, across a shock the dilatational dissipation becomes important. Also the pressure dilatation term is important during the acoustic transient, but may have limited effect in the mean. To confirm our observation, we perform simulations with/without pressure dilatation and dilatational dissipation separately.

For the decaying isotropic turbulence, it is found that turning these two terms on and off does not make discernable difference to both of the resolved and SGS field (not shown here), which is consistent with our observation that $\epsilon_c$ is negligible relative to $\epsilon_s$, and the net effect of $\Pi$, which oscillates around zero, is small. For shock/turbulence interaction, without pressure dilatation model, the results almost collapse with those shown in figure 4.17. However, without dilatational dissipation, both of the mean and fluctuation field will be affected. Figure 4.23 compares the mean density and turbulent energy distributions along the streamwise direction for shock/turbulence interaction between dynamic k-equations models with and without dilatational dissipation term. In figure 4.23 (*b*), it appears that, without dilatational dissipation, the dissipation of SGS kinetic energy across the shock will not be enough. So, the SGS kinetic energy after the shock relaxes too slowly to its normal value. High SGS kinetic energy will generate larger eddy viscosity and dissipates more of the turbulent intensities after the shock. Furthermore, through the total energy equation, this effect will be passed on to the mean flow field as shown in figure 4.23 ($a$). Though the pressure dilatation term appears to have less effect on the mean profiles, this trend should not be assumed to hold for other problems. It does appear to be important instantaneously when acoustic interactions become significant.

## 4.5 Summary

A dynamic one equation eddy viscosity model for compressible LES is proposed. The SGS kinetic energy transport equation is formally derived, and the residual terms in the filtered total energy equation that are neglected in standard DSM have been revisited. The unclosed terms are modeled and the model coefficients are determined dynamically. An algebraic model based on series expansion is proposed for the pressure dilatation term, and a different dynamic procedure for the dissipation terms in energy equations is suggested. *A priori* tests using DNS of decaying isotropic turbulence are performed, which shows that the proposed dynamic k-equation model has comparable correlation level in SGS stress and SGS heat flux to DSM model, and the suggested model for pressure dilatation correlates well with its actual value. The proposed dynamic k-equation model is applied to the decaying isotropic turbulence and isotropic turbulence/normal shock interaction problems in *a posteriori* tests. When compared to available experimental and DNS results, the k-equation model shows good agreement. It improves energy spectra at high wave numbers for decaying isotropic turbulence, and performs similarly to DSM in shock/turbulence interaction due to the dominant linear effect. In shock/turbulence interaction, the one dimensional energy spectra of resolved velocity components and SGS kinetic energy are examined, and the behavior of SGS kinetic energy across the shock is discussed. The budgets of SGS kinetic energy equation shows that the dilatational dissipation is important for shock/turbulent interaction, but may be less important for decaying isotropic turbulence. The pressure dilatation term does not seem to have noticeable net effects in the mean, but instantaneously its magnitude is comparable to other dominant terms, especially when acoustic transients are present.

In addition, the proposed dynamic k-equation model requires less regularization for stability, and is able to be localized easily without degrading its performance, which is encouraging for simulations of high speed flows in complex geometries.

# Chapter 5

# DNS/LES of supersonic turbulent boundary layer

The flat plate turbulent boundary layer is a classic and important problem. It is the basis of numerous complex flow configurations such as flow around an airfoil, jets in cross-flow, compression corner, etc. Its simple geometrical configuration makes it a benchmark problem for evaluation of numerical algorithms and turbulent models. However, simulations of flat plate turbulent boundary layer become challenging as the Reynolds number $Re_\theta$ increases. Here $\theta$ is the momentum thickness of the turbulent boundary layer. At very high Reynolds numbers, wall models must be involved to derive the correct stress conditions near the wall. RANS and Hybrid RANS/LES (DES) can usually be applied to turbulent boundary layers with much higher Reynolds numbers ($Re_\theta \sim 10^5$), with the sacrifice of turbulent flow dynamics not being captured near the wall. LES models that are applicable to high $Re$ turbulent boundary layer is highly desirable. In this chapter, DNS and LES are performed for a Mach 2.9 supersonic turbulent boundary layer. This chapter discusses the recycling-rescaling turbulent inflow boundary generation technique for unstructured compressible flow solvers, and evaluates the proposed dynamic $k$-equation in Chapter 4.

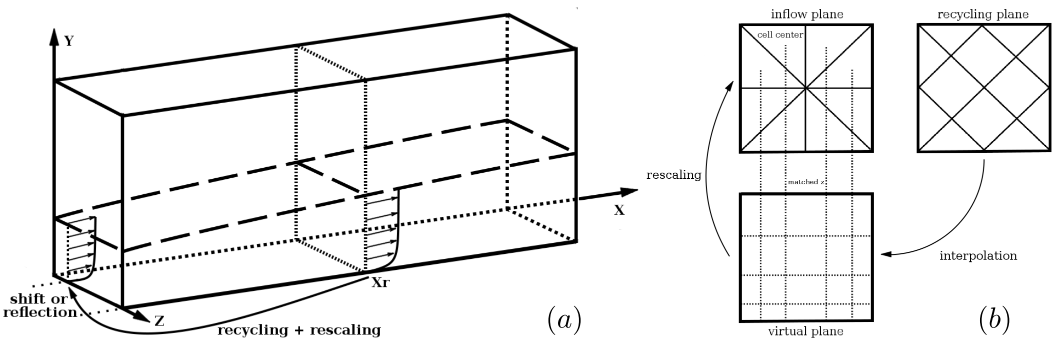

Figure 5.1: Schematics of: (*a*) computational domain and (*b*) recycling-rescaling method on an unstructured mesh.

## 5.1 A recycling-rescaling technique for unstructured compressible flow solvers

### 5.1.1 Formulation

Figure 5.1 (*a*) shows the schematic of the recycling-rescaling method. At a reference downstream location, $x = x_r$, the instantaneous boundary layer data is collected, properly scaled, and then reintroduced as an updated inflow boundary condition. The recycling-rescaling technique was introduced by Lund *et al.* [87] in the simulation of incompressible turbulent boundary layer on a flat plate, which was then extended to compressible boundary layer simulations by Urbin and Knight [88], Stolz and Adams [89] and Xu and Martin [90]. This method decomposes the flow field variables on the recycling plane into mean and fluctuation components, which are then rescaled based on the boundary layer thicknesses at the recycling and inflow planes using the law of the wall and defect law for inner layer and outer layer respectively. In the current study, we adapt Stolz and Adams' [89] method to our unstructured flow solver, and consider both adiabatic and isothermal wall conditions. We further assume that the pressure fluctuation is negligible so that the rescaled temperature profile is related to and can be solved from the rescaled density profile owing to the state equation for ideal gas. Therefore, the rescaling equation for temperature is dropped from the original equations of Stolz and Adams' [89] work. To be exact, the instantaneous flow field variables at the inflow can be calculated by:

$$\begin{aligned} u\left(x_{in}, y, z, t\right) &= \beta[\gamma U\left(x_r, \gamma^n y, t\right) + \left(1-\gamma\right) U_\infty \\ &\quad +\gamma u'\left(x_r, \gamma^n y, z, t\right)] + \left(1-\beta\right)\left[\gamma U\left(x_r, \gamma y, t\right)\right. \qquad (5.1) \\ &\quad \left.+\gamma u'\left(x_r, \gamma y, z, t\right)\right], \\ v\left(x_{in}, y, z, t\right) &= \beta[V\left(x_r, \gamma^n y, t\right) + \gamma v'\left(x_r, \gamma^n y, z, t\right)] \\ &\quad +\left(1-\beta\right)\left[V\left(x_r, \gamma y, t\right) + \gamma v'\left(x_r, \gamma y, z, t\right)\right], \qquad (5.2) \\ w\left(x_{in}, y, z, t\right) &= \beta\gamma w'\left(x_r, \gamma^n y, z, t\right) \\ &\quad +\left(1-\beta\right)\gamma w'\left(x_r, \gamma y, z, t\right), \qquad (5.3) \\ \rho\left(x_{in}, y, z, t\right) &= \beta[\Re\left(x_r, \gamma^n y, t\right) + \gamma\rho'\left(x_r, \gamma^n y, z, t\right)] \\ &\quad +\left(1-\beta\right)\left[\Re\left(x_r, \gamma y, t\right) + \gamma\rho'\left(x_r, \gamma y, z, t\right)\right]. \qquad (5.4) \end{aligned}$$

Here, the subscript '*in*' denotes quantities at the inflow, and the subscript '*r*' denotes quantities at the recycling plane. $\beta$ is the weighting function proposed by Lund *et al.* [87], and is used to blend the inner and outer layer. It takes the form of

$$\beta\left(\eta\right) = \frac{1}{2}\left\{1 + tanh\left[\frac{\alpha\left(\eta - b\right)}{\left(1-2b\right)\eta + b}\right] \Big/ tanh\left(\alpha\right)\right\}, \qquad (5.5)$$

with $\alpha = 4$ and $b = 0.2$. The expression for $\gamma$ is

$$\gamma^n = \frac{\theta_r}{\theta_{in}} \approx \frac{\delta_{0,r}}{\delta_{0,in}}, \qquad (5.6)$$

where $\delta_0$ and $\theta$ are 99% boundary layer thickness and momentum thickness; $n = 8$ for isothermal wall and $n = 10$ for adiabatic wall. $U(x_r, y, t)$, $V(x_r, y, t)$, $\Re(x_r, y, t)$ are the time averaged streamwise velocity, wall-normal velocity and density profiles on the recycling plane at time $t$. Here, a sliding time averaging is used to calculate these mean flow variables, i.e.

$$Q\left(x, y, t\right) = \left(1 - \frac{dt}{T_s}\right) Q\left(x, y, t - dt\right) + \frac{dt}{T_s}\,\hat{q}\left(x, y, t\right), \qquad (5.7)$$

where Q denotes either $U$, $V$ or $\Re$, $dt$ is the time step, $T_s$ is a suitable sampling period and was taken as $T_s \approx 8\ \delta_{0,in}/U_\infty$ in Stolz and Adams [89]'s work; $\hat{q}(x, y, t)$ is the spanwise average of flow variables at time instant $t$, i.e.

$$\hat{q}\left(x, y, t\right) = \frac{1}{L_z} \int_0^{L_z} \tilde{q}\left(x, y, z, t\right) dy. \tag{5.8}$$

Here, $L_z$ is the width of the computational domain, and $\tilde{q} = \overline{\rho q}/\bar{\rho}$ denotes the resolved (Favre-filtered) flow variable. In equations (5.1), (5.2), (5.3) and (5.4), $u'$, $v'$, $w'$, $\rho'$ are fluctuations of streamwise, wall-normal and spanwise velocities and density fluctuation respectively, which are calculated from

$$q'\left(x, y, z, t\right) = \tilde{q}\left(x, y, z, t\right) - Q\left(x, y, t\right). \tag{5.9}$$

Finally, the dynamic shift/reflection method Morgan *et al.* [91] is applied to reduce low frequency streamwise and spanwise correlations observed in the original methods (e.g. Stolz and Adams [89], Spalart *et al.* [92] and Morgan *et al.* [91].

For unstructured computational meshes (shown in figure 5.1 (*b*)), the rescaling procedure (equations. (5.1),(5.2), (5.3), (5.4)) and spanwise averaging (equation (5.8)) is nontrivial. This difficulty can be resolved by creating a "virtual" two-dimensional Cartesian mesh with appropriate $y$ and $z$ coordinates at the recycling plane, so that the flowfield variables on the recycling plane can be mapped onto the virtual plane using high order interpolation. Then, the spanwise averaging can be easily carried out on the virtual plane, as well as the rescaling procedure between the inflow plane and virtual recycling plane. It is favorable to match the $z$ coordinates of the virtual plane to that of the inflow plane, so that no additional interpolations in $z$ direction are required when rescaling. A regular discretization in $y$ direction based on $Re_\theta$ of the boundary layer is good enough, since interpolations in wall-normal direction is inevitable even for structured grids [87]. Further, if the dynamic shift/reflection technique is considered to reduce nonphysical correlations, interpolations in $z$ direction may be involved for if the meshes in $z$ direction on the inflow and virtual recycling planes are not uniform. However, in practice, it is very easy to create a good Cartesian type surface mesh which is uniform in $z$ direction on the inflow plane (therefore on the virtual plane as well), so that interpolations in $z$ direction can be totally avoided.

### 5.1.2 Validation

DNS of a supersonic turbulent boundary layer are performed to evaluate the proposed recycling-rescaling method. The flow conditions are based on Bookey *et al.*'s [93] experiments. The freestream Mach number is $M_\infty = 2.9$, and the Reynolds number is $Re_\infty = (\rho_\infty u_\infty)/\nu_\infty = 635000$ per unit length. The length of the computational domain is 4.5 unit length, the height and the spanwise extents are 0.5 and 0.175 unit length, respectively. The inflow starts at $x = 4.0$, and the wall is located at $y = 0.0$. The domain is periodic in the spanwise ($z$) direction. Zero gradient boundary conditions are imposed at the outflow ($x = 8.5$), and at the top boundary, freestream boundary conditions are imposed. At the top boundary, a sponge layer is imposed to absorb reflected shock waves and acoustics. At the inflow, the boundary layer thickness is prescribed as $\delta_{0.99} = 0.02$. At the wall, an isothermal no-slip boundary conditions are implemented. The wall temperature is kept at $T_w = T_0$, where $T_0 = (1 + \frac{\gamma-1}{2}M_\infty^2)T_\infty$ is the stagnation temperature. Sutherland's law is applied to the computation of viscosity, with a reference temperature of $T_{ref} = T_\infty = 110K$ and reference viscosity of $\mu_{ref} = \mu_\infty$. The computational mesh consists of 24 million hexahedral control volumes, which is uniform in $z$- and $x$-directions up to $x = 7.0$ and stretched in $y$-direction and $x$-direction after $x = 7.0$. The typical grid spacings are $\Delta_x = 2.5 \times 10^{-3}$, $\Delta_{y_{min}} = 5 \times 10^{-5}$, $\Delta_z = 9.1 \times 10^{-4}$, which results in $\Delta_x^+ = 15$, $\Delta_{y_{min}}^+ = 0.3$, $\Delta_z^+ = 5.4$ in viscous wall units. On this domain, a supersonic turbulent boundary layer with $Re_\theta = 1000 \sim 3000$ is developed. Muppidi and Mahesh [47] performed DNS of roughness-induced transition of supersonic boundary layer under similar flow condition and grid resolution, which shows that this grid resolution is good enough for this turbulent boundary layer to be reasonably resolved.

#### Instantaneous flow field

Figures 5.2 ($a$), ($b$), ($c$) and ($d$) show the contours of instantaneous streamwise velocity, density, divergence and density gradient magnitude, respectively. The turbulent boundary layer is observed to be reasonable from all the instantaneous flow variables. It is shown that at the inflow, the freestream region above the boundary layer is undisturbed. A wake leading edge shock is discernible from the density and divergence contours, which

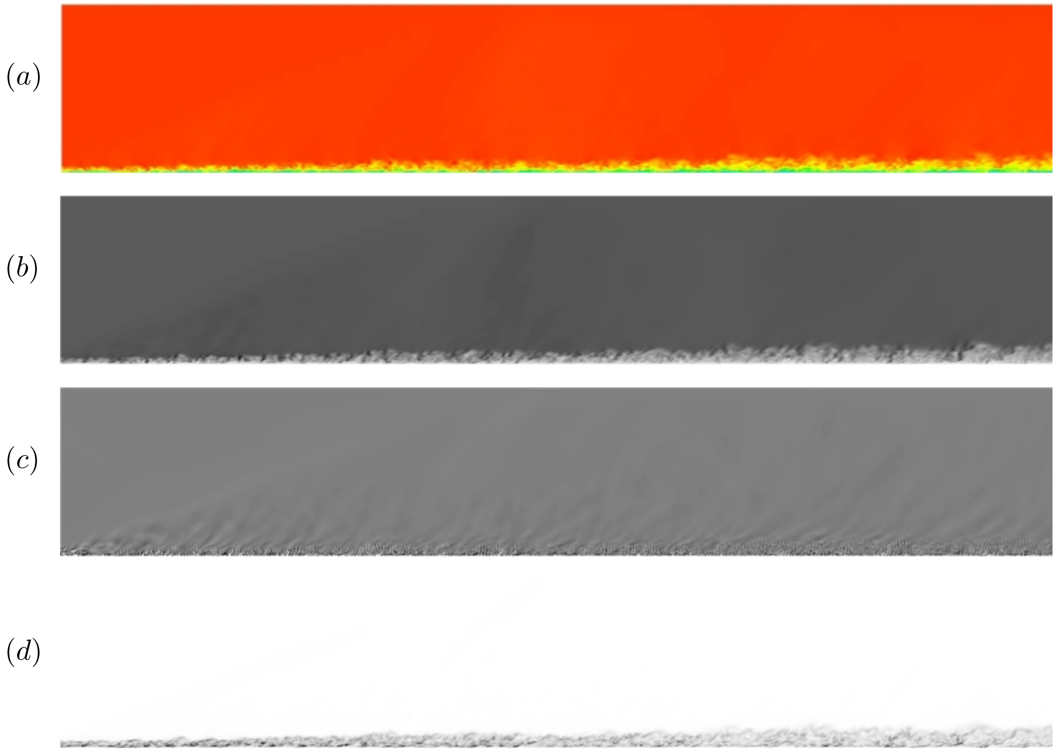

Figure 5.2: Contours of instantaneous (*a*) streamwise velocity, (*b*) density, (*c*) divergence and (*d*) density gradient magnitude.

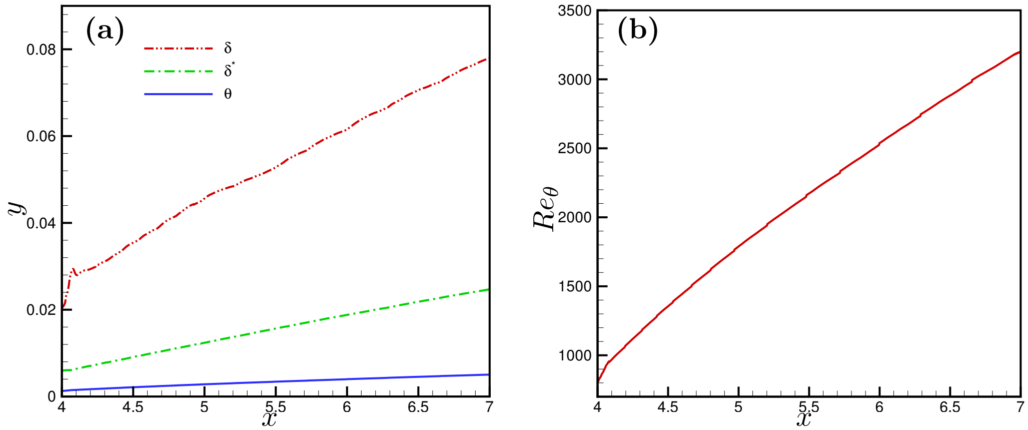

Figure 5.3: Evolution of (*a*) Boundary layer thicknesses and (*b*) $Re_\theta$ along streamwise direction.

is absorbed by the sponge layer imposed at the top boundary. Acoustic waves are observed above the turbulent boundary layer from the divergence contours, which are also absorbed by the top sponge layer so that they do not reflect back and interfere the downstream flow fields.

### Statistics

Figure 5.3 (*a*) shows the growth of the thicknesses of the turbulent boundary layer. The curve for 99% thickness $\delta$ is less smooth than the displacement thickness and momentum thickness, because of its definition. A small transient region is observed near the inflow, but it is very short. Figure 5.3 (*b*) shows the growth of $Re_\theta$ along the streamwise direction. For the current simulation, $Re_\theta$ ranges approximately from 1000 to 3000. Figures 5.4 (*a*) compares the Van Driest transformed streamwise velocity profiles calculated from the current simulation with experimental results. All of the profiles comply with the law of the wall, and show good agreement with the experimental results. Figures 5.4 (*b*) compares the current velocity profiles with available DNS under similar flow conditions. It shows that the current DNS results almost collapse on the past simulations. Figure 5.5 (*a*) shows the turbulent intensity profiles across the boundary layer. It is observed that the current simulation agrees well with the DNS of Guarini *et al.* [94] most of the time, except in $\overline{u'u'}$ between $0.2 < y/\delta < 0.7$. The intensity profiles agree well with the experimental results. Figure 5.5 (*b*) shows the skin friction

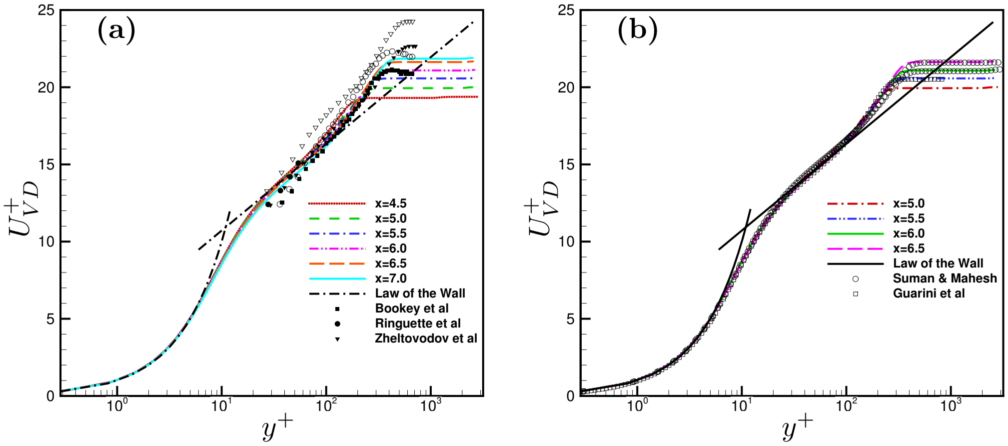

Figure 5.4: Comparison of Van Driest transformed velocity profiles with (*a*) experimental and (*b*) past DNS results.

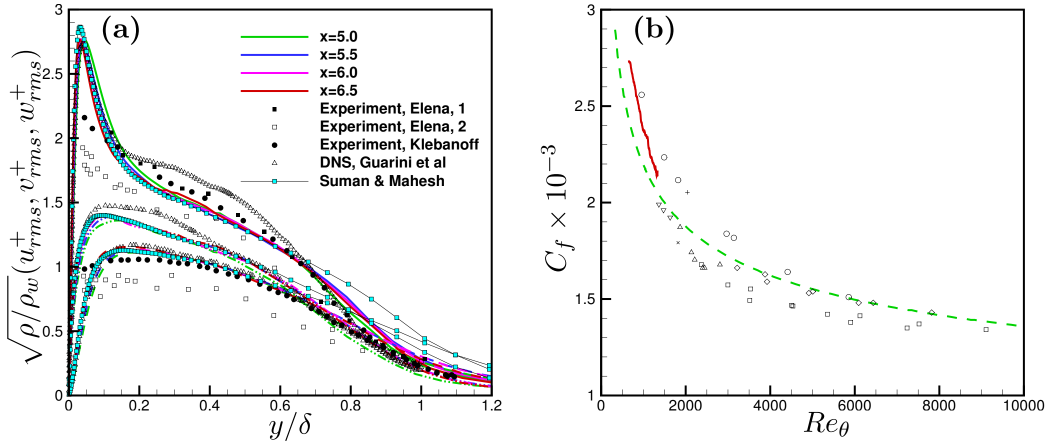

Figure 5.5: Comparison of (*a*) turbulent intensities and (*b*) skin friction distribution profiles with experimental and past DNS results.

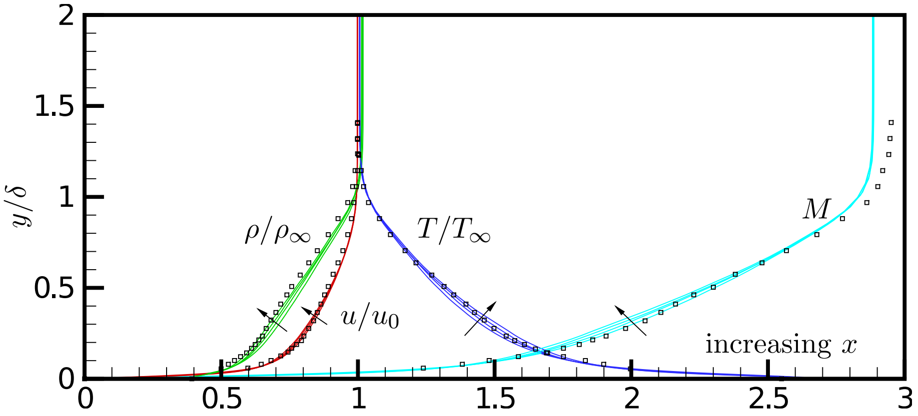

Figure 5.6: Profiles of density, streamwise velocity, temperature and Mach number. Present simulation – solid curves, Zheltovodov *et al.* – symbols.

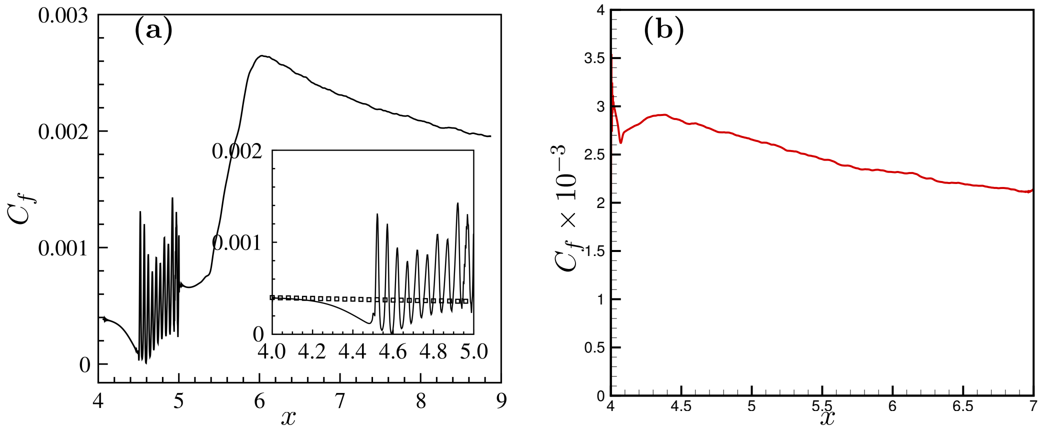

Figure 5.7: Evolutions of $C_f$ along $x$ direction: ($a$) roughness induced transition (Muppidi & Mahesh, 2011); ($b$) current recycling-rescaling method.

coefficient distribution along the streamwise direction. It is observed that, $C_f$ calculated from the current simulation is reasonable, and lays in between available experimental and simulation data. Figure 5.6 compares mean thermodynamic variables with the Zheltovodov *et al.*'s [95] experimental results. Again, good agreement is achieved. Note that in Zheltovodov *et al.*'s experiments, the freestream Mach number is $M_\infty = 3$, therefore small difference in Mach number profiles is observed outside of the boundary layer. The proposed recycling-rescaling methodology appears to work well in generating realistic turbulent boundary layer inflow conditions.

Roughness-induced transitions of boundary layer can also be used to provide turbulent boundary layers. The comparison to the DNS results of Muppidi & Mahesh [47] is therefore also a comparison between two different turbulent boundary layer generation methods, since the current DNS uses the same numerical algorithm and flow conditions as in Muppidi & Mahesh (2011)'s work. While the above figures validated both turbulent generator, some differences between the two set of DNS results are observed. As shown in figure 5.5, the current simulation agrees slightly better with the past work in that Muppidi & Mahesh (2011)'s calculation: (i) slightly over-predicts $\overline{u'u'}$ near the wall; (ii) over-predicts all three Reynolds stress in the outer boundary layer $y/\delta > 0.7$. Another advantage of the recycling-rescaling method is that it requires a much shorter length of development for the boundary layer to reach fully developed status. This can be shown from the evolution of the skin friction coefficients along the streamwise direction. Figure 5.7 compares the $C_f$ distributions along $x$ between the recycling-rescaling method and roughness-induced transition method. It shows that it takes less than 0.5 ($4.0 \sim 4.5$) unit length for the turbulent boundary layer to develop by using recycling-rescaling method, compared to more than 1.0 ($5.0 \sim 6.0$) when using roughness-induced transition. In terms of turbulent boundary layer generator, it is therefore preferable to use the recycling-rescaling method which is favorable in reducing the length of computational domain and cost.

## 5.2 LES of supersonic turbulent boundary layer

In this section, large-eddy simulations of the Mach 2.9 supersonic turbulent boundary layer discussed above are performed using the proposed dynamic $k$-equation model

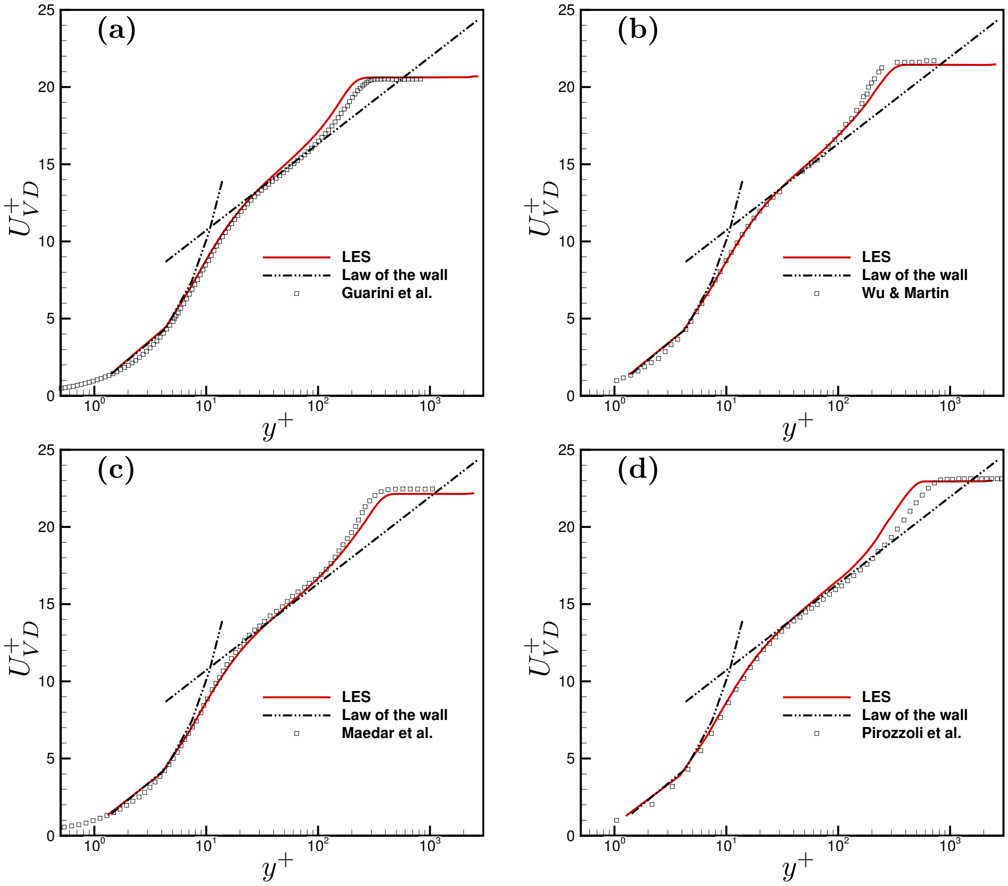

Figure 5.8: Comparison of Van Driest transformed velocity profiles with past DNS results at four different $Re_\theta$: ($a$) $Re_\theta = 1450$, ($b$) $Re_\theta = 2400$, ($c$) $Re_\theta = 3000$, ($d$) $Re_\theta = 4350$.

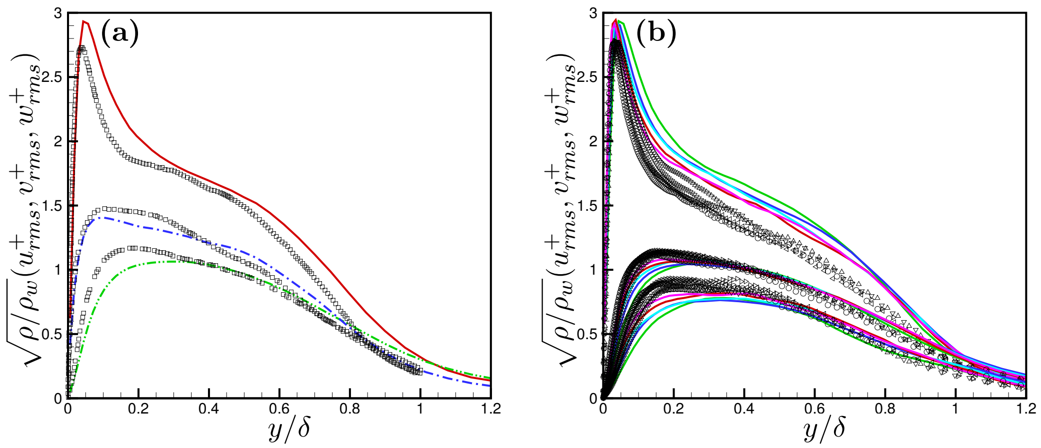

Figure 5.9: Comparison of the resolved Reynolds stresses with (*a*) Guarini *et al.*'s and (*b*) present DNS results.

proposed in chapter 5. The flow conditions are exactly the same as in the DNS, so that the DNS results can be used to evaluate the LES results. The recycling-rescaling method proposed in last section is applied to provide turbulent boundary layer at the inflow. Same boundary conditions conditions are imposed at corresponding boundaries. Boundary conditions are required for the SGS kinetic energy equation. At the inflow, scale similarity assumption is applied, i.e. $k = \frac{1}{2}\left(\widehat{\widetilde{u}_i\widetilde{u}_i} - \widehat{\widetilde{u}}_i\widehat{\widetilde{u}}_i\right)$. On the wall, $k$ is set to be zero. At other boundaries, no-gradient boundary condition is imposed for $k$. The computational domain is extended to $x = 9$ and meshed uniformly in $x$- and $z$-directions. The computational mesh is coarsen based on the above DNS mesh, and the grid resolution becomes $\Delta_x = 3.3 \times 10^{-3}$, $\Delta_{y_{min}} = 2.5 \times 10^{-4}$, $\Delta_z = 2.7 \times 10^{-3}$, which results in $\Delta_x^+ = 22$, $\Delta_{y_{min}}^+ = 1.5$, $\Delta_z^+ = 18$ in viscous wall units.

Figures 5.8 and 5.9 show the comparison of the profiles of Van Driest transformed streamwise velocity and the resolved Reynolds stresses with the past and present DNS results at matched $Re_\theta$. Good agreement is observed for the Van Driest transformed streamwise velocity profiles at all $Re_\theta$. All profiles of the resolved Reynolds stress show that the current LES over-predicts $\overline{u'u'}$, and under-predicts $\overline{v'v'}$ and $\overline{w'w'}$. This is reasonable for LES of turbulent boundary layer on relatively coarse grids.

## 5.3 Summary

In this chapter, an inflow turbulent boundary layer generator based on recycling-rescaling technique is realized for our unstructured compressible flow solver, and compared to a naturally transition boundary layer. This method is validated using DNS of Mach 2.9 supersonic turbulent boundary layer. The DNS shows good agreement with available experimental data and past DNS results. It is observed that with the proposed recycling-rescaling technique the turbulent boundary layer becomes fully developed faster than it does in the boundary layer transition due to distributed roughness elements. LES of the Mach 2.9 supersonic turbulent boundary layer is then performed using the recycling-rescaling turbulent generator and dynamic $k$-equation model (section 4). Good agreement in both mean flow quantities and turbulent intensities is observed between the LES results and DNS data.

# Bibliography

[1] N Park and K Mahesh. Numerical and modeling issues in LES of compressible turbulent flows on unstructured grids. *AIAA Paper 2007–0722*, 2007.

[2] J. G. Santiago and J. C. Dutton. Velocity Measurements of a Jet Injected into a Supersonic Crossflow. *Journal of propulsion and power*, 13(2):264–273, 1997.

[3] S Beresh, R Erven, J Henfling, and R Spillers. Penetration of a Transverse Supersonic Jet into a Subsonic Compressible Crossflow. *AIAA Journal*, 43:379–389, February 2005.

[4] F.~S. Billig and J.~A. Schetz. Penetration of gaseous jets injected into a supersonic stream. *Journal of Spacecraft and Rockets*, 3:1658–1665, November 1966.

[5] Krishnan Mahesh. The interaction of jets with crossflow. *Annual Review of Fluid Mechanics*, 45(1):null, 2013.

[6] M V Morkovin, Jr. Pierce C. A., and C E Craven. Interaction of a side jets with a supersonic main stream. *Bull. 35, Engineering Research Institute, University of Michigan*, September 1952.

[7] J E McAulay and A J Pavli. Cold-flow performance of thrust-vector control by secondary injection. *NASA-TM-X-416*, 1960.

[8] Robert W Cubbison, Bernhard H Anderson, and James J Ward. Surface Pressure Distributions with a Sonic Jet Normal to Adjacent Flat Surfaces at Mach 2.92 to 6.4. *NASA-TN-D-580, E-1025*, 1961.

[9] R E Walker, A R Stone, and M Shandor. Secondary Gas Injection in a Conical Rocket Nozzle. *AIAA Journal*, 1:334–338, 1963.

[10] Edward E Zukoski and Frank W Spaid. Secondary injection of gases into a supersonic flow. *AIAA Journal*, 2:1689–1696, October 1964.

[11] M R Gruber, A S Nejad, T H Chen, and J C Dutton. Compressibility effects in supersonic transverse injection flowfields. *Physics of Fluids*, 9(5):1448–1461, 1997.

[12] W. M. Vanlerberghe, J. G. Santiago, J. C. Dutton, and R. P. Lucht. Mixing of a sonic transverse jet injected into a supersonic flow. *AIAA journal*, 38(3):470–479, 2000.

[13] A Ben-Yakar, M G Mungal, and R K Hanson. Time evolution and mixing characteristics of hydrogen and ethylene transverse jets in supersonic crossflows. *Physics of Fluids*, 18(2):26101, 2006.

[14] Eli Lazar, Gregory Elliott, and Nick Glumac. Energy deposition applied to a transverse jet in a supersonic crossflow. *AIAA journal*, 48(8):1662–1672, 2010.

[15] M R Gruber, A S Nejadt, and T H Chen. Mixing and Penetration Studies of Sonic Jets in a Mach 2 Freestream. *Journal of Propulsion and Power*, 11(2):1995–1995, 1995.

[16] J C Mcdaniel and J Graves. A laser-induced-fluorescence visualization study of transverse, sonic fuel injection in a nonreacting supersonic combustor. 1986.

[17] B. K. McMillin, J. M. Seitzman, and R. K. Hanson. Comparison of NO and OH planar fluorescence temperature measurements in scramjet model flowfields. *AIAA Journal*, 32:1945–1952, October 1994.

[18] Steven J Beresh, John F Henfling, and Rocky J Erven. Surface Measurements of a Supersonic Jet in Subsonic Compressible Crossflow for the Validation of Computational Models . *Sandia Report SAND2002-1890*, 2002.

[19] S Beresh, R Erven, J Henfling, and R Spillers. Turbulent Characteristics of a Transverse Supersonic Jet in a Subsonic Compressible Crossflow. *AIAA Journal*, 43:2385–2394, November 2005.

[20] Steven J Beresh, John F Henfling, Rocky J Erven, and Russell W Spillers. Cross-plane Velocimetry of a Transverse Supersonic Jet in a Transonic Crossflow. *AIAA Journal*, 44(12):3051–3061, 2006.

[21] T F Fric and A Roshko. Vortical structure in the wake of a transverse jet. *Journal of Fluid Mechanics*, 279:1–47, 1994.

[22] A. D. Rothstein and P. J. Wantuck, editors. *A study of the normal injection of hydrogen into a heated supersonic flow using planar laser-induced fluorescence*, July 1992.

[23] D Papamoschou and D. G. Hubbard. Visual observations of supersonic transverse jets. *Experiments in Fluids*, 14:468–476, May 1993.

[24] D M Peterson, P K Subbareddy, and G V Candler. Assessment of synthetic inflow generation for simulating injection into a supersonic crossflow. *AIAA Paper 2006–8128*, 2006.

[25] Soshi Kawai and Sanjiva K. Lele. Large-Eddy Simulation of Jet Mixing in Supersonic Crossflows. *AIAA Journal*, 48:2063–2083, September 2010.

[26] F Génin and S Menon. Dynamics of sonic jet injectiion into supersonic crossflow. *J. Turbulence*, 11:1–13, 2010.

[27] Z A Rana, B Thornber, and D Drikakis. Transverse jet injection into a supersonic turbulent cross-flow. *Physics of Fluids*, 23(4):46103, 2011.

[28] P Moin, K Squires, W Cabot, and S Lee. A dynamic subgrid-scale model for compressible turbulence and scalar transport. *Physics of Fluids A*, 3(11):2746–2757, 1991.

[29] A Yoshizawa. Statistical theory for compressible turbulent shear flows, with the application to subgrid modeling. *Physics of Fluids*, 29:2152, 1986.

[30] Robert H Kraichnan. Direct-Interaction Approximation for Shear and Thermally Driven Turbulence. *Physics of Fluids*, 7(7):1048–1062, 1964.

[31] C G Speziale, G Erlebacher, T A Zang, and M Y Hussaini. The subgrid–scale modeling of compressible turbulence. *Physics of Fluids*, 31(4):940–942, 1988.

[32] D K Lilly. The representation of small scale turbulence in numerical simulation experiments. In *IBM Scientific Computing Symposium on environmental sciences*, pages 195–210, Yorktown heights, 1967.

[33] J W Deardorff. Three-Dimensional Numerical Modeling of the Planetary Boundary Layer. In D A Haugen, editor, *Workshop on Mircometeorology*, pages 271–311, Boston, 1973. Amer. Meteorol. Soc.

[34] U Schumann. Subgrid scale model for finite difference simulations of turbulent flows in plane channels and annuli. *Journal of Computational Physics*, 18(4):376–404, 1975.

[35] C.-H. Moeng. A Large-Eddy-Simulation Model for the Study of Planetary Boundary-Layer Turbulence. *Journal of Atmospheric Sciences*, 41:2052–2062, July 1984.

[36] Roger H Shaw and Ulrich Schumann. Large-eddy simulation of turbulent flow above and within a forest. *Boundary-Layer Meteorology*, 61(1):47–64, 1992.

[37] Akira Yoshizawa and Kiyosi Horiuti. A Statistically-Derived Subgrid-Scale Kinetic Energy Model for the Large-Eddy Simulation of Turbulent Flows. *Journal of the Physics Society of Japan*, 54:2834–2839, 1985.

[38] P J Mason. Large-eddy simulation: A critical review of the technique. *Quarterly Journal of the Royal Meteorological Society*, 120(515):1–26, 1994.

[39] S Ghosal, T S Lund, P Moin, and K Akselvoll. A dynamic localization model for large-eddy simulation of turbulent flows. *Journal of Fluid Mechanics*, 286:229, 1995.

[40] S Menon and W W Kim. High Reynolds number flow simulations using the localized dynamic subgrid-scale model, 1996.

[41] Kiyosi Horiuti. Large Eddy Simulation of Turbulent Channel Flow by One-Equation Modeling. *Journal of the Physics Society of Japan*, 54:2855–2865, 1985.

[42] C G Speziale. Analytic methods for the development of reynolds-stress closures in turbulence. *Annual Review of Fluid Mechanics*, 23:107–157, 1991.

[43] Bert Vreman, Bernard Geurts, and Hans Kuerten. Subgrid-modelling in LES of compressible flow. *Applied Scientific Research*, 54(3):191–203, 1995.

[44] Eric Garnier, Nikolaus Adams, and P Sagaut. *Large Eddy Simulation for Compressible Flows (Scientific Computation)*. Springer, 1 edition, August 2009.

[45] William Sutherland. LII. The viscosity of gases and molecular force. *Philosophical Magazine Series 5*, 36(223):507–531, 1893.

[46] H C Yee, N D Sandham, and M J Djomehri. Low-Dissipative High-Order Shock-Capturing Methods Using Characteristic-Based Filters. *Journal of Computational Physics*, 150(1):199–238, 1999.

[47] Suman Muppidi and Krishnan Mahesh. {DNS} of roughness-induced transition in supersonic boundary layers. *accepted by Journal of Fluid Mechanics*, 2011.

[48] X Chai and K Mahesh. Simulations of High Speed Jets in Crossflows. *AIAA Paper 2011–650*, 2011.

[49] A. N. Kolmogorov. The local structure of turbulence in incompressible viscous fluid for very large Reynolds numbers. *Royal Society of London Proceedings Series A*, 434:9–13, July 1991.

[50] J Smagorinsky. General circulation experiments with the primitive equations. I. The basic experiment. *Mon. Weather Rev.*, 91:99–165, 1963.

[51] M Germano, U Piomelli, P Moin, and M Cabot. A dynamic subgrid-scale eddy viscosity model. *Physics of Fluids*, 3:1760, 1991.

[52] R H Kraichnan. Eddy viscosity in two and three dimension. *J. Atmos. Sci.*, 33:1521–1536, 1976.

[53] J P Chollet and M Lesieur. Parametrization of small scales of three-dimensional isotropic turbulence utilizing spectral closures. *J. Atmos. Sci.*, 38:2747–2757, 1981.

[54] A Yakhot, S A Orszag, and Y Yakhot. Renormaliztion-group formulation of large-eddy simulations. *J. Sci. Comp.*, 4:139, 1989.

[55] O Métais and M Lesieur. Spectral large-eddy simulation of isotropic and stably stratified turbulence. *Journal of Fluid Mechanics*, 239:157–194, 1992.

[56] L M Smith and S L Woodruff. Renormaliztion-group analysis of turbulence. *Annual Review of Fluid Mechanics*, 30:275–310, 1998.

[57] M Lesieur and O Métais. New trends in large-eddy simulations of turbulence. *Annu. Rev. Fluid Mech.*, 28:45–82, 1996.

[58] Charles Meneveau and Joseph Katz. Scale-Invariance and Turbulence Models for Large-Eddy Simulation. *Annual Review of Fluid Mechanics*, 32(1):1–32, 2000.

[59] D K Lilly. A proposed modification of the Germano subgrid-scale closure method. *Physics of Fluids A*, 3:1760, 1991.

[60] Prahladh Iyer, Suman Muppidi, and Krishnan Mahesh. Boundary layer transition in high-speed flows due to roughness. *2012–1106*, 2012.

[61] Xiaochuan Chai and Krishnan Mahesh. Dynamic -equation model for large-eddy simulation of compressible flows. *Journal of Fluid Mechanics*, 699:385–413, 2012.

[62] D. E. Everett and M. J. Morris. Wall pressure measurements for a sonic jet injected transversely into a supersonic crossflow. *Journal of propulsion and power*, 14(6):861–868.

[63] Suman Muppidi and Krishnan Mahesh. Study of trajectories of jets in crossflow using direct numerical simulations. *Journal of Fluid Mechanics*, 530:81–100, 2005.

[64] T H New, T T Lim, and S C Luo. Elliptic jets in cross-flow. *Journal of Fluid Mechanics*, 494:119–140, 2003.

[65] S H Smith and M G Mungal. Mixing, structure and scaling of the jet in crossflow. *Journal of Fluid Mechanics*, 357:83–122, 1998.

[66] Suman Muppidi and Krishnan Mahesh. Direct numerical simulation of passive scalar transport in transverse jets. *Journal of Fluid Mechanics*, 598:335–360, 2008.

[67] Y Kamotani and I Greber. Experiments on a Turbulent Jet in a Cross Flow. *AIAA Journal*, 10:1425–1429, November 1972.

[68] Lester L Yuan and Robert L Street. Trajectory and entrainment of a round jet in crossflow. *Physics of Fluids*, 10(9):2323–2335, 1998.

[69] G. N. Abramovich. *The theory of turbulent jets*. Massachusetts Institute of Technology Press, Cambridge, Mass. Chap. 12, Sec. 4, 1963.

[70] Pradeep C. Babu and Krishnan Mahesh. Upstream entrainment in numerical simulations of spatially evolving round jets. *Physics of Fluids*, 16(10):3699–3705, 2004.

[71] F P Ricou and D B Spalding. Measurements of entrainment by axisymmetrical turbulent jets. *Journal of Fluid Mechanics*, 11(01):21–32, 1961.

[72] U Piomelli, W H Cabot, P Moin, and S Lee. Subgrid-scale backscatter in turbulent and transitional flows. *Physics of Fluids A*, 3:1766–1771, 1991.

[73] Thierry Dubois, J A Domaradzki, and Albert Honein. The subgrid-scale estimation model applied to large eddy simulations of compressible turbulence. *Physics of Fluids*, 14(5):1781–1801, 2002.

[74] S Sarkar, G Erlebacher, M Y Hussaini, and H O Kreiss. The analysis and modelling of dilatational terms in compressible turbulence. *Journal of Fluid Mechanics*, 227:473–493, 1991.

[75] K W Bedford and W K Yeo. Conjunctive Filtering Procedures in Surface Water Flow and Transport. In B Galperin and S A Orszag, editors, *Large Eddy Simulation of Complex Engineering and Geophysical Flows*, pages 513–539, New York, 1993. Cambridge Univ. Press.

[76] E Pomraning and C J Rutland. Dynamic One-Equation Nonviscosity Large-Eddy Simulation Model. *AIAA Journal*, 40:689–701, 2002.

[77] Shankar Ghosh and Krishnan Mahesh. Numerical simulation of the fluid dynamic effects of laser energy deposition in air. *Journal of Fluid Mechanics*, 605:329–354, 2008.

[78] E T Spyropoulos and G A Blaisdell. Evaluation of the dynamic model for simulations of compressible decaying isotropic turbulence. *AIAA Journal*, 34(5):990–998, 1996.

[79] Charles Meneveau. Statistics of turbulence subgrid-scale stresses: Necessary conditions and experimental tests. *Physics of Fluids*, 6(2):815–833, 1994.

[80] G Comte-Bellot and S Corrsin. Simple Eulerian time correalation of full- and narrow-band velocity signals in grid-generated isotropic turbulence. *Journal of Fluid Mechanics*, 48:273, 1971.

[81] Gordon Erlebacher, M Y Hussaini, H O Kreiss, and S Sarkar. The analysis and simulation of compressible turbulence. *Theoretical and Computational Fluid Dynamics*, 2(2):73–95, 1990.

[82] J R Ristorcelli and G A Blaisdell. Consistent initial conditions for the DNS of compressible turbulence. *Physics of Fluids*, 9(1):4–6, 1997.

[83] K Mahesh, S K LeLe, and P Moin. The influence of entropy fluctuations on the interaction of turbulence with a shock wave. *Journal of Fluid Mechanics*, 334:353–379, 1997.

[84] J Larsson and S K Lele. Direct numerical simulation of canonical shock/turbulence interaction. *Physics of Fluids*, 21:126101, 2009.

[85] S Lee, S K Lele, and P Moin. Direct numerical simulation of isotropic turbulence interacting with a weak shock wave. *Journal of Fluid Mechanics*, 251:533–562, 1993.

[86] J R Ristorcelli. A pseudo-sound constitutive relationship for the dilatational covariances in compressible turbulence. *Journal of Fluid Mechanics*, 347:37–70, 1997.

[87] Thomas S Lund, Xiaohua Wu, and Kyle D Squires. Generation of Turbulent Inflow Data for Spatially-Developing Boundary Layer Simulations. *Journal of Computational Physics*, 140(2):233–258, 1998.

[88] G Urbin and D Knight. Large-Eddy Simulation of a Supersonic Boundary Layer Using an Unstructured Grid. *AIAA Journal*, 39:1288–1295, July 2001.

[89] S Stolz and N A Adams. Large-eddy simulation of high-Reynolds-number supersonic boundary layers using the approximate deconvolution model and a rescaling and recycling technique. *Physics of Fluids*, 15(8):2398–2412, 2003.

[90] Sheng Xu and M Pino Martin. Assessment of inflow boundary conditions for compressible turbulent boundary layers. *Physics of Fluids*, 16(7):2623–2639, 2004.

[91] B Morgan, J Larsson, S Kawai, and S.˜K. Lele. Improving Low-Frequency Characteristics of Recycling/Rescaling Inflow Turbulence Generation. *AIAA Journal*, 49:582–597, March 2011.

[92] P R Spalart, M Strelets, and A Travin. Direct numerical simulation of large-eddy-break-up devices in a boundary layer. *International Journal of Heat and Fluid Flow*, 27(5):902–910, 2006.

[93] Patrick Bookey, Christopher Wyckham, Alexander Smits, and Pino Martin. New Experimental Data of STBLI at DNS/LES Accessible Reynolds Numbers. *AIAA Paper 2005–0309*, 2005.

[94] Stephen E. Guarini, Robert D. Moser, Karim Shariff, and Alan Wray. Direct numerical simulation of a supersonic turbulent boundary layer at mach 2.5. *Journal of Fluid Mechanics*, 414:1–33, 2000.

[95] A.A Zheltovodov, V.M. Trofimov, E. Schulein, and V.N. Yakovlev. An experiment documentation of supersonic turbulent flows in the vicinity of forward- and backward-facing ramps. *Tech. Rep. 2030. Institute of Theoretical and Applied Mechanics, USSR Academy of Sciences, Novosibirsk*, 1990.

# Appendix A

# Derivation of SGS kinetic energy equation

The SGS kinetic energy equation can be derived by subtracting the product of the Favre-filtered velocity and the filtered momentum equation from the filtered product of velocity and momentum equation, i.e.,

$$\overline{[u_i \times (momentum\ equation)]} - \widetilde{u_i} \times \overline{(momentum\ equation)}. \tag{A.1}$$

First, consider term $\overline{[u_i \times (momentum\ equation)]}$. The momentum equation for compressible flow is

$$\frac{\partial \rho u_i}{\partial t} + \frac{\partial \rho u_i u_j}{\partial x_j} = -\frac{\partial p}{\partial x_i} + \frac{\partial \sigma_{ij}}{\partial x_j}.$$

Multiplying $u_i$ on both sides yields

$$u_i \frac{\partial \rho u_i}{\partial t} + u_i \frac{\partial \rho u_i u_j}{\partial x_j} = -u_i \frac{\partial p}{\partial x_i} + u_i \frac{\partial \sigma_{ij}}{\partial x_j}. \tag{A.2}$$

Now, consider the two terms on the LHS:

$$u_i \frac{\partial \rho u_i}{\partial t} = u_i u_i \frac{\partial \rho}{\partial t} + \rho u_i \frac{\partial u_i}{\partial t} = u_i u_i \frac{\partial \rho}{\partial t} + \rho \frac{\partial \left(\frac{1}{2} u_i u_i\right)}{\partial t}, \tag{A.3}$$

$$u_i \frac{\partial \rho u_i u_i}{\partial x_j} = u_i u_i \frac{\partial \rho u_j}{\partial x_j} + \rho u_i u_i \frac{\partial u_i}{x_j} = u_i u_i \frac{\partial \rho u_j}{\partial x_j} + \rho u_j \frac{\partial \left(\frac{1}{2} u_i u_i\right)}{\partial x_j}. \tag{A.4}$$

Add equations (A.3) and (A.4), and apply continuity equation, the LHS of equation A.2 becomes

$$\begin{aligned} & u_i u_i \left( \frac{\partial \rho}{\partial t} + \frac{\partial \rho u_j}{\partial x_j} \right) + \rho \frac{\partial \left( \frac{1}{2} u_i u_i \right)}{\partial t} + \rho u_j \frac{\partial \left( \frac{1}{2} u_i u_i \right)}{\partial x_j} \\ = \quad & \tfrac{1}{2} u_i u_i \left( \frac{\partial \rho}{\partial t} + \frac{\partial \rho u_j}{\partial x_j} \right) + \left( \tfrac{1}{2} u_i u_i \frac{\partial \rho}{\partial t} + \rho \frac{\partial \left( \frac{1}{2} u_i u_i \right)}{\partial t} \right) + \left( \tfrac{1}{2} u_i u_i \frac{\partial \rho u_j}{\partial x_j} + \rho u_j \frac{\partial \left( \frac{1}{2} u_i u_i \right)}{\partial x_j} \right) \\ = \quad & \frac{\partial \left[ \rho \left( \frac{1}{2} u_i u_i \right) \right]}{\partial t} + \frac{\partial \left[ \rho \left( \frac{1}{2} u_i u_i \right) u_j \right]}{\partial x_j}. \end{aligned} \tag{A.5}$$

The pressure term on the RHS of equation (A.2) can be rewritten as

$$-u_i \frac{\partial p}{\partial x_i} = -\frac{\partial p u_j}{\partial x_j} + p \frac{\partial u_j}{\partial x_j}. \tag{A.6}$$

Substituting equation (A.5) and (A.6), equation (A.2) reduces to

$$\frac{\partial \left[ \rho \left( \frac{1}{2} u_i u_i \right) \right]}{\partial t} + \frac{\partial \left[ \rho \left( \frac{1}{2} u_i u_i \right) u_j \right]}{\partial x_j} = -\frac{\partial p u_j}{\partial x_j} + p \frac{\partial u_j}{\partial x_j} + u_i \frac{\partial \sigma_{ij}}{\partial x_j}. \tag{A.7}$$

Applying space filtering to equation (A.7) and assuming the derivative and filtering operation are commutative yield:

$$\frac{\partial \bar{\rho} \widetilde{\left( \frac{1}{2} u_i u_i \right)}}{\partial t} + \frac{\partial \bar{\rho} \widetilde{\left( \frac{1}{2} u_i u_i u_j \right)}}{\partial x_j} = -\overline{\frac{\partial p u_j}{\partial x_j}} + \overline{p \frac{\partial u_j}{\partial x_j}} + \overline{u_i \frac{\partial \sigma_{ij}}{\partial x_j}}. \tag{A.8}$$

Next, consider term $\widetilde{u_i} \times \overline{(momentum\ equation)}$. Recall the filtered momentum equation:

$$\frac{\partial \bar{\rho} \tilde{u}_i}{\partial t} + \frac{\partial \bar{\rho} \tilde{u}_i \tilde{u}_j}{\partial x_j} = -\frac{\partial \bar{p}}{\partial x_j} + \frac{\partial \widetilde{\sigma_{ij}}}{\partial x_j} - \frac{\partial \tau_{ij}}{\partial x_j}. \tag{A.9}$$

Following similar steps as above, multiplying $\tilde{u}$ on both sides of equation (A.9) and simplifying yield:

$$\frac{\partial \bar{\rho} \left( \frac{1}{2} \tilde{u}_i \tilde{u}_i \right)}{\partial t} + \frac{\partial \bar{\rho} \left( \frac{1}{2} \tilde{u}_i \tilde{u}_i \tilde{u}_j \right)}{\partial x_j} = -\frac{\partial \bar{p} \tilde{u}_j}{\partial x_j} + \bar{p} \frac{\partial \tilde{u}_j}{\partial x_j} + \tilde{u}_i \frac{\partial \widetilde{\sigma_{ij}}}{\partial x_j} - \tilde{u}_i \frac{\partial \tau_{ij}}{\partial x_j}. \tag{A.10}$$

Plugging equation (A.10) and (A.8) into (A.1) yields

$$\begin{aligned}\frac{\partial\left[\frac{1}{2}\bar{\rho}\left(\widetilde{u_iu_i}-\tilde{u}_i\tilde{u}_i\right)\right]}{\partial t} &+ \frac{\partial\left[\frac{1}{2}\bar{\rho}\left(\widetilde{u_iu_iu_j}-\tilde{u}_i\tilde{u}_i\tilde{u}_j\right)\right]}{\partial x_j} = -\frac{\partial}{\partial x_j}\left(\overline{pu_j}-\bar{p}\tilde{u}_j\right)\\ &+ \left(\overline{p\frac{\partial u_j}{\partial x_j}}-\bar{p}\frac{\partial \tilde{u}_j}{\partial x_j}\right)+\left(\overline{u_i\frac{\partial \sigma_{ij}}{\partial x_j}}-\tilde{u}_i\frac{\partial \widetilde{\sigma_{ij}}}{\partial x_j}\right)+\tilde{u}_i\frac{\partial \tau_{ij}}{\partial x_j}.\end{aligned}$$

Adding $\frac{\partial}{\partial x_j}\left(\frac{1}{2}\bar{\rho}\widetilde{u_iu_i}\tilde{u}_j\right)$ on both sides of the equation above and rearrange:

$$\begin{aligned}\frac{\partial\left[\frac{1}{2}\bar{\rho}\left(\widetilde{u_iu_i}-\tilde{u}_i\tilde{u}_i\right)\right]}{\partial t} &+ \frac{\partial\left[\frac{1}{2}\bar{\rho}\left(\widetilde{u_iu_i}-\tilde{u}_i\tilde{u}_i\right)\tilde{u}_j\right]}{\partial x_j} = \frac{\partial\left[\frac{1}{2}\bar{\rho}\left(\widetilde{u_iu_i}\tilde{u}_j-\widetilde{u_iu_iu_j}\right)\right]}{\partial x_j}\\ &- \frac{\partial}{\partial x_j}\left(\overline{pu_j}-\bar{p}\tilde{u}_j\right)+\left(\overline{p\frac{\partial u_j}{\partial x_j}}-\bar{p}\frac{\partial \tilde{u}_j}{\partial x_j}\right)\\ &+ \left(\overline{u_i\frac{\partial \sigma_{ij}}{\partial x_j}}-\tilde{u}_i\frac{\partial \widetilde{\sigma_{ij}}}{\partial x_j}\right)+\tilde{u}_i\frac{\partial \tau_{ij}}{\partial x_j}.\end{aligned} \tag{A.11}$$

Recalling the definition of SGS kinetic energy,

$$\bar{\rho}k=\frac{1}{2}\bar{\rho}\left(\widetilde{u_iu_i}-\tilde{u}_i\tilde{u}_i\right), \tag{A.12}$$

equation (A.11) becomes:

$$\begin{aligned}\frac{\partial\bar{\rho}k}{\partial t}+\frac{\partial\bar{\rho}k\tilde{u}_j}{\partial x_j} &= \frac{\partial\left[\frac{1}{2}\bar{\rho}\left(\widetilde{u_iu_i}\tilde{u}_j-\widetilde{u_iu_iu_j}\right)\right]}{\partial x_j}-\frac{\partial}{\partial x_j}\left(\overline{pu_j}-\bar{p}\tilde{u}_j\right)\\ &+ \left(\overline{p\frac{\partial u_j}{\partial x_j}}-\bar{p}\frac{\partial \tilde{u}_j}{\partial x_j}\right)+\left(\overline{u_i\frac{\partial \sigma_{ij}}{\partial x_j}}-\tilde{u}_i\frac{\partial \widetilde{\sigma_{ij}}}{\partial x_j}\right)+\tilde{u}_i\frac{\partial \tau_{ij}}{\partial x_j}.\end{aligned} \tag{A.13}$$

Equation (A.13) is the SGS kinetic energy equation, which need further simplification to yield the form of equation (4.1). First, consider the second term on the RHS of equation (A.13):

$$\begin{aligned}\overline{pu_j}-\bar{p}\tilde{u}_j &= \overline{\rho RTu_j}-\overline{\rho RT}\tilde{u}_j\\ &= \bar{\rho}R\left(\widetilde{Tu_j}-\tilde{T}\tilde{u}_j\right)\equiv Rq_j\end{aligned} \tag{A.14}$$

Here $q_j$ is the SGS heat flux defined by equation (2.16). Now consider the fourth term on the RHS of equation (A.13).

$$\overline{u_i \frac{\partial \sigma_{ij}}{\partial x_j}} - \tilde{u}_i \frac{\partial \widetilde{\sigma_{ij}}}{\partial x_j} = \left[ \overline{\frac{\partial \left(\sigma_{ij} u_i\right)}{\partial x_j}} - \frac{\partial \left(\widetilde{\sigma_{ij}} \tilde{u}_i\right)}{\partial x_j} \right] - \left( \overline{\sigma_{ij} \frac{\partial u_i}{\partial x_j}} - \widetilde{\sigma_{ij}} \frac{\partial \tilde{u}_i}{\partial x_j} \right) \tag{A.15}$$

Expanding $\sigma_{ij}$ in equation (A.15) yields:

$$\begin{aligned}
\overline{\frac{\partial \left(\sigma_{ij} u_i\right)}{\partial x_j}} &= \frac{\partial}{\partial x_j} \left[ \overline{\rho\nu \left( u_i \frac{\partial u_i}{\partial x_j} + u_i \frac{\partial u_j}{\partial x_i} - u_i \frac{2}{3} \delta_{ij} \frac{\partial u_k}{\partial x_k} \right)} \right] \\
&= \frac{\partial}{\partial x_j} \left[ \overline{\rho\nu \frac{\partial \frac{1}{2} u_i u_i}{\partial x_j}} + \overline{\rho\nu \frac{\partial u_i u_j}{\partial x_i}} - \overline{\rho\nu u_j \frac{\partial u_i}{\partial x_i}} - \overline{\rho\nu u_i \frac{2}{3} \delta_{ij} \frac{\partial u_k}{\partial x_k}} \right] \\
&= \frac{\partial}{\partial x_j} \left[ \bar{\rho}\nu \frac{\widetilde{\partial \frac{1}{2} u_i u_i}}{\partial x_j} + \bar{\rho}\nu \frac{\partial \widetilde{u_i u_j}}{\partial x_i} - \bar{\rho}\nu \frac{5}{3} \widetilde{u_j \frac{\partial u_k}{\partial x_k}} \right] \\
&= \frac{\partial}{\partial x_j} \left[ \bar{\mu} \frac{\widetilde{\partial \frac{1}{2} u_i u_i}}{\partial x_j} + \bar{\mu} \frac{\partial \widetilde{u_i u_j}}{\partial x_i} - \frac{5}{3} \bar{\mu} \widetilde{u_j \frac{\partial u_k}{\partial x_k}} \right]
\end{aligned} \tag{A.16}$$

Here, it is assumed that the kinematic kinematic viscosity $\nu$ are spatially uniform over the filter width, so that $\bar{\mu} = \overline{\rho\nu} = \bar{\rho}\nu$. Similarly,

$$\begin{aligned}
\frac{\partial \left(\widetilde{\sigma_{ij}} \tilde{u}_i\right)}{\partial x_j} &= \frac{\partial}{\partial x_j} \left[ \bar{\nu} \left( \tilde{u}_i \frac{\partial \tilde{u}_i}{\partial x_j} + \tilde{u}_i \frac{\partial \tilde{u}_j}{\partial x_i} - \tilde{u}_i \frac{2}{3} \delta_{ij} \frac{\partial \tilde{u}_k}{\partial x_k} \right) \right] \\
&= \frac{\partial}{\partial x_j} \left[ \bar{\mu} \frac{\partial \frac{1}{2} \tilde{u}_i \tilde{u}_i}{\partial x_j} + \bar{\mu} \frac{\partial \tilde{u}_i \tilde{u}_j}{\partial x_i} - \frac{5}{3} \bar{\mu} \tilde{u}_j \frac{\partial \tilde{u}_k}{\partial x_k} \right].
\end{aligned} \tag{A.17}$$

$$\begin{aligned}
\overline{\sigma_{ij} \frac{\partial u_i}{\partial x_j}} &= \overline{2\mu S^*_{ij} \left(S_{ij} + \Omega_{ij}\right)} = \overline{2\mu S^*_{ij} S_{ij}} \\
&= \overline{2\mu S^*_{ij} \left( S^*_{ij} + \frac{1}{3} \delta_{ij} S_{kk} \right)} = \overline{2\mu S^*_{ij} S^*_{ij}} \\
&= 2\bar{\mu} \widetilde{S^*_{ij} S^*_{ij}}
\end{aligned} \tag{A.18}$$

$$\begin{aligned}
\widetilde{\sigma_{ij}}\frac{\partial \tilde{u}_i}{\partial x_j} &= 2\bar{\mu}\widetilde{S_{ij}^*}\left(\widetilde{S_{ij}}+\widetilde{\Omega_{ij}}\right) = 2\bar{\mu}\widetilde{S_{ij}^*}\widetilde{S_{ij}} \\
&= 2\bar{\mu}\widetilde{S_{ij}^*}\left(\widetilde{S_{ij}^*}+\frac{1}{3}\delta_{ij}\widetilde{S_{kk}}\right) \qquad (A.19) \\
&= 2\bar{\mu}\widetilde{S_{ij}^*}\widetilde{S_{ij}^*}
\end{aligned}$$

Therefore,

$$\begin{aligned}
&\overline{\frac{\partial\left(\sigma_{ij}u_i\right)}{\partial x_j}} - \frac{\partial\left(\widetilde{\sigma_{ij}}\tilde{u}_i\right)}{\partial x_j} \\
&= \frac{\partial}{\partial x_j}\left[\bar{\mu}\frac{\partial}{\partial x_j}\left(\frac{1}{2}\widetilde{u_iu_i}-\frac{1}{2}\tilde{u}_i\tilde{u}_i\right)+\bar{\mu}\frac{\partial}{\partial x_i}\left(\tilde{u}_i\tilde{u}_j-\tilde{u}_i\tilde{u}_j\right)-\frac{5}{3}\bar{\mu}\left(\widetilde{u_j\frac{\partial u_k}{\partial x_k}}-\tilde{u}_j\frac{\partial \tilde{u}_k}{\partial x_k}\right)\right] \\
&= \frac{\partial}{\partial x_j}\left[\bar{\mu}\frac{\partial k}{\partial x_j}+\bar{\mu}\frac{\partial(\tau_{ij}/\rho)}{\partial x_i}-\frac{5}{3}\bar{\mu}\left(\widetilde{u_j\frac{\partial u_k}{\partial x_k}}-\tilde{u}_j\frac{\partial \tilde{u}_k}{\partial x_k}\right)\right], \qquad (A.20)
\end{aligned}$$

and

$$\overline{\sigma_{ij}\frac{\partial u_i}{\partial x_j}} - \widetilde{\sigma_{ij}}\frac{\partial \tilde{u}_i}{\partial x_j} = 2\bar{\mu}\left(\widetilde{S_{ij}^*S_{ij}^*}-\widetilde{S_{ij}^*}\widetilde{S_{ij}^*}\right). \qquad (A.21)$$

Plugging equation (A.20) and (A.21) into equation (A.15) yields

$$\begin{aligned}
\overline{u_i\frac{\partial \sigma_{ij}}{\partial x_j}} - \tilde{u}_i\frac{\partial \widetilde{\sigma_{ij}}}{\partial x_j} &= \frac{\partial}{\partial x_j}\left[\bar{\mu}\frac{\partial k}{\partial x_j}+\bar{\mu}\frac{\partial(\tau_{ij}/\rho)}{\partial x_i}-\frac{5}{3}\bar{\mu}\left(\widetilde{u_j\frac{\partial u_k}{\partial x_k}}-\tilde{u}_j\frac{\partial \tilde{u}_k}{\partial x_k}\right)\right] \qquad (A.22) \\
&\quad -2\bar{\mu}\left(\widetilde{S_{ij}^*S_{ij}^*}-\widetilde{S_{ij}^*}\widetilde{S_{ij}^*}\right).
\end{aligned}$$

The fifth term in equation (A.13) can be rewritten as

$$\tilde{u}_i\frac{\partial \tau_{ij}}{\partial x_j} = \frac{\partial \tau_{ij}\tilde{u}_i}{\partial x_j} - \tau_{ij}\frac{\partial \tilde{u}_i}{\partial x_j} = \frac{\partial \tau_{ij}\tilde{u}_i}{\partial x_j} - \tau_{ij}\widetilde{S_{ij}} \qquad (A.23)$$

Substituting equations (A.14), (A.22) and (A.23) in equation (A.13) yields

$$\begin{aligned}
\frac{\partial \bar{\rho} k}{\partial t} + \frac{\partial \bar{\rho} k \tilde{u}_j}{\partial x_j} \quad = \quad & \frac{\partial \left[ \frac{1}{2} \bar{\rho} \left( \widetilde{u_i u_i} \tilde{u}_j - \widetilde{u_i u_i u_j} \right) \right]}{\partial x_j} - \frac{\partial \left( R q_j \right)}{\partial x_j} + \left( \overline{p \frac{\partial u_j}{\partial x_j}} - \bar{p} \frac{\partial \tilde{u}_j}{\partial x_j} \right) \\
& + \frac{\partial}{\partial x_j} \left[ \bar{\mu} \frac{\partial k}{\partial x_j} + \bar{\mu} \frac{\partial (\tau_{ij} / \rho)}{\partial x_i} - \frac{5}{3} \bar{\mu} \left( \widetilde{u_j \frac{\partial u_k}{\partial x_k}} - \tilde{u}_j \frac{\partial \tilde{u}_k}{\partial x_k} \right) \right] \qquad (A.24) \\
& - 2 \bar{\mu} \left( \widetilde{S^*_{ij} S^*_{ij}} - \widetilde{S^*_{ij}} \widetilde{S^*_{ij}} \right) + \frac{\partial \tau_{ij} \tilde{u}_i}{\partial x_j} - \tau_{ij} \widetilde{S_{ij}}.
\end{aligned}$$

Rearrange equation (A.24), and derive the final form of SGS kinetic energy equation:

$$\begin{aligned}
\frac{\partial \bar{\rho} k}{\partial t} \quad = \quad & - \frac{\partial \bar{\rho} k \tilde{u}_j}{\partial x_j} - \tau_{ij} \widetilde{S_{ij}} - 2 \bar{\mu} \left[ \widetilde{S^*_{ij} S^*_{ij}} - \widetilde{S^*_{ij}} \widetilde{S^*_{ij}} \right] - \frac{\partial}{\partial x_j} \left[ \frac{5}{3} \left( \bar{\mu} \widetilde{u_j \frac{\partial u_k}{\partial x_k}} - \bar{\mu} \tilde{u}_j \frac{\partial \tilde{u}_k}{\partial \tilde{x}_k} \right) \right] \\
& + \frac{\partial}{\partial x_j} \left[ \tau_{ij} \tilde{u}_i + \bar{\mu} \frac{\partial k}{\partial x_j} + \bar{\mu} \frac{\partial}{\partial x_i} \left( \frac{\tau_{ij}}{\bar{\rho}} \right) + R q_j \right] - \frac{\partial}{\partial x_j} \left[ \frac{1}{2} \bar{\rho} \left( \widetilde{u_i u_i u_j} - \widetilde{u_i u_i} \tilde{u}_j \right) \right] \cdot \\
& + \left( \overline{p \frac{\partial u_k}{\partial x_k}} - \bar{p} \frac{\partial \tilde{u}_k}{\partial x_k} \right)
\end{aligned} \qquad (A.25)$$

Equation (A.25) is considered as the exact form of SGS kinetic energy transport equation for compresible flows. Only two assumptions have been made for its derivation: 1) the derivative and filtering operations are commutative; 2) the kinematic viscosity is uniform across filter width, so that it can be taken out the filter operator.